Max-Planck-Institut
für Meteorologie

MAX-PLANCK-GESELLSCHAFT

International Max Planck Research School
on Earth System Modelling

Tidal Mixing and Large-Scale Circulation

Eleftheria Exarchou

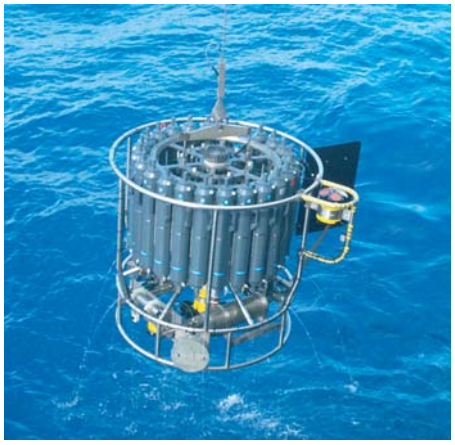

Berichte zur Erdsystemforschung 112/2012

Reports on Earth System Science

Hinweis

Die Berichte zur Erdsystemforschung werden vom Max-Planck-Institut für Meteorologie in Hamburg in unregelmäßiger Abfolge herausgegeben.

Sie enthalten wissenschaftliche und technische Beiträge, inklusive Dissertationen.

Die Beiträge geben nicht notwendigerweise die Auffassung des Instituts wieder.

Die "Berichte zur Erdsystemforschung" führen die vorherigen Reihen "Reports" und "Examensarbeiten" weiter.

Notice

The Reports on Earth System Science are published by the Max Planck Institute for Meteorology in Hamburg. They appear in irregular intervals.

They contain scientific and technical contributions, including Ph. D. theses.

The Reports do not necessarily reflect the opinion of the Institute.

The "Reports on Earth System Science" continue the former "Reports" and "Examensarbeiten" of the Max Planck Institute.

Anschrift / Address

Max-Planck-Institut für Meteorologie
Bundesstrasse 53
20146 Hamburg
Deutschland

Tel.: +49-(0)40-4 11 73-0
Fax: +49-(0)40-4 11 73-298
Web: www.mpimet.mpg.de

Layout:

Bettina Diallo, PR & Grafik

Titelfotos:
vorne:
Christian Klepp - Jochem Marotzke - Christian Klepp
hinten:
Clotilde Dubois - Christian Klepp - Katsumasa Tanaka

Berichte zur Erdsystemforschung 112/2012

Tidal Mixing and Large-Scale Circulation

Eleftheria Exarchou

aus Larissa, Griechenland

Hamburg 2012

Reports on Earth System Science 112/2012

ISSN 1614-1199

Eleftheria Exarchou
Max-Planck-Institut für Meteorologie
Bundesstrasse 53
20146 Hamburg

Als Dissertation angenommen
vom Department Geowissenschaften der Universität Hamburg

auf Grund der Gutachten von
Prof. Dr. Detlef Quadfasel
und
Dr. Jin-Song von Storch

Hamburg, den 27. Januar 2012
Prof. Dr. Jürgen Oßenbrügge
Leiter des Departments für Geowissenschaften

ISSN 1614-1199

Tidal Mixing and Large-Scale Circulation

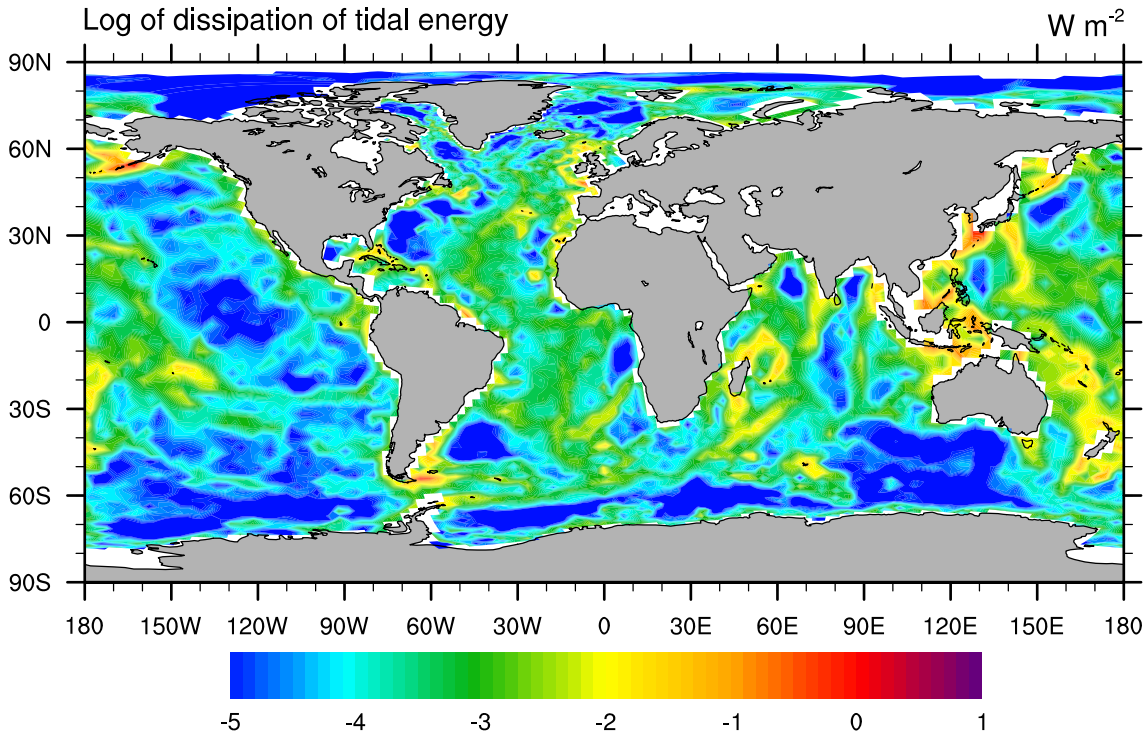

Eleftheria Exarchou

Hamburg 2012

Abstract

Tidal mixing is considered to be one of the main energy sources that drive the Meridional Overturning Circulation. Tidal mixing occurs mainly over rough topography, and leads to a local enhancement of the turbulent diapycnal diffusivity. The diffusivity in the ocean is therefore, due to tidal mixing, spatially inhomogeneous, with small values over smooth regions, and greatly enhanced values over rough topography. Most Ocean General Circulation Models do not take into account the spatial variability of the diapycnal diffusivity, instead they use a spatially homogeneous diffusion. The goal of the present study is to investigate the effect of a more advanced diffusivity scheme, that takes into account tidal mixing, in the ocean general circulation model MPIOM, and to investigate the influence of the scheme on the transient climate response to increasing greenhouse forcing.

The tidal mixing scheme requires a bottom roughness map that can be chosen depending on the scales of topographic features one wants to focus on. Previous observational and theoretical studies suggest that topographical features with length scales smaller than 10 km should be considered on the formulation of the bottom roughness map. In the present study, we examine the sensitivity of the modeled circulations to different spatial scales represented in bottom roughness, by performing uncoupled MPIOM simulations. We compare experiments that include the tidal mixing scheme using bottom roughness calculated at three different spatial scales, ranging from 15-200 km, with a control experiment, which uses the standard configuration with spatially constant diffusivity. Three main results are discussed. First, the three tidal simulations have different equilibrium solutions in the Atlantic Meridional Overturning Circulation (AMOC) and bottom circulations. The strength of the bottom circulations increases with decreasing spatial scales represented in the bottom roughness map. The AMOC decreases at depths between 2000-3000 m in the experiment with bottom roughness map calculated at small scales. The model results, therefore, are sensitive to the formulation of bottom roughness. Second, the changes in the bottom circulations caused by the tidal mixing scheme are not driven by tidally induced changes in convection. Third, among the three tidal simulations, the one using small-scale bottom roughness map has the smallest bias and the strongest bottom water transport, in better agreement with observations.

By performing coupled atmosphere-ocean ECHAM5/MPIOM experiments with the tidal mixing scheme, we investigate the sensitivity of the transient climate change for a global warming scenario to tidal mixing. We perform experiments with two setups; one setup uses the tidal mixing scheme and the second setup uses the standard configuration. We run two experiments with the two setups to quasi-equilibrium with pre-industrial CO_2 concentration. We perform global warming experiments for each

setup, with CO_2 rate of increase equal to $1\%\,yr^{-1}$ until CO_2 doubling (at yr 70), and then we keep CO_2 constant to $2\times CO_2$ for another 430 years. Tidal mixing modifies the transient climate response to CO_2 increase, defined as the difference between the transient and quasi-equilibrium climate. More specifically, tidal mixing enhances the MOC reduction by 30% in the upper cell and by 50% in the lower cell of the global ocean. Tidal mixing reduces surface warming by 9%, and polar amplification, quantified by the maximum normalized polar warming, by 9% in the northern hemisphere and by 17% in the southern hemisphere. Tidal mixing also leads to both weaker summer sea-ice area loss and less late-winter sea-ice melting. The reduction of surface warming due to tidal mixing results from stronger ocean heat uptake. The changes in the ocean heat uptake are caused by advection, i.e. caused by the different response in the circulation indirectly induced by the tidal mixing, rather than directly by the additional diffusion provided by the tidal mixing.

Contents

Chapter 1

Introduction

1.1 Motivation and research questions

The Meridional Overturning Circulation (MOC), defined as the zonally integrated flow in the ocean, is an important component in Earth's Climate. It drives the meridional heat transport that warms up high latitudes; it also stores tracers, like CO_2, in the deep ocean. It consists of deep water formation regions at high latitudes where water becomes dense and sinks, deep currents that transport the deep and dense water horizontally, upwelling regions where the deep water is transported from large depths to the upper ocean, and surface currents that transport the surface light water horizontally. A review of observational studies on the global circulation is given by Schmitz (1995).

There is an ongoing discussion on the drivers of the MOC, in the sense of its energy providers (Wunsch and Ferrari, 2004; Kuhlbrodt et al., 2007; Ferrari and Wunsch, 2010), that can be traced back to Sandström inference: "A circulation can develop from thermal causes only if the level of the heat source lies below the level of the cold source" (Sandström, 1908; Kuhlbrodt, 2008). The ocean is heated and cooled at the same geopotential level, namely, at the sea surface. According to Sandström inference, there should not be deep circulation in the ocean. However, there are currents in the deep and abyssal ocean. In particular, the deep water masses do upwell, return to the surface and eventually close the meridional circulation. The gap between what Sandström inference suggested and the real oceanic circulation was covered by Jeffreys (1925). Jeffreys pointed out that Sandström inference is a valid analysis, if turbulent mixing is taken into account. Mixing transports heat in large depths below the cooling level, and a deep overturning can then develop. In that sense, the ocean is not buoyancy-driven, like the atmosphere; the ocean is instead mechanically driven, with sources of energy that create turbulent mixing, necessary for the ocean overturning circulation. The questions that follow are, how much energy the ocean needs to sustain the deep circulation, and which are then the sources of this energy. Munk and Wunsch (1998) calculated that 2.1 TW are required to sustain the deep circulation. Motivated by observations from satellites (Egbert, 1997), which estimate that 0.9 TW of barotropic energy is dissipated in the deep ocean, Munk and Wunsch suggested that half of the energy (1 TW) for

the deep circulation is coming from dissipation of barotropic tides, and the other half (another 1 TW) from winds (Fig. 1.1). More recent satellite observations support this hypothesis (Egbert and Ray, 2003).

The mechanism by which energy is supplied into the deep ocean is related to the dissipation of the internal wave field in the ocean interior. Tidal internal waves form an important part of the internal wave field. They are baroclinic waves, generated from the interaction of the barotropic tides with rough topography. Part of these internal waves are dissipated at their generation sites; the rest of these waves propagate in the ocean interior and dissipate far away from their generation sites. The local dissipation of these waves at the location of their generation, creates mixing and turbulence, that locally enhances the turbulent diapycnal diffusivity, hence the way that salinity and temperature are mixed, or diapycnally diffused. These arguments are supported by observations, according to which, diffusivity values over rough topography are several orders of magnitude larger than the diffusivity over smooth regions of the ocean (Toole et al., 1994; Polzin et al., 1997; Ledwell et al., 2000). The diffusivity in the ocean, therefore, is highly inhomogeneous in space, with small values over smooth regions, and greatly enhanced values over rough topography.

Most Ocean General Circulation Models (OGCMs) do not take into account the spatial variability of the diapycnal diffusivity. Instead, they assign a constant value to diffusivity, representing the 'background' mixing. The 'background' mixing describes the effect of the internal tides that propagate away from their generation sites and dissipate into the oceanic interior. The effect of the internal tides that dissipate immediately at the generation sites is completely neglected. An attempt to cover this gap was the study by Laurent et al. (2002), that proposed a tidal mixing scheme which takes into account the energy constraints from tidal mixing. The tidal mixing scheme has been implemented and tested in several modeling studies: Simmons et al. (2004); Saenko and Merryfield (2004); Saenko (2006); Montenegro et al. (2007); Jayne (2009). Results from these studies indicate that tidal mixing has a significant effect on the simulated MOC, and that it noticeably improves the ocean state.

The tidal mixing scheme requires a bottom roughness map that can be chosen depending on the scales of topographic features one wants to focus on. Different scales of topographic features would imply a different structure of tidal mixing, hence different structure of diapycnal diffusion. Previous studies that implemented the tidal mixing scheme of Laurent et al. (2002) (Simmons et al., 2004; Saenko and Merryfield, 2004; Montenegro et al., 2007), used the same bottom roughness map, which contains large-scale topographic features. However, studies based on observations and on theoretical arguments (Polzin and Firing, 1997; Naveira Garabato et al., 2004; Polzin, 2004; Muller and Bühler, 2009; Nikurashin and Ferrari, 2010a,b) suggest that small-scale features of topography, such as abyssal hills with length scales $1 - 10$ km, are important for the dissipation of internal waves. Such arguments are further supported in Nikurashin

and Legg (2011) using high resolution two-dimensional numerical simulations. Therefore, there is a gap between the consideration of bottom roughness in modeling studies and what observations suggest. Considering small-scales features in the formulation of bottom roughness in climate models has, until now, unknown effects.

Chapter 2 of the present study, in the context of the studies described above, deals with the implementation of the tidal mixing parameterization by Laurent et al. (2002) in the MPI-Ocean Model MPIOM (Marsland et al., 2003), with the focus being on the sensitivity of the modeled circulation to different spatial scales represented in the bottom roughness map. By performing uncoupled MPIOM simulations that include the tidal mixing scheme using bottom roughness calculated at different spatial scales, we address in Chapter 2 the following research questions:

(1) What is the impact of different scales of bottom roughness on the general circulation?

(2) Do tidally-induced changes in convection drive the strong bottom water transports in the simulations with tidal mixing?

(3) Does tidal mixing improve the MPIOM solution?

Chapter 2 is written in the style of journal publication, and is submitted to Ocean Modeling (Exarchou et al. (2011), currently under revision). Therefore, Chapter 2 can be read independently than Chapter 3.

In recent years, in climate modeling studies, there is an ongoing effort to predict the climate change due to increasing greenhouse forcing. Part of these studies are focused on the time-evolving climate change, rather than the equilibrium climate change, because the interest of the society focuses on the changes that will be taking place in the coming decades, when the system will be far from equilibrium.

The transient climate response to increasing greenhouse forcing is determined by the climate feedbacks and the uptake of heat from the atmosphere into the deep ocean (Gregory and Mitchell, 1997). Tidal mixing, that modifies the way heat is diffused diapycnally in the interior of the ocean, could lead to different ocean heat uptake. Moreover, tidal mixing, as we discuss in Chapter 2, strongly affects the strength of the MOC, hence the climatic variables connected to MOC, such as meridional heat transports, and sea-ice conditions. Tidal mixing, therefore, could lead to different transient climate response to increasing greenhouse forcing.

There is one study that addresses the impact of tidal mixing on the transient climate change (Saenko, 2006); however the study was conducted using a highly idealized

setting, more specifically, an energy-moisture balance atmospheric model, and an idealized geometry ocean model. Therefore, in Chapter 3, we address the question of the effect of tidally driven mixing on the transient climate response to CO_2 increase, by using a far more realistic setting: the fully coupled state-of-the-art Atmosphere-Ocean GCM ECHAM5/MPIOM, that is used in IPCC framework studies for future climate projections. The research questions that are addressed in Chapter 3 are:

(4) What is the effect of tidally driven mixing on the transient climate response to CO_2 increase?

(5) What are the processes responsible for the modified transient climate response?

1.2 Thesis outline

In Chapter 2 we discuss the implementation of the tidal mixing scheme in MPIOM. We perform uncoupled MPIOM simulations and focus on the impact of tidal mixing with different scales of bottom roughness on the general circulation.

In Chapter 3 we investigate the sensitivity of the transient climate change for a global warming scenario to tidal mixing, by performing coupled ECHAM5/MPIOM simulations. We also investigate possible mechanisms responsible for the modified transient climate change in the simulations with tidal mixing.

In Chapter 4 we summarize the main findings of our study and propose possible directions for future research.

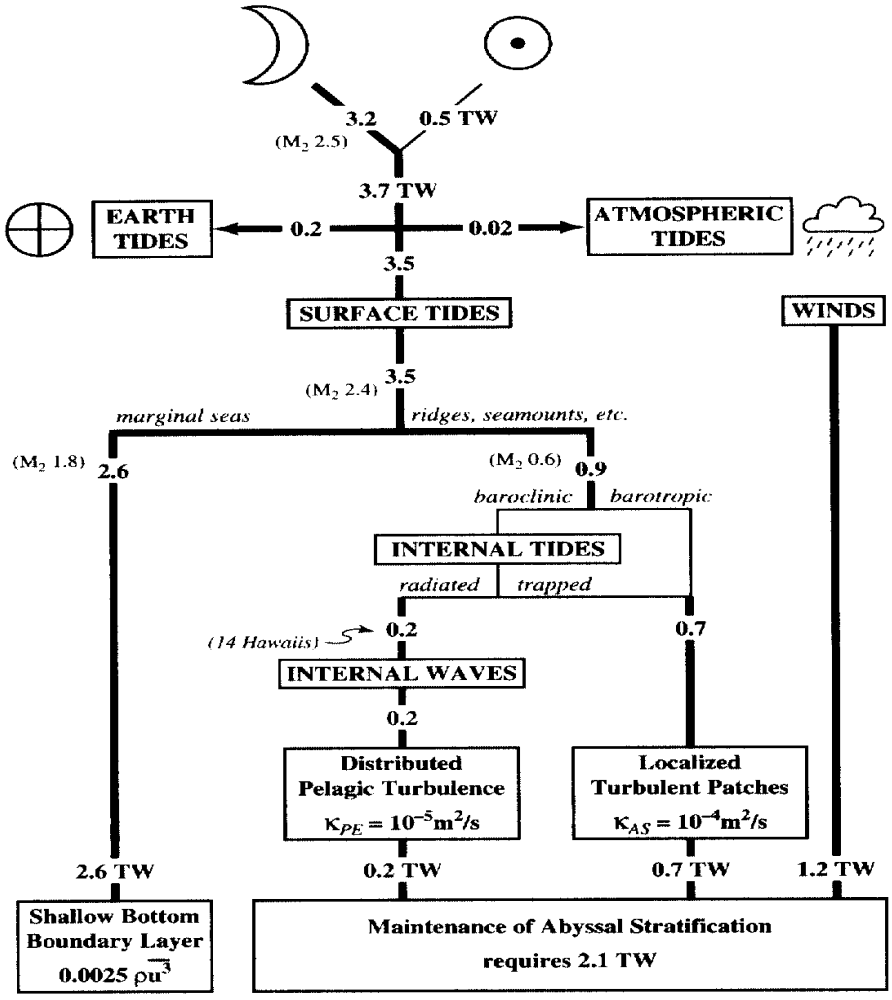

Figure 1.1: A graphical budget of tidal energy flux. Satellite observations (Egbert, 1997) suggest that 0.9 TW of tidal energy are dissipated in the deep ocean (over ridges and seamounts). Another 1.2 TW is estimated to come from wind energy (Wunsch, 1998). The sum from wind and tidal energy is 2.1 TW, and is, according to estimations of Munk and Wunsch, adequate to sustain the deep circulation/stratification (taken from Munk and Wunsch (1998)).

Chapter 2

Impact of tidal mixing with different scales of bottom roughness on the general circulation in the ocean model MPIOM

2.1 Introduction

In the interior of the ocean, according to observations, there is only weak turbulent mixing. Diapycnal diffusivity, which quantifies turbulent mixing, has over most of the ocean area a weak 'background' value around 10^{-5} m^2s^{-1}. Over rough topography, on the other hand, diffusivity has values that are several orders of magnitude larger than the weak background diffusivity (Toole et al., 1994; Polzin et al., 1997; Ledwell et al., 2000). The main source of energy for the enhanced turbulent mixing is considered to be the dissipation of internal waves originating from barotropic tides when they interact with rough topography. Theoretical estimates (Munk and Wunsch, 1998) and observations from satellites (Egbert and Ray, 2003) support that tides provide 1 TW of energy to the deep ocean. Part of tidally induced internal waves break over rough topography. The resulting diffusivity is highly variable in space, and has small values over smooth regions and greatly enhanced values over rough topography.

In most Ocean General Circulation Models (OGCMs) this spatial variability of diapycnal diffusivity that is associated with tides is not taken into account. The effects of tides is merely represented in the form of a spatially homogeneous background diffusivity. Several recent modeling studies (Hasumi and Suginohara, 1999; Simmons et al., 2004; Saenko and Merryfield, 2004; Montenegro et al., 2007; Huang and Jin, 2007; Jayne, 2009) indicate that using more physically based spatially variable diffusion coefficients instead of fixed constant values has a significant effect on the simulated ocean circulation and noticeably improves the ocean state.

The present study deals with the implementation of the tidal mixing parameterization proposed by Laurent et al. (2002) in the MPI-Ocean Model MPIOM (Marsland et al., 2003) and investigates its effects on the overturning circulation. The tidal mixing scheme requires a bottom roughness map that can be chosen depending on the scales

of topographic features one wants to focus on. Previous studies that implemented the scheme (Simmons et al., 2004; Saenko and Merryfield, 2004; Montenegro et al., 2007) used the same bottom roughness, built-in the tidal energy conversion map provided by Jayne and Laurent (2001), which contains topographic features up to 50 km. However, Polzin et al. (1997) argue that tidal mixing occurs over topographic features with small length scales, of the order of $1-10$ km. Taking the above argument into consideration, in our study we focus on the sensitivity of the modeled circulation to the different spatial scales that are represented in the bottom roughness map (sections 2.3.1 and 2.3.2).

The overturning circulation and the bottom circulation in our simulations are strengthened. Previous studies in single-basin, single-hemisphere, idealized models demonstrate that the deep overturning circulation scales with diffusivity (Bryan, 1987; Scott and Marotzke, 2002). Other studies argue that the scaling between the diffusivity and the lower limb of the overturning is different than the scaling for the upper limb (Ito and Marshall, 2008; Nikurarashin and Vallis, 2011). It is not clear whether similar relationships holds for an OGCM with tidal mixing (Jayne, 2009) and additionally, it is not clear that in the case of an enhancement of overturning due to tidal mixing what exactly is the cause of it. We discuss whether the enhancement we observe in our simulations is caused by changes in the convective events or by local changes in the water properties (section 2.4). We describe the changes in the simulated density field in section 2.5). Finally, we compare the results of our simulations with observations in section 2.6 and conclude in section 2.7.

2.2 Methods

2.2.1 Model Description

The model used in this study is the Max Planck Institute Global Ocean-Sea Ice Model MPIOM (Marsland et al., 2003). It has an orthogonal curvilinear grid, with horizontal resolution 3° by 3° near the equator that increases towards the model poles, placed over Greenland and Antarctica. The model resolution ranges between 28 km near Greenland, and 390 km near the tropical Pacific. There are 40 vertical levels. The subgridscale parameterizations of the model include a convective adjustment scheme (Marsland et al., 2003). We do not use enhanced diffusivity to parameterize convection because this would mask enhanced diffusivity due to tidal mixing, since we use the entire diffusivity term as a diagnostic. For the vertical eddy viscosity and diffusivity, the model follows the so-called PP scheme, suggested by Pacanowski and Philander (1981). According to the PP scheme, the total vertical diffusivity is given by

$$k = k_{ri} + k_{bg}, \tag{2.1}$$

where k_{ri} is a Richardson number dependent term which operates mainly within the thermocline, and k_{bg} is the background mixing term and accounts for other sources for mixing, predominantly due to internal waves. In Eq. 2.1 the term k_{winds} is added, which accounts for the turbulent mixing close to the sea surface due to the wind. The model is forced by the OMIP climatological forcing dataset (Röske, 2006).

2.2.2 Tidal mixing parameterization

The tidal mixing parameterization was proposed by Laurent et al. (2002) and used in the modeling studies of Simmons et al. (2004), Montenegro et al. (2007) and Saenko and Merryfield (2004). The parameterization replaces k_{bg} in Eq. 2.1 by

$$k_{bg} + k_{tidal} = k_{bg} + \frac{q\Gamma E(x,y)F(x,y,z)}{\rho N(x,y,z)^2}. \tag{2.2}$$

The term k_{tidal} represents mixing due to local dissipation of tidally induced waves over rough topography. This term is directly related to the energy flux per unit area $E(x,y)$ that is lost from barotropic to baroclinic tides. The term $q = 0.3$ is the portion of the tidal energy that dissipates locally, $\Gamma = 0.2$ is the mixing efficiency, ρ is the density, and $N(x,y,z)$ is the buoyancy frequency. $F(x,y,z)$ of Eq. 2.2 is a vertical structure function, which satisfies $\int_{-H}^{0} F(z)dz = 1$ for each grid point (x,y), and is given by

$$F(x,y,z) = \frac{e^{-(H(x,y)+z)/\zeta}}{\zeta(1-e^{-H(x,y)/\zeta})}, \tag{2.3}$$

where $H(x,y)$ is the total depth of the water column, and $\zeta = 500$m is the vertical decay scale of turbulence. The meaning of the function $F(x,y,z)$ is that the energy that originates from local mixing decays exponentially with height. The term k_{bg} represents the background mixing and accounts for sources of mixing other than the local dissipation of tidal waves, such as breaking of low-mode internal waves that have been generated by barotropic tides and radiated away from their generation sites, or breaking of waves that have been generated by the winds at the surface and have radiated into the ocean interior.

The energy flux per unit area that is lost from barotropic tides to internal waves $E(x,y)$ is given by

$$E(x,y) = \frac{1}{2}\rho_0 N_b(x,y)\kappa h(x,y)^2 \left\langle u(x,y)^2 \right\rangle, \tag{2.4}$$

where ρ_0 is a reference density, $N_b(x,y)$ is the bottom buoyancy frequency, $\left\langle u^2 \right\rangle$ is the mean square tidal velocity, taken from a tidal model (Zahel et al., 2000), κ is the wavenumber of topography, which is taken constant and is used as a tuning parameter, and $h(x,y)^2$ is the bottom roughness. We explain in more detail in the section below how the value for $h(x,y)^2$ is calculated, and how κ is tuned. Concerning the tidal

velocity, we note here a difference to Jayne and Laurent: the velocities used by Jayne and Laurent are derived from a tidal model with extra terms that account for the wave dissipation. These terms resulted in reducing the rms error when compared with the observed tides. In Zahel et al. such terms are not used, because this effect is implicitly considered by the dynamic residuals appearing in their results due to data assimilation (W. Zahel, 2010, personal communication). In addition, the rms errors in Zahel et al. are significantly smaller than in Jayne and Laurent, which indicates the good performance of the tidal model and gives us confidence on the tidal velocities dataset.

The tidal mixing scheme, thus, depends on bottom roughness, mean tidal velocity amplitudes and stratification. It also evolves as part of the model solution, through its dependence on the buoyancy frequency N and the density ρ.

2.2.3 Bottom roughness resulting from topographic features at different spatial scales

Previous studies (Polzin et al., 1997; Polzin, 2004; Muller and Bühler, 2009) suggest that tidal mixing is maintained by the dissipation of internal waves over small-scale features of topography, such as abyssal hills with length scales $1-10$ km, rather than over large-scale topographic features. This argument is further supported in Nikurashin and Legg (2011) using high resolution numerical simulations. In previous studies that implemented the tidal mixing parameterization of Laurent et al., (Saenko and Merryfield, 2004; Simmons et al., 2004), bottom roughness (which is used for the calculation of the energy conversion map $E(x, y)$ in Eq. 2.4) is taken from Jayne and Laurent (2001), and is modeled as the root-mean square residual from a smooth surface fitted to the topography over an area with 50 km radius. This roughness map, therefore, captures topographic features on scales up to 50 km. A consideration of roughness at different spatial scales results in different spatial distribution of the energy dissipation and in different model solutions, as we will see in the next section. This comprises the main research question we address in this paper, the impact of different modeled roughnesses on the model solution.

To achieve our research goal we use differently modeled bottom roughness maps $h(x, y)$ which result in three different energy conversion maps $E(x, y)$. The first bottom roughness map (hereafter: 'small-scale') contains only small-scale topographic features. It is defined as the root mean squares of the residuals from smoothed surfaces over areas of size 15×15 km^2, which is then interpolated to the model grid. The second bottom roughness map (named 'large-scale') is the root mean squares of the residuals from smoothed surfaces on model grid, whose size is by and large about 200 km. In both maps the topography dataset used for calculating the smoothed surfaces is the high

resolution (2 minute) topography dataset from ETOPO2[1]. The smoothed surfaces are derived by fitting polynomial sloping surfaces, either on a 15×15 km^2 grid in the first case, or on the coarse model grid in the second case. The third bottom roughness map (named 'medium-scale') is directly taken from Jayne (2009), and is derived using a 50 km smoothing radius. In general, the medium-scale and large-scale maps that capture topographic features on scales of several tens of kilometers up to about 300 km reveal values larger than the small-scale map that represents topographic features on scales smaller than 15 km.

For the large-scale and small-scale roughness maps, the respective energy flux E is obtained following Eq. 2.4, where by adjusting κ the surface integral of E over areas with depth larger than 1000 m is 1 TW. The physical interpretation of κ is that it characterizes the wavenumber of bathymetry, and in principle should be calculated directly from the topography. Here, in line with previous studies (Jayne and Laurent, 2001; Jayne, 2009), we treat κ as a constant parameter which we tune so that the integrated energy flux gives the value of 1 TW. Due to the different smoothing radius used in the calculation of these maps, the roughness h is smaller in small-scale compared to large-scale. Hence, κ in small-scale is adjusted to a value significantly larger than its value in large-scale ($\kappa|_{\text{large-scale}} \sim 2\pi/170$ km^{-1}, $\kappa|_{\text{small-scale}} \sim 2\pi/2$ km^{-1}). The energy flux for the medium-scale roughness is directly provided by Jayne. Note that the same surface integral of the medium-scale energy flux, after having been interpolated onto our model grid, is about 1.4 TW. In our experiments we did not scale the medium-scale energy flux to 1 TW. However, a shorter parallel test run (not shown) with scaled medium-scale energy flux to 1 TW, did not have qualitatively different solution from the one we consider here.

Having inferred the value of the parameter κ for the large-scale and small-scale roughness (for the medium-scale roughness the value of κ is provided by Jayne (2009)), we can compare the combined effect of roughness and wavenumber of the bathymetry, given by the quantity κh^2, as it appears in Eq. 2.4. The medium-scale and large-scale maps appear to be strikingly similar at their large scale features, despite the different smoothing radius used in each map (Fig. 2.1). The main differences between these two are in the coastal regions, where medium-scale map has larger κh^2 values. In contrast, both medium-scale and large-scale are very different from the small-scale map. The small-scale map appears to have more smeared out features, rather than having large κh^2 values concentrated at some certain regions, as is the case in the other two topography maps. The differences are revealed further in Fig. 2.2. small-scale has higher κh^2 values compared to the other two cases over the ridges in Mid-Atlantic Ocean, Indian Ocean, and East Pacific, and weaker in West Pacific and, in comparison

[1]U.S. Department of Commerce, National Oceanic and Atmospheric Administration, National Geophysical Data Center, 2006. 2-minute Gridded Global Relief Data (ETOPO2v2) http://www.ngdc.noaa.gov/mgg/fliers/06mgg01.html

to medium-scale, in almost all coastal regions.

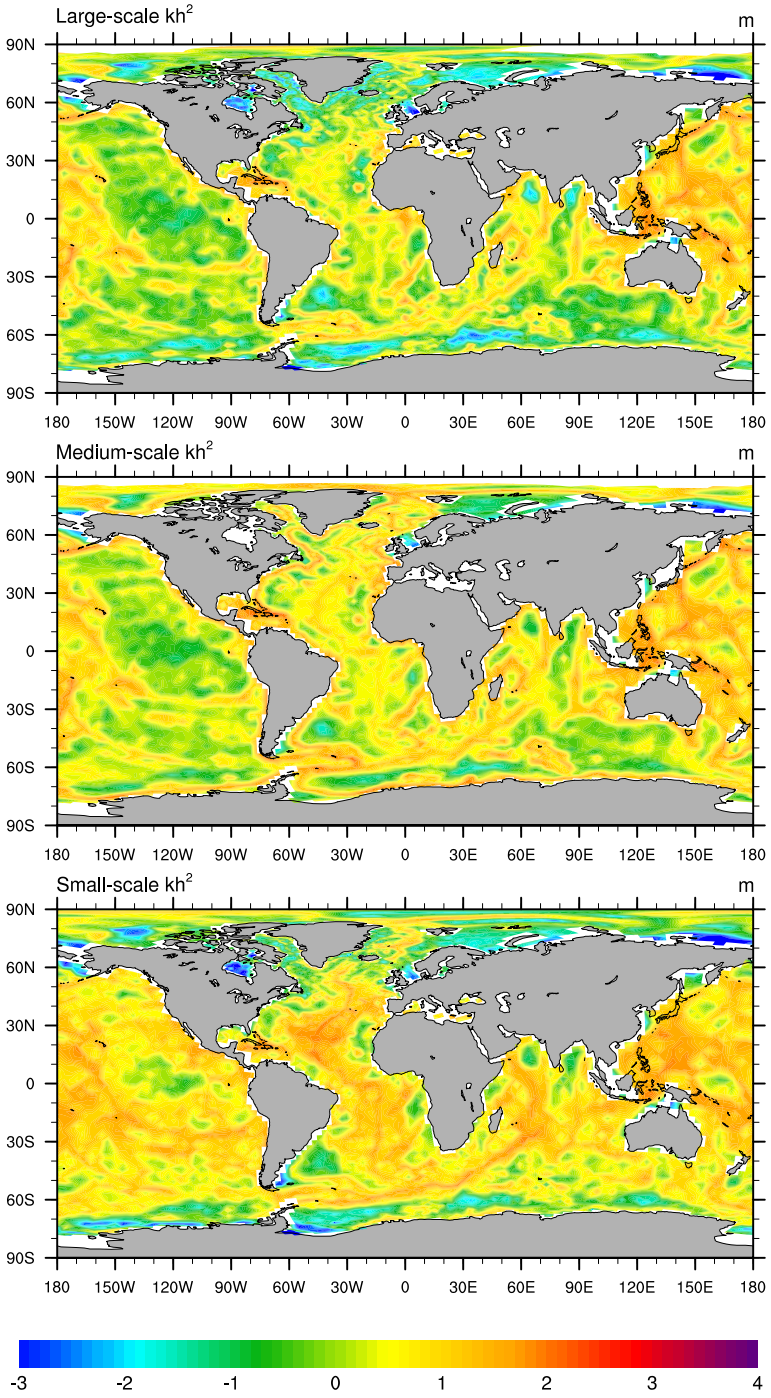

Figure 2.1: Quantity κh^2 of Eq. 2.4 (in a log scale, units are m) based on large-scale (top), medium-scale (middle) and small-scale (bottom) derived bottom roughness.

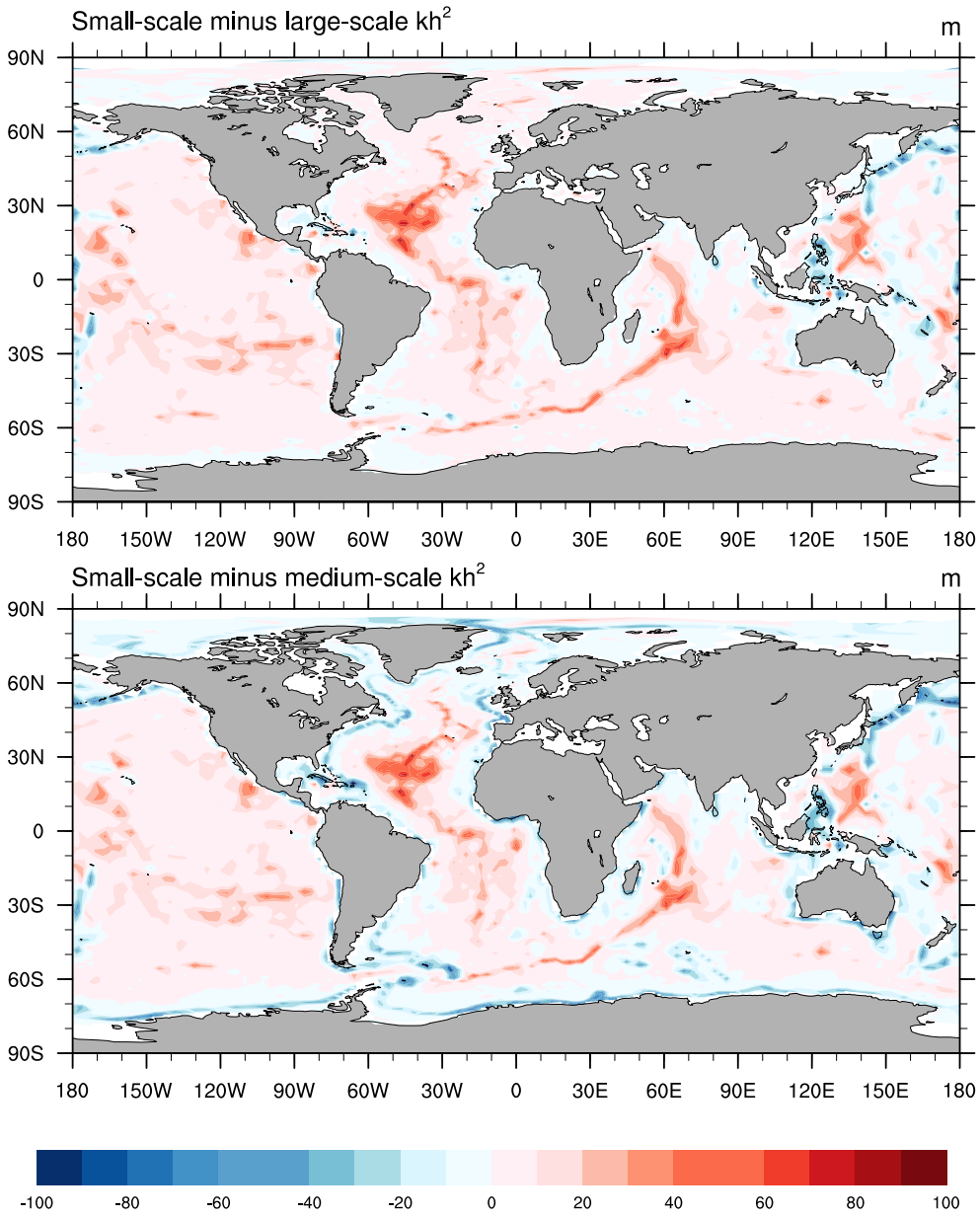

Figure 2.2: Difference between κh^2 based on different calculations of bottom roughness: small-scale minus large-scale (top) and small-scale minus medium-scale (bottom). (Units are m).

2.2.4 Experiments

We perform four simulations that are initialized from the Levitus dataset (World Ocean Atlas 1998, hereafter WOA98, Levitus et al. (1998)) and span 2000 years each. One control experiment uses the default PP scheme diffusivity k with the background term

k_{bg} equal to 10^{-5} m^2s^{-1} ('CtrEXP'). The tidal effect in the control experiment is represented only by the constant background term, which accounts for the background mixing arising from breaking of tidal or wind generated internal waves. The other three simulations utilize the tidal mixing scheme and add in the diffusion coefficient the tidal term k_{tidal} given in Eq. 2.2. The tidal effect, hence, is described by a spatially variable term, representing the local dissipation of tides over rough topography, and a weak background term k_{bg} equal to 10^{-5} m^2s^{-1}, representing the weak background mixing due to breaking of internal waves. The three simulations use the large-scale, medium-scale and small-scale energy dissipation maps shown in Fig. 2.1 and are called hereafter 'large-scaleEXP', 'medium-scaleEXP' and 'small-scaleEXP', respectively. We note here that due to small buoyancy frequencies N close to the bottom, the tidal term in Eq. 2.2 can yield unrealistically large values. To overcome this problem we use as an upper limit for k_{tidal} the value of 2×10^{-3} m^2s^{-1}. Similar problem was reported in Saenko and Merryfield where they used the same truncation value like here, as well as in Montenegro et al., where they truncated at 5×10^{-4} m^2s^{-1}.

Fig. 2.3 shows a vertical section of diffusivity over the Mid-Atlantic Ridge at 35° N for the three tidal runs. The similarity between medium-scaleEXP and large-scaleEXP is evident, both experiments produce near-bottom diffusivity values over the ridge close to $6-7$ cm^2s^{-1} which they decrease to the background value $0.1-0.2$ cm^2s^{-1} at ~ 1 km above the ridge. In contrast, small-scaleEXP produces higher diffusivities, reaching 25 cm^2s^{-1} near bottom, and decreasing to ~ 0.8 cm^2s^{-1} at 1 km above the ridge. From the horizontal distribution of energy dissipation, shown in Fig. 2.2 we expect such differences in diffusivities among the three simulations, since the energy conversion in small-scale is stronger everywhere in the Atlantic Ocean. Additional differences can occur due to different density and buoyancy fields, through their non-linear relation to the energy dissipation in Eq. 2.2. From oceanic observations over rough topographies (Polzin et al., 1997; Toole et al., 1994) we expect enhanced diffusivity values larger than 10 cm^2s^{-1} within 150 m from the bottom, and larger than 1 cm^2s^{-1} within 500 m from the bottom. 'small-scaleEXP', therefore, cannot be considered unrealistic.

The experiments are summarized in Table 2.1. The analysis that follows in the next sections uses time means of the last 200 years of the 2000 year-long simulations, and each experiment is compared to CtrEXP which is considered as a reference run. The large number of simulations, four in total plus some additional runs that are discussed later, did not allow for longer runs. The trends for globally averaged potential temperature and salinity at 4000 m depth at the last years of the integration are less than 0.08 degrees Celsius and 0.03 psu per thousand years, respectively. For the Atlantic MOC the trends at 1000 m and 3500 m depth are less than 0.05 Sv and 0.03 Sv per hundred years, respectively. The last 200 years represent hence states that are close to quasi-equilibrium.

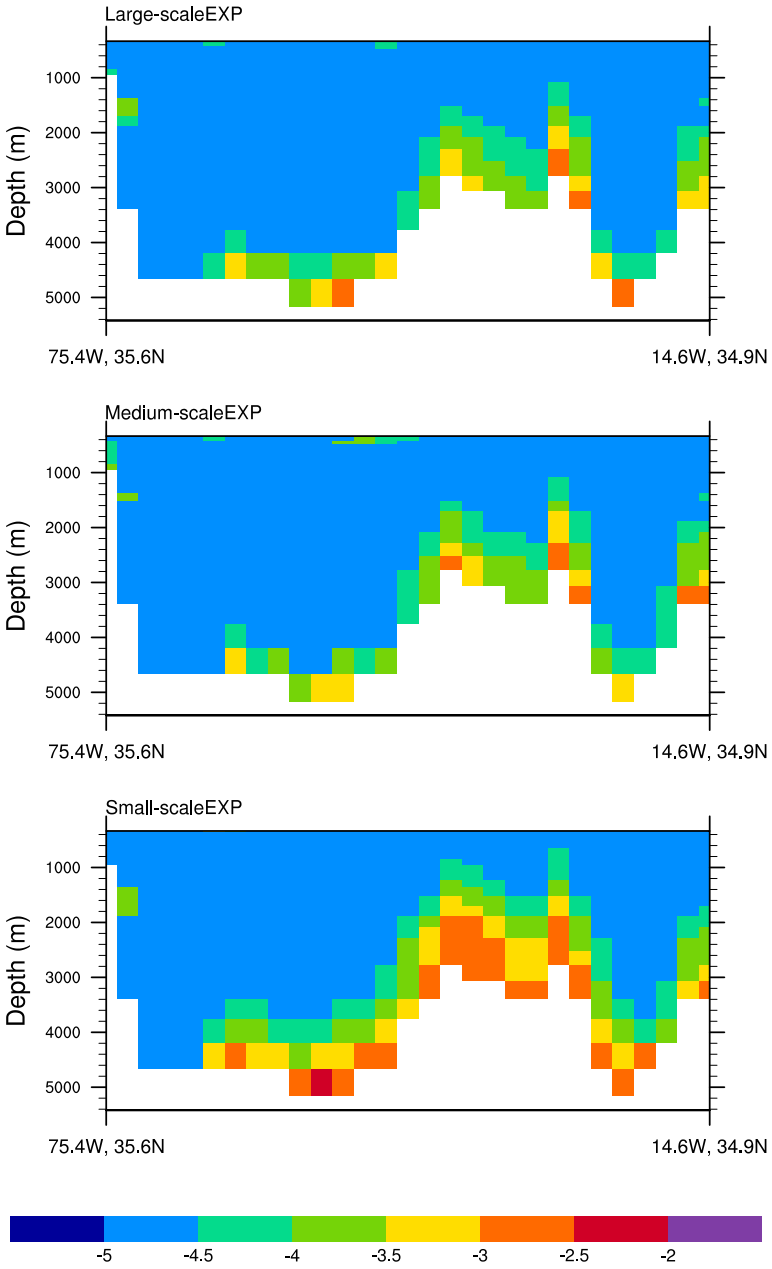

Figure 2.3: Vertical section of diffusivity (in a log scale, units are $m^2 s^{-1}$) at 35° N, of large-scaleEXP (top), medium-scaleEXP (middle) and small-scaleEXP (bottom). The longitudes and latitudes of the end points of the section are shown in the x axis.

2.3 Results in the general circulation

In the current section we discuss the differences in the large-scale circulation in the major ocean basins among the experiments.

	large-scaleEXP	medium-scaleEXP	small-scaleEXP	CtrEXP
$k_{bg}(m^2s^{-1})$	10^{-5}	10^{-5}	10^{-5}	10^{-5}
k_{tidal} (m^2s^{-1})	$q\Gamma FE_{\underset{scale}{large}}/\rho N^2$	$q\Gamma FE_{\underset{scale}{medium}}/\rho N^2$	$q\Gamma FE_{\underset{scale}{small}}/\rho N^2$	0

Table 2.1: Summary of the experiments performed in this study.

2.3.1 Atlantic Ocean

Interestingly, each experiment shows a different response in the Atlantic Ocean circulation (Fig. 2.4). CtrEXP has a reasonably strong circulation, with a North Atlantic Deep Water cell (NADW) that reaches up to 20 Sv at 40° N and 1000 m depth, and an Antarctic Bottom Water cell (AABW) in which the flow reaches 3 Sv at 3500 m depth. Large-scaleEXP exhibits an increase in the overturning streamfunction throughout the entire NADW cell. The maximum transport in the NADW cell in large-scaleEXP is 2 Sv larger than CtrEXP and shifted 300 m deeper and 5 degrees to the North. In addition, in large-scaleEXP the strength of the AABW cell is increased by about 1.7 Sv. In contrast, small-scaleEXP behaves quite differently compared to large-scaleEXP: the bottom water transport in the AABW cell is enhanced by 4 Sv compared to CtrEXP, thus reaching up to 7 Sv. At the same time, the NADW strength is slightly increasing about 0.5 Sv at 1500 m depth, and decreasing at depths between 2000-3000 m. The third experiment, medium-scaleEXP, is between large-scaleEXP and small-scaleEXP: The strength of the AABW cell is enhanced by 2 Sv, and the NADW cell is significantly enhanced mainly at depths between 1000-3000 m, but weakened above 1000 m depth, compared to CtrEXP. In addition, the maximum streamfunction value of the NADW cell is shifted downward and slightly northward.

Given the sensitivity of the model to diapycnal diffusivity, it may not be a big surprise that each tidal simulation drifts to its own solution. We will discuss more about the differences among the experiments in sections 2.4 and 2.5.

2.3.2 Pacific Ocean

In the Pacific Ocean, CtrEXP reveals three shallow subtropical cells, and a bottom cell extending northward transport from the Southern Ocean up to about 30° N with maximum upwelling strength of about 5 Sv at 4000 m depth (see Fig. 2.5). The three tidal simulations change in the same direction (but different amplitudes): in all three experiments the bottom water transport is significantly strengthened, by 5.5 Sv in large-scaleEXP and medium-scaleEXP, and by 6.5 Sv in small-scaleEXP, when compared to CtrEXP. Saenko and Merryfield (2004) had a similar conclusion in their modeling study, in which bottom water circulation in the Pacific Ocean is greatly enhanced when tidal mixing is taken into account. In fact, without tidal mixing, the Pacific Ocean of that

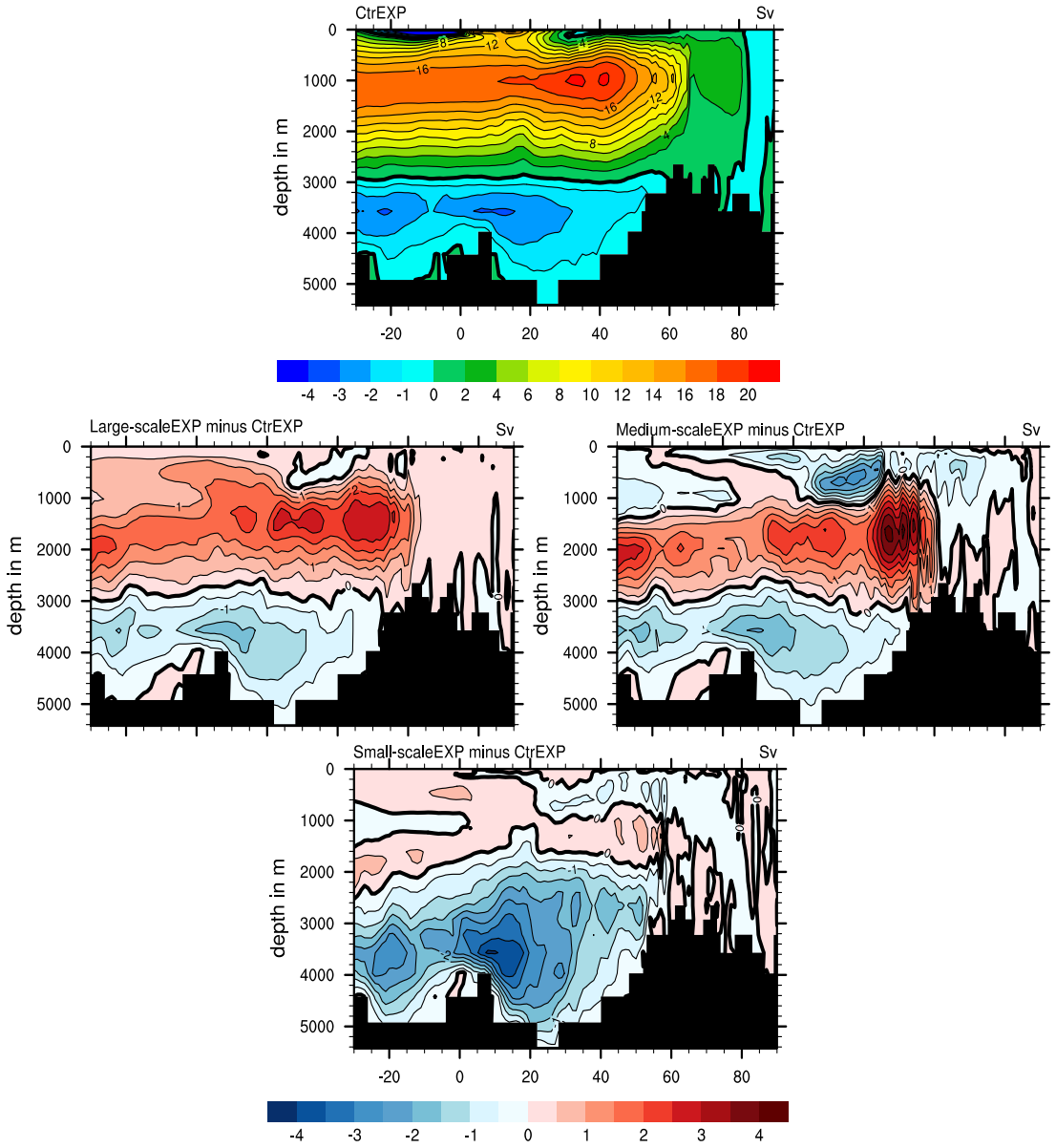

Figure 2.4: Meridional overturning streamfunction, in Sv, for the Atlantic Ocean for CtrEXP (top, contour interval is 1 Sv for negative and 2 Sv for positive values). Differences from CtrEXP: large-scaleEXP (middle left), medium-scaleEXP (middle right) and small-scaleEXP (bottom). Contour interval is 0.5 Sv.

study becomes a stagnant basin, with no circulation in the deep/bottom ocean.

Observations (Talley et al., 2003) indicate that there is significant bottom water flow in the Pacific Ocean, with a maximum northward transport of bottom water close to 13 Sv at 28° S. In CtrEXP, the bottom water transport, which reaches 3 Sv at 28° S and 5 Sv close to the equator, is quite underestimated. In the tidal runs, the bottom transport around 25-30° S reaches about 9 Sv in large-scaleEXP and medium-scaleEXP and 11 Sv in small-scaleEXP. Tidal mixing, therefore, significantly improves the circulation in the Pacific Ocean, even though the transports are still weaker than those suggested by observations.

2.4 Sensitivity of bottom cells to changes in convective activity induced by tidal mixing

Numerous previous studies examine the relation between diapycnal diffusivity and the production of bottom water. The study of Nikurarashin and Vallis (2011), performed using an idealized single basin setting, demonstrated that the deep overturning circulation in a single basin, with the deep water source in the South Hemisphere, scales with diffusivity. Ito and Marshall (2008) reached to a similar scaling relation using residual-mean theory, tested with an idealized OCGM. Tsujino et al. (2000), using an OGCM with horizontally homogeneous and vertically varying diffusivity, found that a strong deep Pacific circulation cannot be reproduced without a depth-increasing diffusivity. Furue and Masahiro (2005), in a two-basin model with idealized configuration, found that deep diffusivity increased only in the Pacific Ocean leads to enhancement of AABW production.

In our experiments with tidal mixing, which produces a depth-increasing spatially inhomogeneous diffusivity, the bottom water transport is significantly enhanced, in line with the aforementioned studies. Additionally, experiment small-scaleEXP produces the strongest among the three tidal runs bottom water transport, which is almost doubled in both Atlantic and Pacific (CtrEXP taken as a reference value). What causes such a strong enhancement of bottom water transport in small-scaleEXP? Bottom water, both in Atlantic and Pacific Ocean, is formed in the Southern Ocean with open ocean deep convection (Jacobs et al., 1970). One possible explanation for the strong bottom water transport in small-scaleEXP is the remote action of convection, due to enhanced tidal mixing in the convection regions of the Southern Ocean. The mechanism at work is that tidal mixing affects the local properties of the water masses by affecting the way that temperature and salinity are mixed from surface down to larger depths, thus affecting the stratification of the water column by making it more homogeneous, and finally facilitating the convection events. An enhancement in convective events will then strengthen the deep water formation leading to an increase in bottom water

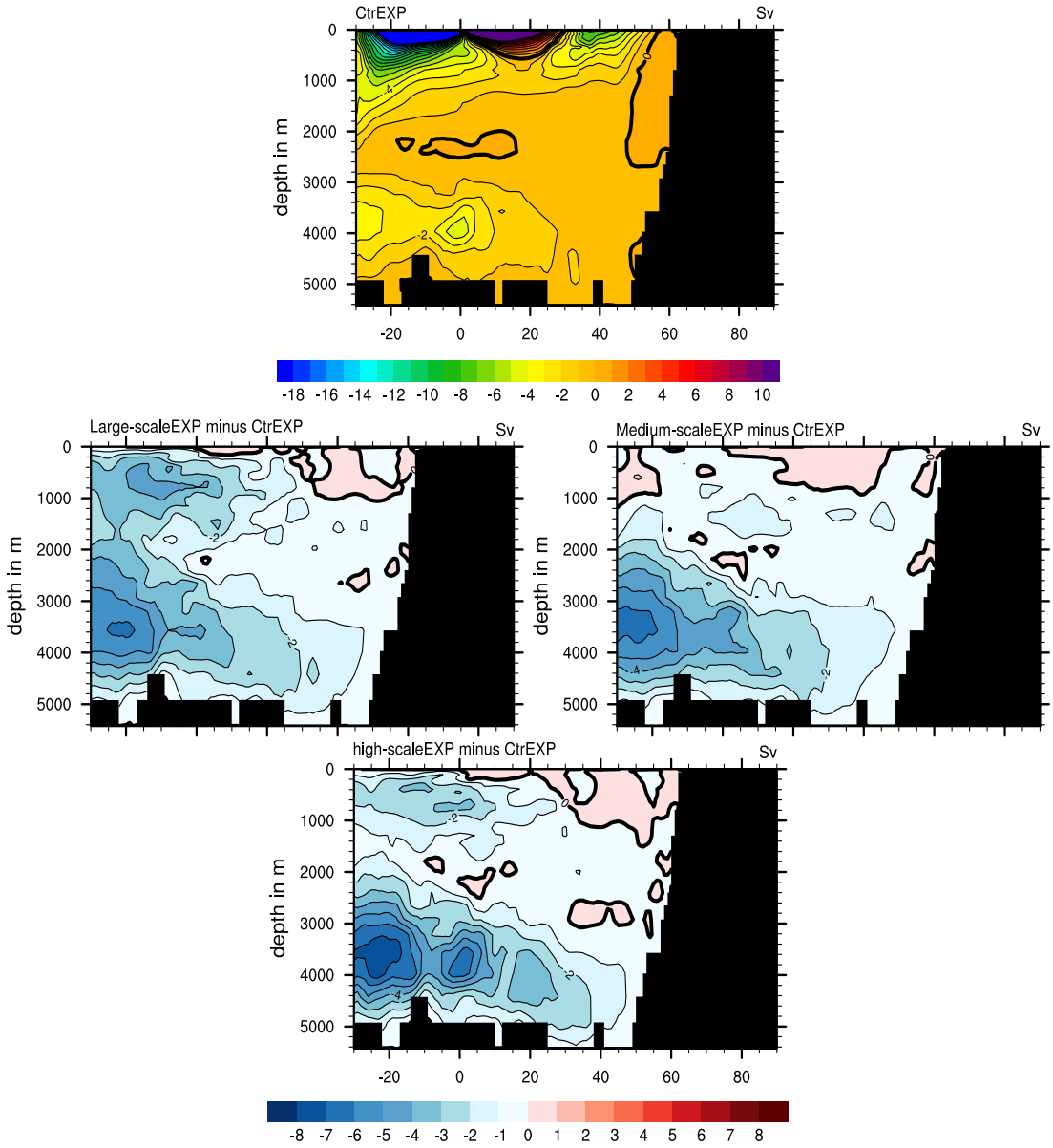

Figure 2.5: Meridional overturning streamfunction, in Sv, for the Pacific Ocean for CtrEXP (top). Differences from CtrEXP: large-scaleEXP (middle left), medium-scaleEXP (middle right) and small-scaleEXP (bottom). Contour interval is 1 Sv.

transport. If our hypothesis is valid, switching-off tidal mixing in convection areas would not favor convection events. Bottom water formation would not be enhanced, and bottom water transport transport would not be strengthened. To test our hypothesis, we perform one additional experiment, named small-scaleSO-EXP, in which tidal mixing is switched off in the Southern Ocean in small-scaleEXP. The experiment starts from WOA98 and is integrated for 1000 years. We note here that by Southern Ocean we mean the entire circumpolar area that extends zonally from Drake Passage (55° S) up to Antarctica, and it includes all the major convections sites of the Southern Hemisphere in the model. Results from this additional experiment (shown in Fig. 2.6) do not support our hypothesis. Apart from some local differences, tidal mixing in the Southern Ocean cannot explain the increase of the bottom transport of the order of 4 Sv in the Atlantic Ocean (Fig. 2.4) and 6.5 Sv in the Pacific Ocean (Fig. 2.5). Our hypothesis is rejected, suggesting that the differences in bottom water transport are not driven by the differences in the convective events induced by tidal mixing.

The experiment small-scaleSO-EXP demonstrates quite clearly that tidal mixing in convection regions is not responsible for the great enhancement of the bottom water transport in small-scaleEXP. Additional experiments (not shown) in which we switch off mixing in the other major convection regions, namely in the Nordic Seas and in the Labrador Sea, yield the same result: changes in convection due to tidal mixing do not significantly affect the overturning circulation. What is driving the changes in the bottom circulation instead, is the local mixing in the vast area of the ocean bottom.

Our result is in line with the study of Scott and Marotzke (2002), in which it was found that in a single-hemisphere, idealized geometry model, high latitude mixing, where stratification is weak, has a weak impact on the MOC strength, because it is unable to drive strong vertical buoyancy fluxes. Mixing at low latitudes, instead, where there is strong stratification and high surface temperature, has very strong effect on MOC strength.

2.5 Changes in horizontal density gradients

In the current section we discuss how the modifications of the water masses due to tidal mixing are associated with the enhancement in the deep and bottom water transports.

The large-scale circulation is to a good approximation in geostrophic balance. The combination of geostrophy and the hydrostatic approximation under the Boussinesq approximation lead to the thermal wind equation,

$$f\rho_0\frac{\partial v}{\partial z} = -g\frac{\partial \rho}{\partial x}, \tag{2.5}$$

which relates the zonal density gradient $\partial\rho/\partial x$ with the meridional velocity shear $\partial v/\partial z$. Assuming a level of no motion at $z = z_0$, the vertical integration of Eq. 2.5

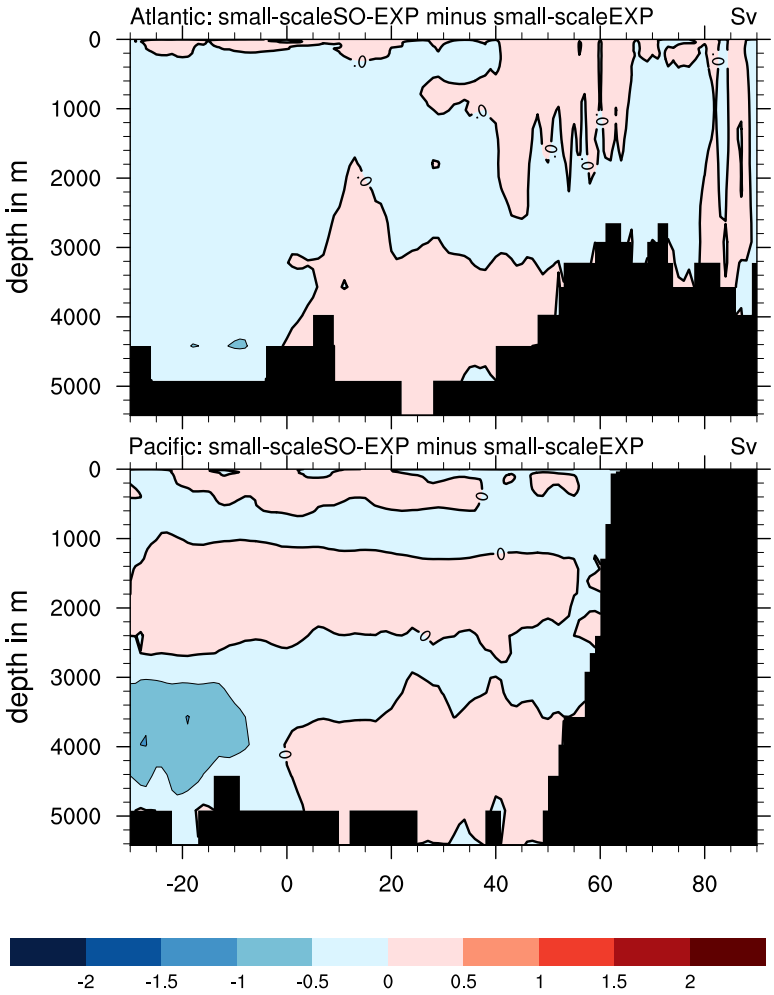

Figure 2.6: Differences in meridional overturning streamfunction, in Sv, between small-scaleSO-EXP and small-scaleEXP, for Atlantic Ocean (top) and Pacific Ocean (bottom). Contour interval is 0.5 Sv.

leads to

$$f\rho_0 v(z) = -\int_{z_0}^{z} g\frac{\partial \rho}{\partial x}. \tag{2.6}$$

Eq. 2.6 implies that large horizontal density gradients are associated with strong absolute meridional transport. Figures 2.8 and 2.7 show the potential density field σ_4 at a vertical section in North Atlantic and South Pacific, respectively, along an east-west section close to the maximum of the bottom water transport of each ocean basin. One striking result is that CtrEXP has stronger vertical density gradient below 2500 m depth compared to the other three experiments, demonstrated by the large number of contour lines at these depths in CtrEXP. Smaller vertical density gradients, hence more homogeneous water column, in the other three experiments is a result of tidal mixing

in the tidal simulations. A more careful inspection reveals that the isopycnals in the tidal simulations are not lifted uniformly, but rather they have strong slopes, especially in the Atlantic section in small-scaleEXP. Larger isopycnal slopes are associated with stronger meridional flow, as seen from the thermal wind balance in Eq. 2.6 Experiment small-scaleEXP has steeper isopycnal slopes (Fig. 2.8), which in turn are associated to stronger deep/bottom water transport in small-scaleEXP than the two other tidal experiments, consistent with geostrophic balance in the ocean's interior.

2.6 Comparison with observations

The tidal mixing scheme affects the vertical distribution of temperature and salinity, hence the density of the water masses. The bias, defined as the departure from WOA98 data, can provide us with a measure for assessing the improvement achieved by including the tidal mixing scheme. Figures 2.11 and 2.10 show the zonally averaged density σ_4 bias for Atlantic and Pacific, respectively. In CtrEXP, the water masses are too light in the upper 2-3 km of the ocean, and too dense from that level down to the ocean bottom, when compared to the WOA98 climatology. This results mainly from too warm waters in the upper 2-3 km, and too cold waters in the deep and bottom ocean regions, which means that heat is not adequately mixed down to the deep/bottom ocean. Here, we note that the bias in CtrEXP in the Atlantic is temperature driven. The salinity bias, characterized by a too saline upper ocean and a too fresh deep ocean, has a contribution to the density bias that opposes the temperature bias. In the Pacific, the salinity bias is positive everywhere, thus contributing to the density bias only in the deep/bottom ocean. Tidal mixing, which is mainly large close to the ocean bottom, opposes the temperature and salinity gradient, thus reducing the bias below 3000 m depth, especially in the simulation with strong bottom mixing, small-scaleEXP. As a trade-off, at depths around 1000 m the tidal simulations are warmer and less dense compared to both CtrEXP and WOA98. At these depths the tidal experiments should have mixing equal to Ctr, hence we could expect a similar bias. However this is not entirely true, one reason being that bottom tidal mixing decays with an e-folding scale of 500 m, and second reason being that tidal mixing occurs in coastal and shallow regions as well. So, larger bias at these depths in the tidal simulations could be due to either too strong coastal tidal mixing, or too large vertical decay scale of tidal mixing (ζ in Eq. 2.3). The latter is supported by other studies (Muller and Bühler, 2009) according to which, tidal mixing is more confined to the bottom than usually assumed. Reducing ζ is difficult to realize in MPIOM, whose vertical resolution is larger than 300 m below 3000 m depth.

The above outcomes are revealed altogether in the global density bias (Fig. 2.9): the enhancement of bias above 2500 m depth, and the reduction of bias below 3000 m depth in all three tidal simulations. Looking at global temperature and salinity biases

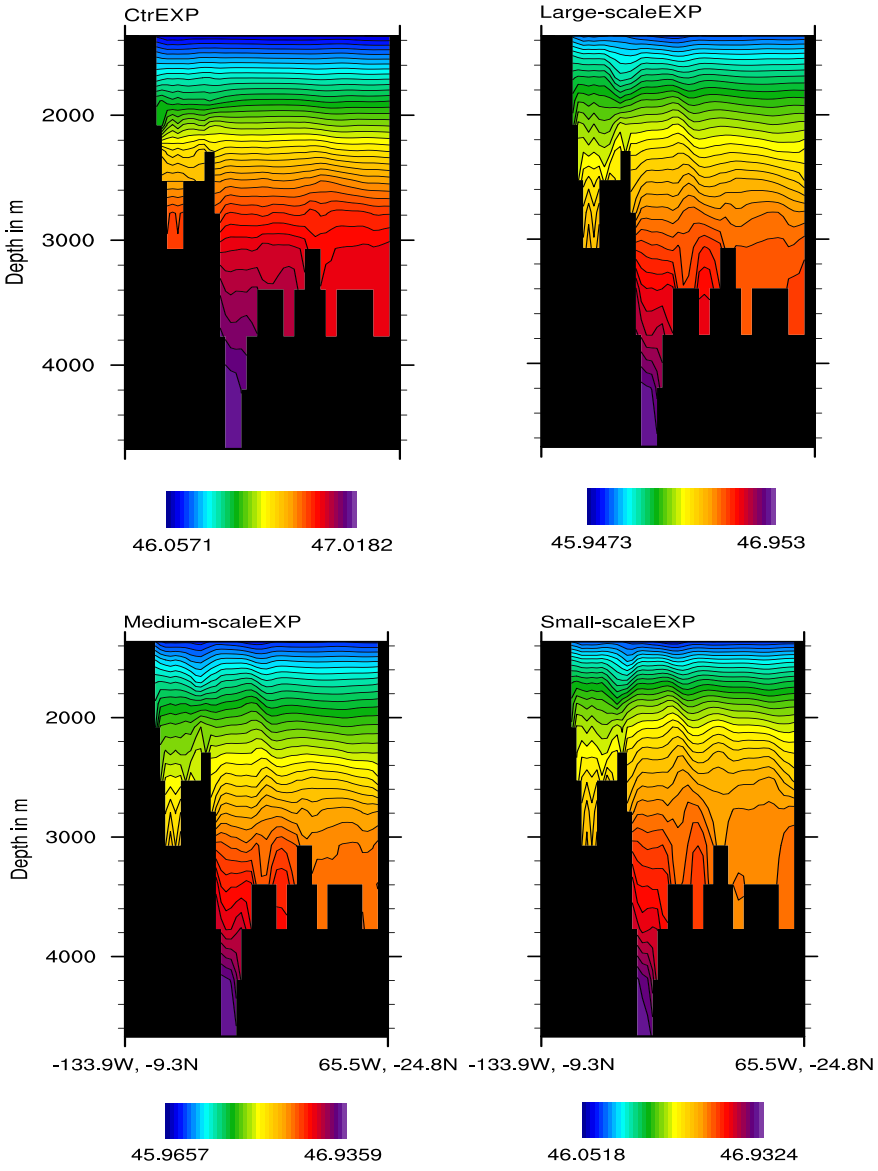

Figure 2.7: Potential density σ_4 (kg m^{-3}) in a vertical section in South Pacific between 9° S and 25° S, a location which is close to the maximum bottom water transport (the longitudes and latitudes of the end points of the section are shown in the x axis). Each plot has different colorbar which is confined between the maximum and minimum of the density value of each experiment in this particular section, and is divided into 40 contours.

(not shown), all tidal simulations, when compared to CtrEXP, reduce the salinity bias everywhere, as well as the temperature bias below 3000 m. The increase of the density bias at 1000 m in the tidal runs originates from the increase in the temperature bias. It is apparent from the global bias that small-scaleEXP performs better than the other

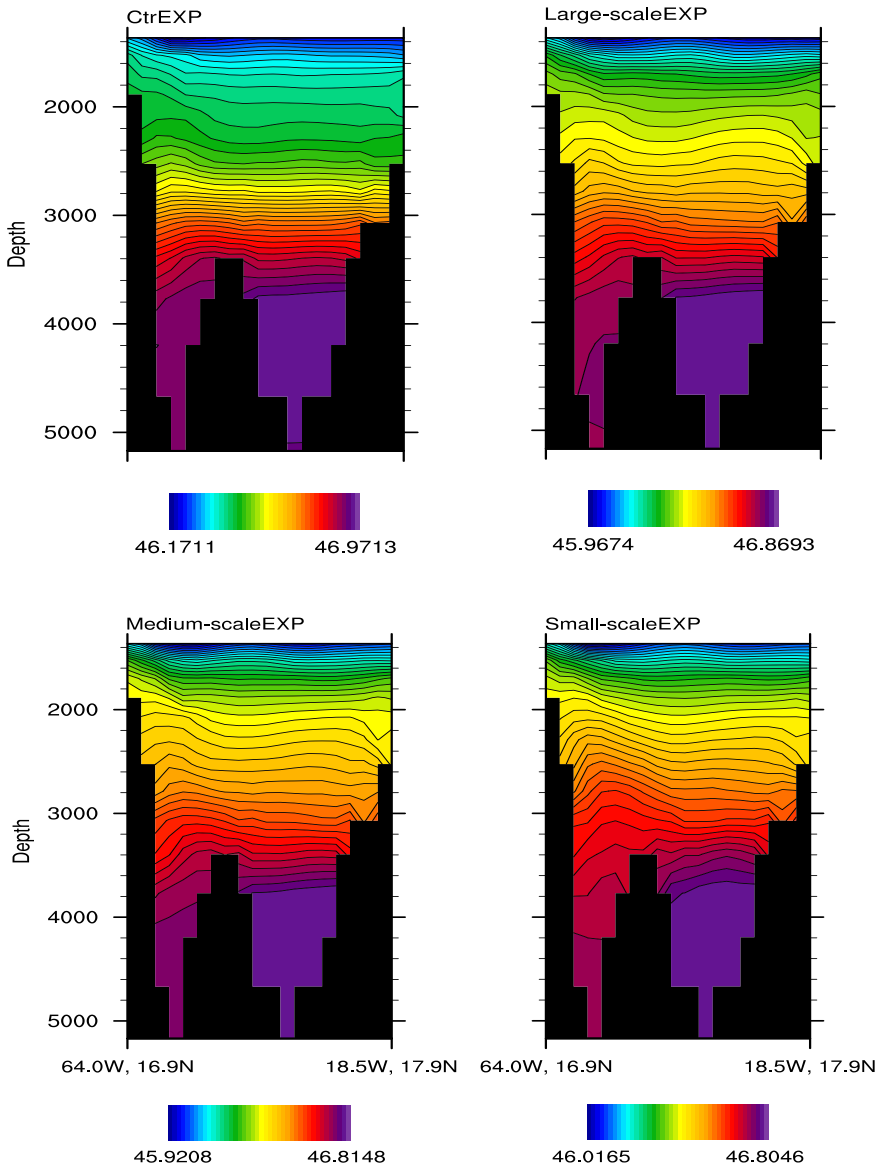

Figure 2.8: Potential density σ_4 (kg m^{-3}) in a vertical section in North Atlantic around 17° N, a location which is close to the maximum of the AABW transport (the longitudes and latitudes of the end points of the section are shown in the x axis). Each plot has different colorbar which is confined between the maximum and minimum of the density value of each experiment in this particular section, and is divided into 40 contours.

two tidal runs in the sense that it has the smallest increase of the bias at 1000 m, and at the same time the smallest bias of all experiments at the deep and bottom waters.

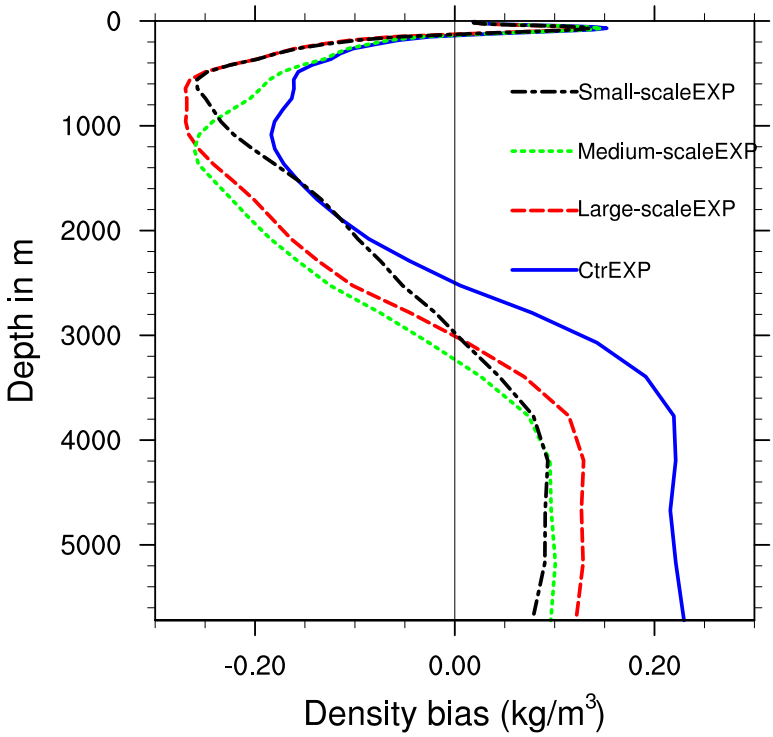

Figure 2.9: Global average of potential density σ_4 bias (defined as the departure from WOA98 climatology) in kg m^{-3}.

2.7 Conclusions and discussion

The current study discusses the effects of the tidal mixing parameterization proposed by Laurent et al. on the MPI-Ocean Model MPIOM. This scheme produces spatial variations of diapycnal diffusivity depending on the locations of tidal energy dissipation over rough topography. We examine the sensitivity of the model results on the spatial scales of the modeled bottom roughness. Four experiments were carried out: three experiments with the tidal mixing scheme and bottom roughness calculated at low, medium and high resolution (large-scaleEXP, medium-scaleEXP and small-scaleEXP), and a fourth experiment with the standard configuration and the same background diffusivity as in the tidal experiments (CtrEXP).

1. The first result is that all three tidal simulations have different equilibrium solutions for the circulation. The strength of the bottom circulations increases with decreasing roughness length, whereas the AMOC behaves in a more complex manner: it increases everywhere in large-scaleEXP, increases only at depths between 1000-3000 m in medium-scaleEXP, and decreases at depths between 2000-3000 m in small-scaleEXP. It is not straightforward, hence, to implement the tidal mixing scheme, due to the sensitivity of the results on the formulation of bottom rough-

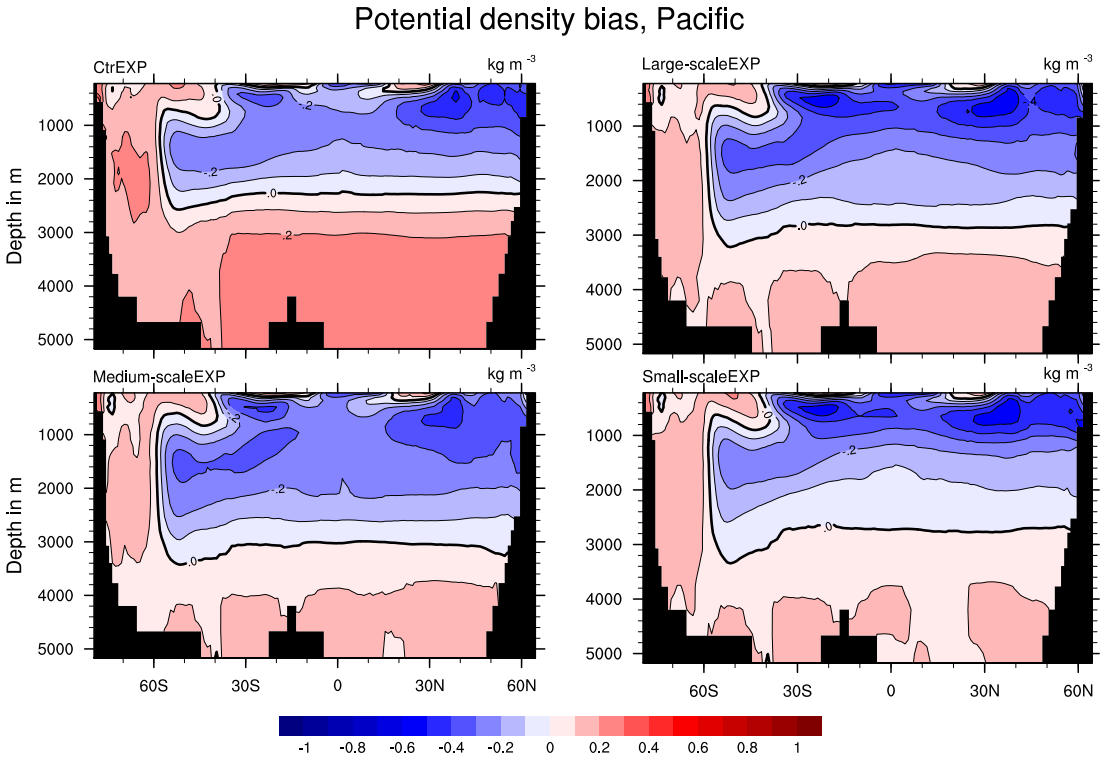

Figure 2.10: Potential density σ_4 bias (defined as the departure from WOA98 climatology) zonally averaged in the Pacific Ocean. Contour interval is 0.1 kg m^{-3}.

ness. To our knowledge, such a sensitivity on the modeled roughness has not been tested and discussed in any other modeling study using OGCM. Previous studies that used the same tidal mixing scheme (Simmons et al., 2004; Saenko and Merryfield, 2004) have used the same modeled roughness built-in the energy conversion map, taken from Jayne and Laurent.

2. The second result is that the changes in the bottom circulation in the tidal simulations are not driven by tidally induced changes in convection. The popular concept of direct relationship between convection and circulation strength is counteracted here. Instead, we find that local changes in water masses properties affect bottom circulation, without necessarily convection having to play a dominant role.

3. The third result is that all the tidal simulations reduce the bias of the model at big depths, and increase it at intermediate depths. Among the tidal simulations, the one based on small-scale roughness produces the smallest biases.

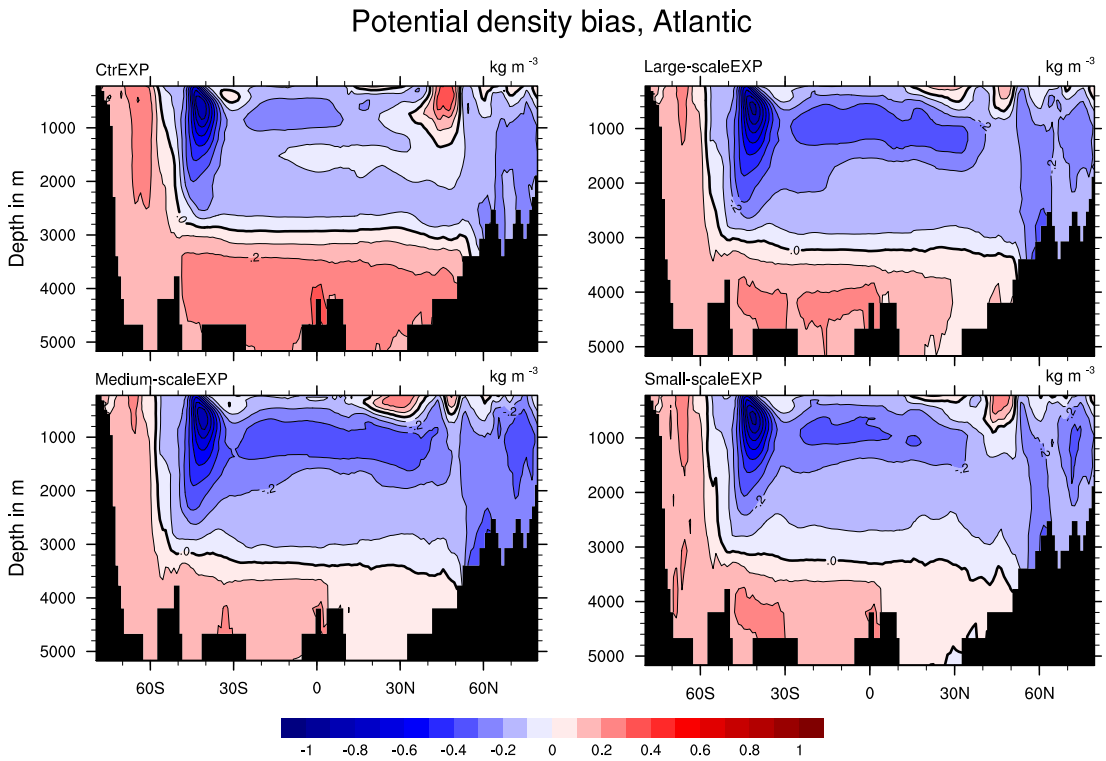

Figure 2.11: Potential density σ_4 bias (defined as the departure from WOA98 climatology) zonally averaged in the Atlantic Ocean. Contour interval is 0.1 kg m^{-3}.

Chapter 3

The effect of tidally driven mixing on the transient climate response to CO_2 increase

3.1 Introduction

Several coupled atmosphere-ocean general circulation models are being used for simulations of the climate change with different emission scenarios. The results of these simulations are synthesized into collective synthesis reports in the Intergovernmental Panel for Climate Change (IPCC[1]). Part of these simulations are focused on the time-evolving climate change, rather than the equilibrium climate change, because the immediate societal interest is on the near present rather than on the distant future. The simulated transient climate changes (referred to as 'responses') of different models, quantified through metrics such as global-mean surface temperature, Atlantic thermohaline circulation, sea-ice cover etc., vary significantly from one model to another. For example, the range in temperature change at the end of the 21st century under the B1 emission scenario is about $1.2° - 3.2°$ C, implying a $2°$ C multi-model ensemble spread. Under different emissions scenarios, the multi-model ensemble spread ranges from $2°$ to $2.5°$ C (Solomon et al., 2007, pp. 763). In addition to the differences in the global-mean surface temperature change, there are differences in the temperature change patterns among different models. The magnitude of the polar amplification, measured by the ratio of high latitude warming to the global-mean warming, varies among models from 1.5 to 4.5 times the global-mean warming (Holland and Bitz, 2003). Disagreement in polar amplification among models is associated with disagreement in the sea ice thinning (Solomon et al., 2007, pp. 771). Even though coupled models agree on some common features in polar climate change, such as arctic sea ice decaying much faster than antarctic sea ice, and northward heat transport increasing in the northern high latitudes, models produce a large range on their quantitative predictions on sea-ice area reduction and sea ice melting.

Changes in surface climate quantities, like temperature or sea-ice conditions, are significantly influenced by changes in the ocean. For example, the overturning circulation

[1] http://www.ipcc.ch/

(MOC), through its control on meridional ocean heat transport, affects sea-ice conditions, hence the polar climate response. The MOC also affects vertical ocean heat fluxes, hence the ocean heat uptake, which in turn affects the transient near-surface air temperature response. Therefore, large uncertainties among model predictions arise from their large disagreement in the circulation response. For example, common feature among all models simulating the transient climate change is a reduction in the Atlantic MOC, that is caused by reduced convection due to warming and freshening of the high-latitudes ocean. However, models disagree on how strong this reduction is: it can be very small (indistinguishable from natural variability) ranging up to 50% or more (Gregory et al. (2005), also Fig. 3.1, taken from Solomon et al. (2007)).

The strength of the MOC, hence the meridional ocean heat transport, are strongly dependent on the choice of the vertical or diapycnal diffusivity (Bryan, 1987; Zhang et al., 1999; Marotzke, 1997; Scott and Marotzke, 2002). Observations (Toole et al., 1994; Polzin et al., 1997; Ledwell et al., 2000) indicate that diapycnal diffusivity is highly variable in space; over most of the ocean area it is weak, around $10^{-5}\,\mathrm{m^2 s^{-1}}$, but over rough topography the diffusivity values are several order of magnitude larger. Large diffusivity comes from enhanced turbulent mixing over rough topography. The enhanced turbulent mixing is considered to result mainly from the dissipation of internal waves, that originate from barotropic tides through their interaction with rough topography. Diapycnal diffusivity, therefore, is highly spatially inhomogeneous, due to the mixing induced by dissipation of tides in the ocean.

At present, most Ocean General Circulation Models (OGCMs), do not take the spatial inhomogeneity of diapycnal diffusivity into account; instead, they represent diffusivity with a spatially constant value. Implementing a more physically based, spatially-variable diffusivity in models has significant impacts on the simulated ocean circulation (Hasumi and Suginohara, 1999; Simmons et al., 2004; Saenko and Merryfield, 2004; Montenegro et al., 2007; Huang and Jin, 2007; Jayne, 2009; Exarchou et al., 2011). The research question we are addressing in the present study is how the differences in ocean circulation due to tidal mixing are affecting the transient climate response to CO_2 increase. We aim with our study, therefore, to quantify the uncertainties in the transient response in the ocean circulation, hence in the surface climate, that are related to tidal mixing in the ocean.

There is one previous study that examined the impact of tidal mixing on the transient climate change (Saenko, 2006); however, the limitation of that study was that it used a highly idealized setting, more specifically, an energy-moisture balance atmospheric model, and an idealized geometry ocean model. For the simulations in our study we use a fully coupled state-of-the-art Atmosphere-Ocean GCM, that is used in IPCC framework studies for future climate projections. To the best of our knowledge, there is no previous modeling study that uses a setting as realistic as in our study, to examine the impact of tidal mixing on the transient climate response to CO_2 increase.

This Section is organized as follows: we introduce the model and setup of the experiments in Section 3.2. In Section 3.3 we describe how the quasi-equilibrium climate produced by the coupled model is modified when the tidal mixing scheme is implemented. In Section 3.4 we discuss the tidal-mixing induced changes in climate response. In Section 3.5 we discuss the role of the ocean heat uptake in the modified transient climate response induced by tidal mixing. In Section 3.6 we discuss the processes responsible for the ocean heat uptake. Finally, we summarize in Section 3.7 and conclude in Section 3.8.

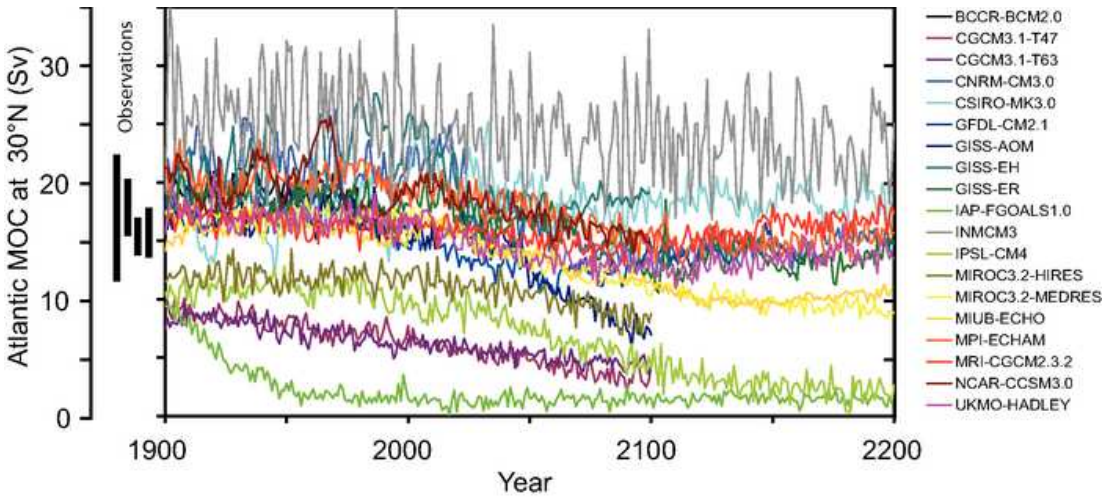

Figure 3.1: Evolution of the Atlantic meridional overturning circulation (MOC) at 30° N in simulations with the suite of comprehensive coupled climate models from 1850 to 2100 using 20th Century Climate in Coupled Models (20C3M) simulations for 1850 to 1999 and the SRES A1B emissions scenario for 1999 to 2100. Some of the models continue the integration to year 2200 with the forcing held constant at the values of year 2100. Observationally based estimates of late-20th century MOC are shown as vertical bars on the left. Three simulations show a steady or rapid slow down of the MOC that is unrelated to the forcing; a few others have late-20th century simulated values that are inconsistent with observational estimates. Of the model simulations consistent with the late-20th century observational estimates, no simulation shows an increase in the MOC during the 21st century; reductions range from indistinguishable within the simulated natural variability to over 50% relative to the 1960 to 1990 mean; and none of the models projects an abrupt transition to an off state of the MOC. (Taken from Solomon et al., 2007, pp. 773).

3.2 Model and experimental setup

3.2.1 Description of coupled ECHAM5/MPIOM

The simulations in this study are performed using the state-of-the art coupled model ECHAM5/MPIOM, developed at the Max Planck Institute for Meteorology (Jungclaus et al., 2006). The coupled model consists of the spectral atmosphere model

ECHAM5 and the ocean general circulation model MPIOM (Marsland et al., 2003). ECHAM5/MPIOM was used for the fourth assessment report on the Intergovernmental Panel for Climate Change (Solomon et al., 2007, IPCC AR4). Here, we use a coarse-resolution version of the coupled model to perform long simulations, of up to 1700 years length.

ECHAM5

ECHAM5 is the 5th generation of ECHAM model series. It has a spectral dynamical core with vorticity, temperature, and logarithmic air pressure represented by a truncated series of spherical harmonics (Roeckner et al., 2003). In our study we use the low resolution ECHAM5, truncated at the T31 spectral coefficient, which corresponds to 3.75° horizontal resolution, and with 19 vertical hybrid sigma pressure levels, that reach up to middle stratosphere (10 hPa). The time-step for ECHAM5 is 20 minutes.

MPIOM

MPIOM (Marsland et al., 2003) is a z-coordinate ocean GCM thats is based on the primitive equations for a hydrostatic Boussinesq fluid on a rotating sphere. It has a bipolar, orthogonal spherical coordinate system on Arakawa C-grid. In our study we use the grid configuration GR30, with the model poles placed over Greenland and Antarctica. The advantage in the choice of the model poles is that first, numerical singularities are avoided, and second, the model resolution is high near deep water formation regions at high latitudes. The horizontal resolution ranges between 28 km near Greenland, and 350 km near the tropical Pacific. The vertical resolution is high near the sea surface (10 m) and gets lower with increasing depth (300 m or more in the deep ocean), distributed in 40 vertical levels. The time-step for MPIOM is 2.4 hours. MPIOM also includes a zero-layer dynamic-thermodynamic sea-ice model with viscous-plastic rheology (Semtner, 1976; Hibler, 1979).

Processes that are not resolved in the coarse horizontal and vertical grid resolution are parameterized. We here briefly summarize some of the parameterizations we employ in our setup. Convection is parameterized using a convective adjustment scheme, described in Marsland et al. (2003). The vertical mixing of momentum and tracers (temperature and salinity) is parameterized following the so-called PP scheme (Pacanowski and Philander, 1981). Isopycnal diffusivity for tracers is parameterized following Griffies et al. (1998). Complementary to the isopycnal tracer diffusion is the scheme of Gent and McWilliams (1990) (GM hereafter), that parameterizes isopycnal advection due to sub-grid scale eddies, and is also implemented in our setup. Finally, in our simulations we use the tidal mixing parameterization of Laurent et al. (2002), in order to investigate the impact of tidal mixing on transient climate change, which constitutes the research goal of the current study.

OASIS

The coupling between the two models is performed every 24 hours using the OASIS coupler (Valcke et al., 2003). The coupler transfers from the atmosphere to the ocean momentum, heat and freshwater fluxes, after interpolating them onto MPIOM grid. From the ocean to the atmosphere the coupler transfers sea surface temperatures, sea-ice thickness and area, snow cover and sea surface velocities. River runoff and glacier calving, which are implemented in the atmospheric model (Hagemann and Dumenil, 1998; Hagemann and Gates, 2003), are passed from the atmosphere to the ocean through the freshwater fluxes. The coupled model does not require any flux adjustment.

3.2.2 Experiments

We perform experiments with two setups of ECHAM5/MPIOM, one setup with the tidal mixing scheme, and the second setup with the standard configuration. We refer to the two setups as TID and CTR hereafter. We discussed in detail the implementation of the tidal mixing scheme in MPIOM in Chapter 2. The implementation of the scheme to the coupled model and the choice of parameter values are performed exactly as in the uncoupled simulations of Chapter 2. Additionally, we choose here to represent the bottom roughness as the room-mean-square residuals from smoothed surfaces onto the model grid. Furthermore, in both CTR and TID the background diffusivity is equal to $10^{-5}\,\mathrm{m^2\,s^{-1}}$.

Both TID and CTR are run with pre-industrial CO_2 concentration (278 ppmv) until quasi-equilibrium is reached (spin-up runs). There is no single strict criterion for quasi-equilibrium. Instead, we arbitrarily determine the length of the spin-up runs by looking that the trends of different quantities at different ocean depth levels are adequately small. The length of the CTR spin-up is 1000 years, and of the TID spin-up is 1200 years. In Section 3.3, where we discuss the quasi-equilibrium climates of TID and CTR, we discuss the time-means of the last 200-years of the spin-up runs. We hereafter refer to the experiments in quasi-equilibrium as $\mathrm{TID_{1CO2}}$ and $\mathrm{CTR_{1CO2}}$.

We mention here that TID and CTR do not have equal global-mean diffusivity. To cover this gap, we performed a third experiment with the standard configuration but large background diffusivity ($10^{-4}\,\mathrm{m^2\,s^{-1}}$), equal to the TID global-mean diffusivity. However, we do not discuss in our study this additional experiment, because it produces unrealistically high global-mean near-surface air temperature (SAT) in its quasi-equilibrium state, equal to 17.5 °C. For comparison, the observed global-mean SAT for the commonly used base period of 1951-1980 is estimated to be 14 °C[2]. The other two experiments have realistic global-mean SAT: 13.9 °C for $\mathrm{CTR_{1CO2}}$ and 14.4 °C for

[2]IPCC 1995, also http://earthobservatory.nasa.gov/Features/WorldOfChange/decadaltemp.php

TID_{1CO2}.

After the spin-up runs, we increase the CO_2 concentration by 1% per year until CO_2 doubling (556 ppmv) in 70 years. After year 70, we keep CO_2 constant to 556 ppmv for another 430 years. In total, the entire period of increased CO_2 forcing lasts 500 years. We refer to the first 100 years as the 'transient' period, and the next 400 years as the 'post-transient' period. The choose the term post-transient phase for the last 400-years for two reasons: first, we avoid to call it also transient, because this term is commonly used in literature to characterize the time period during the CO_2 increase, but not the period after CO_2 stabilization. Second, because the climate is not in quasi-equilibrium yet, but it is still drifting, so it is still in a kind of "transient" mode. For the latter reason, during the whole 500-year period, for each setup we take ensemble-means of three runs, so as to minimize natural variability.

In Section 3.4, we discuss the tidal-mixing induced changes in the transient climate response. 'Response' is defined as the difference between the post-transient and quasi-equilibrium experiments. Post-transient experiments are time-means of the last 100 years of the post-transient phase (we refer to post-transient experiments as 'EXP_{2CO2}'). We also discuss the first 10 and last 10 years of the transient period in Section 3.6. We refer to the experiments at these periods as 'EXP_{TRANS1}' and 'EXP_{TRANS2}' (where EXP is either TID or CTR).

Also, for easy reference, a graphical overview of the experiments performed in this study is shown in Fig. 3.2 and the experiments are summarized in Table 3.1.

EXPS	$1\times CO_2$	TRANS1	TRANS2	$2\times CO_2$
Years	$-200-0$	$0-10$	$90-100$	$400-500$

Table 3.1: Time-periods of the experiments considered in our study. Year zero is the year of initialization of the CO_2 increase, negative numbers indicate years from the spin-up integrations.

3.3 Quasi-equilibrium climate produced by the coupled ECHAM5/MPIOM model with the tidal mixing

In this Section we discuss the large-scale characteristics of the quasi-equilibrium climates of TID and CTR. We focus particularly on the mass and heat meridional transports, on the temperature and salinity distributions in the ocean, as well as on the sea-ice conditions and the near-surface temperatures.

3.3.1 Meridional mass transports

We discuss the quasi-equilibrium mass transports, expressed in the form of the zonally integrated stream function (in Sv = 10^6 m^3/s), in the two major basins and in the

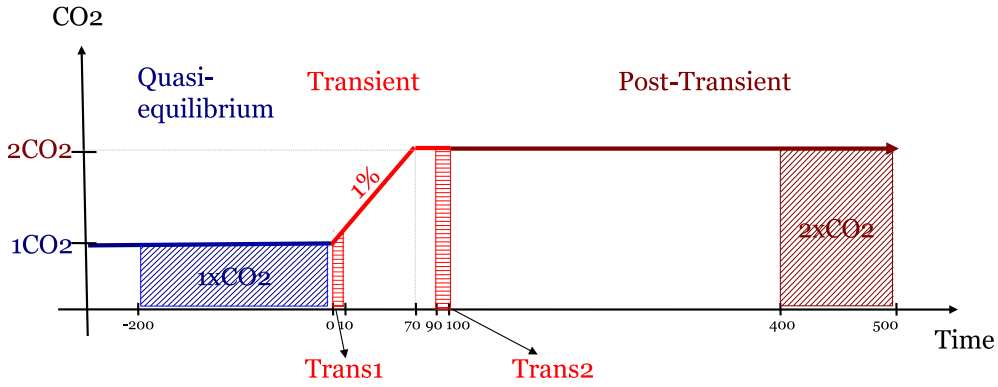

Figure 3.2: Graphical overview of the experiments performed in this study. Blue color is used for marking the time period of the spin-up integration when quasi-equilibrium is reached (at $1CO_2$), the light red color for marking the period of the transient climate (70-year long), and the red color for marking the period after the transient climate (430-year long time period). The climate of the latter time period is referred to as 'post-transient' for two reasons: first, in order to differentiate it from the 70-year period of CO_2 increase, and second, because it is not in quasi-equilibrium yet. Year zero is the year of the beginning of CO_2 doubling. Four time periods are discussed in the text: The first period is the last 200 years of the spin-up integrations, when the quasi-equilibrium at pre-industrial CO_2 is reached. Experiments at this period are being referred to as 'EXP_{1CO_2}' in the text. The second and third periods are years $0-10$ and $90-100$. Experiments at these periods are named 'EXP_{TRANS1}' and 'EXP_{TRANS2}', respectively. The fourth period is years $400-500$. Experiments here are named 'EXP_{2CO2}'. ('EXP' is either CTR or TID).

Global Ocean. Positive stream function values imply clockwise and negative values counter-clockwise transports. The unit (Sv) is implying volume transport, however we refer to is as mass transport, since volume and mass are linearly related with a near-constant density.

Atlantic

In the Atlantic Ocean, the meridional overturning circulation produces two distinct overturning cells. The upper cell is representative of the southward flow of the North Atlantic Deep Water (NADW) formed in the North Atlantic. The lower cell characterizes the northward flowing Antarctic Bottom Water (AABW) that is formed in the Southern Ocean. In CTR_{1CO2} the maximum NADW transport reaches 18.9 Sv (1 Sv $= 10^6\,m^3s^{-1}$) at 30° N and 1000 m depth, and it transports 16 Sv over the equator to the Southern Hemisphere (SH) (Fig. 3.3, top panel). The maximum AABW transport is 2.7 Sv at 6° N and 3600 m depth. In TID_{1CO2} the structure remains the same, but both overturning cells have stronger transports, by 3.2 Sv (+17%) in the upper cell and by 1.2 Sv (+44%) in the lower cell (Fig. 3.3, middle and bottom panels). Similar results for the tidally induced changes in the Atlantic circulation were found in the uncoupled MPIOM experiments in Chapter 2 (Exarchou et al., 2011).

Indo-Pacific

In the Indo-Pacific Ocean of CTR_{1CO2} there are shallow overturning cells close to the surface, and a deep overturning cell between 2500 and 5000 m depth (Fig. 3.4a). This deep cell represents the northward transport of bottom water that is formed in the Southern Ocean through deep convection. The maximum bottom water transport is 3.9 Sv at 30° S and 4000 m depth. Of these bottom water masses, 3 Sv are transported northward to the equatorial regions. From these latter masses, 2 Sv upwell from bottom to 3000 m depth, and another 1 Sv upwells from bottom to the surface. In TID_{1CO2} the pattern is similar to CTR_{1CO2}, but the transports are greatly enhanced, particularly between 30° S and 30° N (Fig. 3.4, middle and bottom panels). The maximum stream function value of TID_{1CO2} reaches 8.6 Sv (+120%) at 20° S and 3600 m depth, of which 5 Sv upwell from bottom to the surface. The same enhancement in the Indo-Pacific mass transports was observed in the uncoupled experiments in Chapter 2 (Exarchou et al., 2011).

CTR_{1CO2} underestimates the bottom water transports in the Indo-Pacific Ocean by 7 Sv or more compared to observations (Talley et al., 2003). The enhanced indo-pacific bottom water transport in TID, therefore, represents an improvement in the model solution, since it is significantly closer to the observations. Observational estimates from Talley et al. yield 10 Sv of maximum bottom water transport occurring between $3000 - 4000$ m depth at 30° S in the Info-Pacific. Their estimate is only 2 Sv more than the corresponding value in TID_{1CO2}. Observations also estimate that 6 Sv of bottom water upwell up to 1500 m depth. In the solution of TID_{1CO2} the respective number is 5 Sv. The Info-Pacific overturning circulation is, therefore, very sensitive to diapycnal diffusivity; in addition, TID_{1CO2} improves the simulated circulation of the Info-Pacific Ocean.

Similar findings have been reported in past studies: Saenko and Merryfield (2004) implemented the same tidal mixing scheme as in our study in a coupled global GCM and found that the Info-Pacific bottom water transport in their model was greatly enhanced with the tidal scheme, but practically non-existent without it. Furue and Masahiro (2005) used a vertically varying and horizontally homogeneous diffusivity in an idealized model and found that the deep Info-Pacific circulation was maintained by the Info-Pacific mid-depth diffusivity. When the latter was reduced to a background value, the effect was global: the Info-Pacific circulation of their model was greatly reduced, as well as the NADW and AABW production. Since the scope of our study is to examine the role of tidal mixing not in the quasi-equilibrium but in the transient climate after CO_2 doubling, our interest focuses on whether the runs are able to reproduce realistic meridional mass transports for Info-Pacific and Atlantic. We find that both runs manage to reproduce sufficiently realistic transports, within the uncertainties of observational estimates (Talley et al., 2003), and consistent with other studies and with

the uncoupled experiments of Chapter 2 (Exarchou et al., 2011).

Global

The combined effects of the circulation patterns in both Atlantic and Info-Pacific appear in the global overturning circulation (Fig. 3.5). Two distinct overturning cells, the upper one being confined above 3000 m depth and the lower one below 3000 m, represent, respectively, the transport of water masses of North Atlantic and Antarctic origin. As it is the case in the Atlantic and the Info-Pacific, $\mathrm{TID}_{1\mathrm{CO2}}$ has significantly stronger transport in the World Ocean than $\mathrm{CTR}_{1\mathrm{CO2}}$, by 3.7 Sv (+21%) in the upper cell at 24° N and by 6 Sv (+78%) in the lower cell at 35° S. The differences in the lower cell, as also seen in Atlantic and Info-Pacific, are much more pronounced than the upper cell differences. This means that $\mathrm{TID}_{1\mathrm{CO2}}$ is much more efficient in producing and transporting AABW.

The connection between enhanced diffusivity and enhanced bottom water transports, has been predicted from theoretical arguments and tested in past modeling studies. Kamenkovich and Goodman (2000) found, using theoretical arguments, that the AABW transport intensifies with increasing diffusivity (assumed to be spatially constant) because of the increase in the meridional density gradient, which drives the flow. At low latitudes, enhanced diapycnal mixing leads to more heat being diffused at large depth, creating lighter water, which then upwells. The upwelling at low latitudes is balanced by enhanced AABW transport. Ito and Marshall (2008) developed a theoretical model based on residual-mean theory and found that the strength of the bottom overturning is proportional to the square root of the diapycnal diffusivity, and the mesoscale eddy transfer. The authors further support their arguments using an idealized OGCM.

Previous studies (Park, 1999; Thorpe et al., 2001) suggest that, in a geostrophic flow, there is a linear relation between zonal and meridional pressure gradients, implying that there is relationship between the meridional pressure gradient and the overturning strength. The differences in bottom water transports in our experiments can be then explained by different meridional pressure gradients. The latter, through the hydrostatic balance, can be expressed by the depth integrated meridional density gradients, between low and high latitudes. The meridional density gradient, in turn, can be expressed in terms of the steric height h, defined as

$$h(z_1, z_2) = \int_{z1}^{z2} \Delta\rho/\rho_0 \, \mathrm{d}z, \tag{3.1}$$

where $\Delta\rho$ is the zonally-averaged density difference between two latitude bands, ρ_0 is a reference density, and z_1 and z_2 are two depth levels. Calculating the steric height, integrated between the depth levels 3000 and 5500 m (where the bottom water of Antarctic origin is being transported), and $\Delta\rho$ is calculated as the difference between zonally aver-

aged density at the equator and at $40-80^\circ$ S, yields $h_{\mathrm{CTR}} = 2.09\,\mathrm{m}$ and $h_{\mathrm{TID}} = 2.98\,\mathrm{m}$ (+42% compared to $\mathrm{CTR}_{1\mathrm{CO2}}$). So, even though $\mathrm{TID}_{1\mathrm{CO2}}$ is overall less dense than $\mathrm{CTR}_{1\mathrm{CO2}}$ (Fig. 3.6), its steric height, hence its meridional density gradient, is stronger than in CTR, leading to stronger bottom circulation.

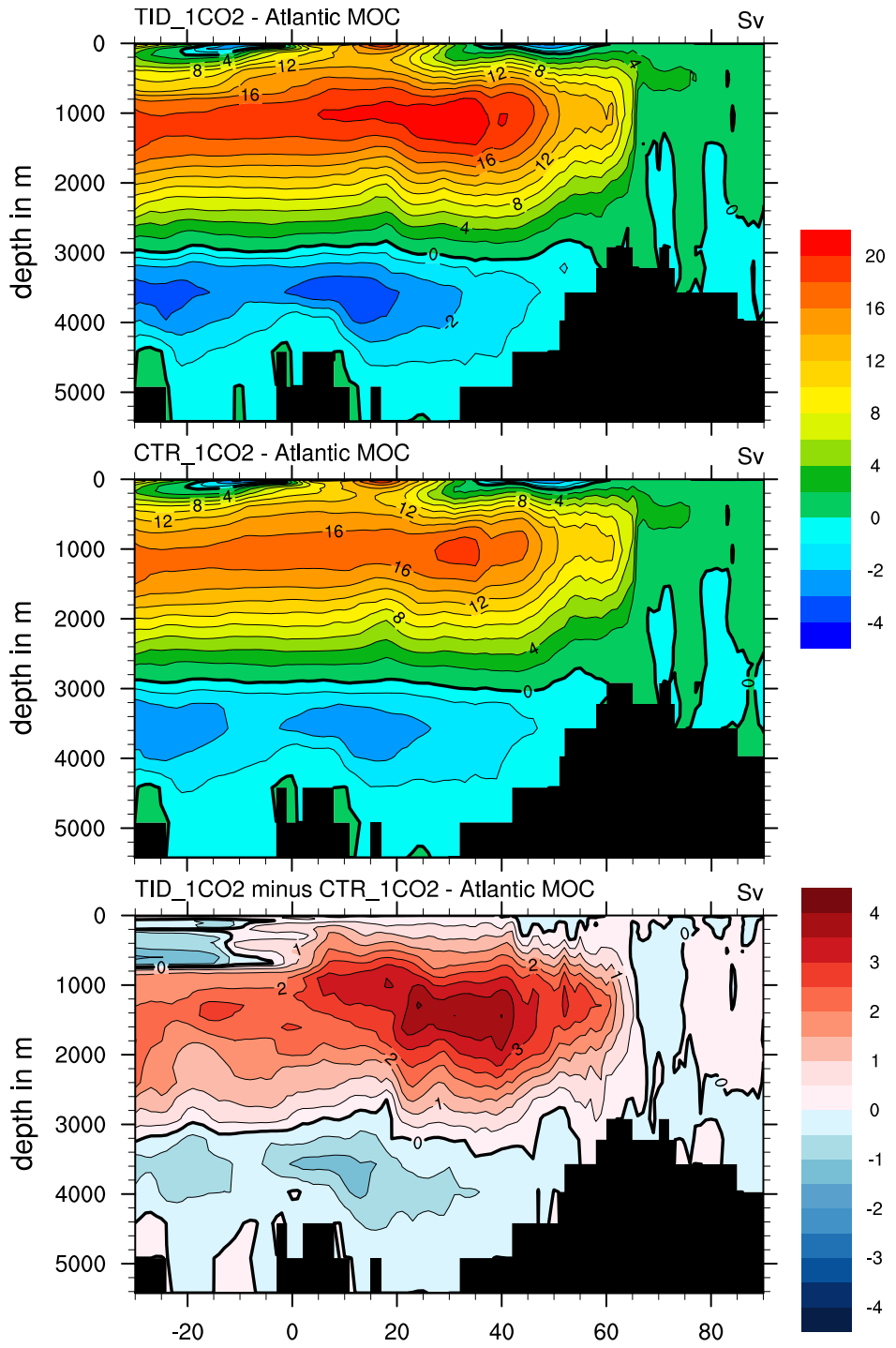

Figure 3.3: Atlantic meridional overturning stream function in Sv for $\mathrm{TID}_{1\mathrm{CO2}}$ (top), $\mathrm{CTR}_{1\mathrm{CO2}}$ (middle), and their difference (bottom). (Contour interval in top two plots: 1 Sv for negative and 2 Sv for positive values. In bottom plot: 0.5 Sv).

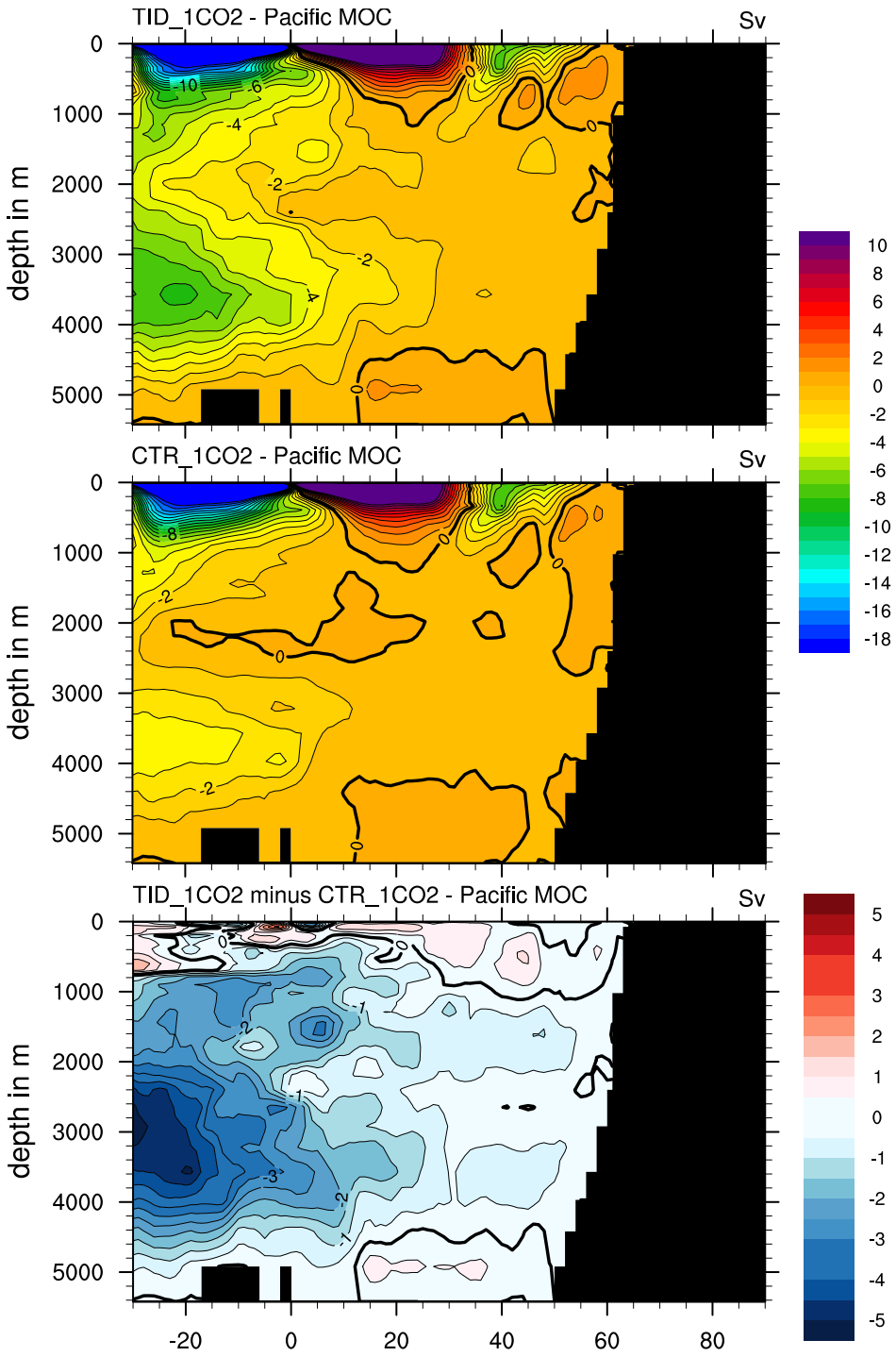

Figure 3.4: Indo-pacific meridional overturning stream function in Sv for $\mathrm{TID}_{1\mathrm{CO2}}$ (top), $\mathrm{CTR}_{1\mathrm{CO2}}$ (middle), and their difference (bottom). (Contour interval in top two plots is 1 Sv, in bottom plot is 0.5 Sv).

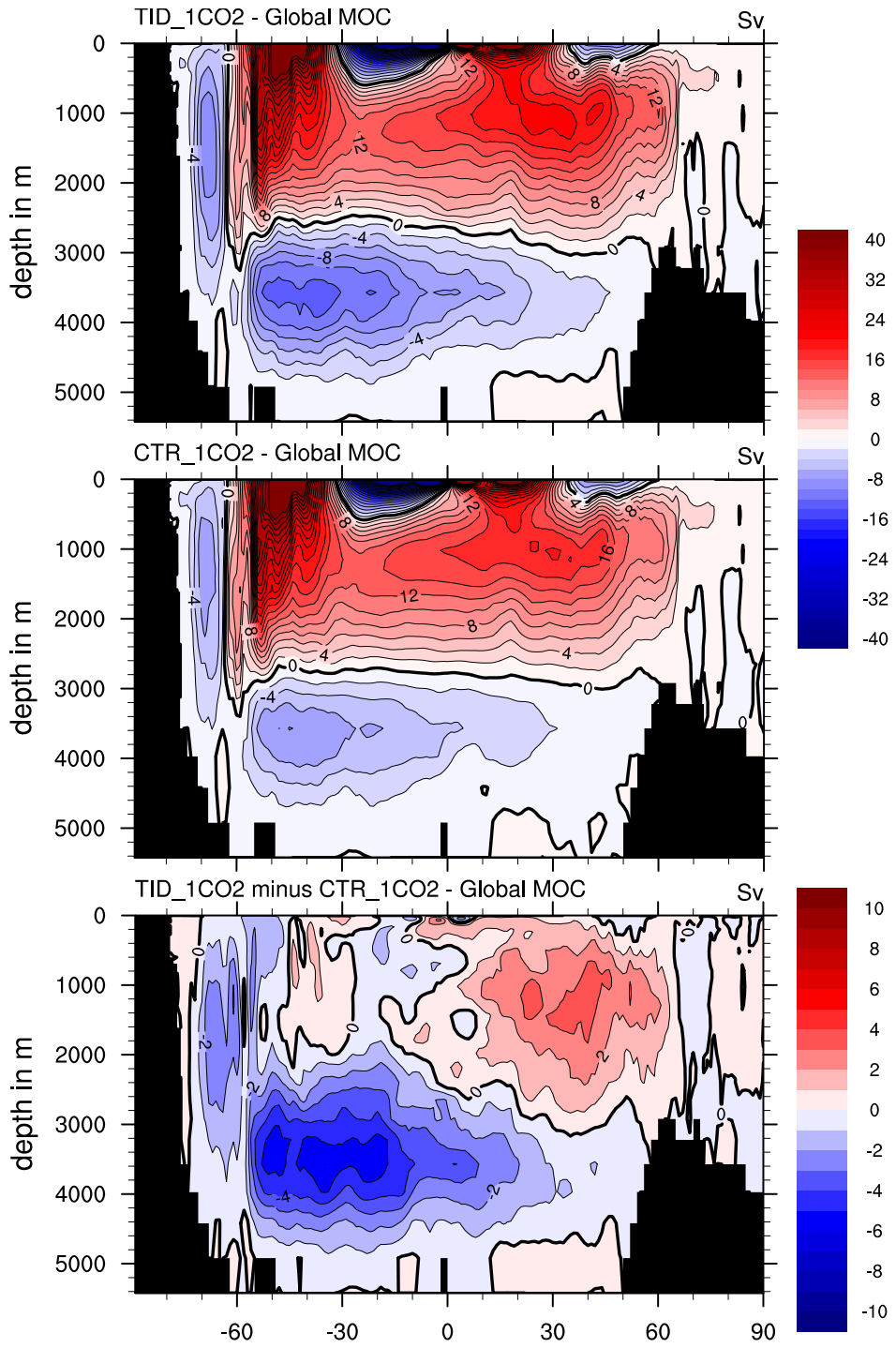

Figure 3.5: Global meridional overturning stream function in Sv for $\mathrm{TID}_{1\mathrm{CO2}}$ (top), $\mathrm{CTR}_{1\mathrm{CO2}}$ (middle), and their difference (bottom). (Contour interval in top two plots is 2 Sv, in bottom plot is 1 Sv).

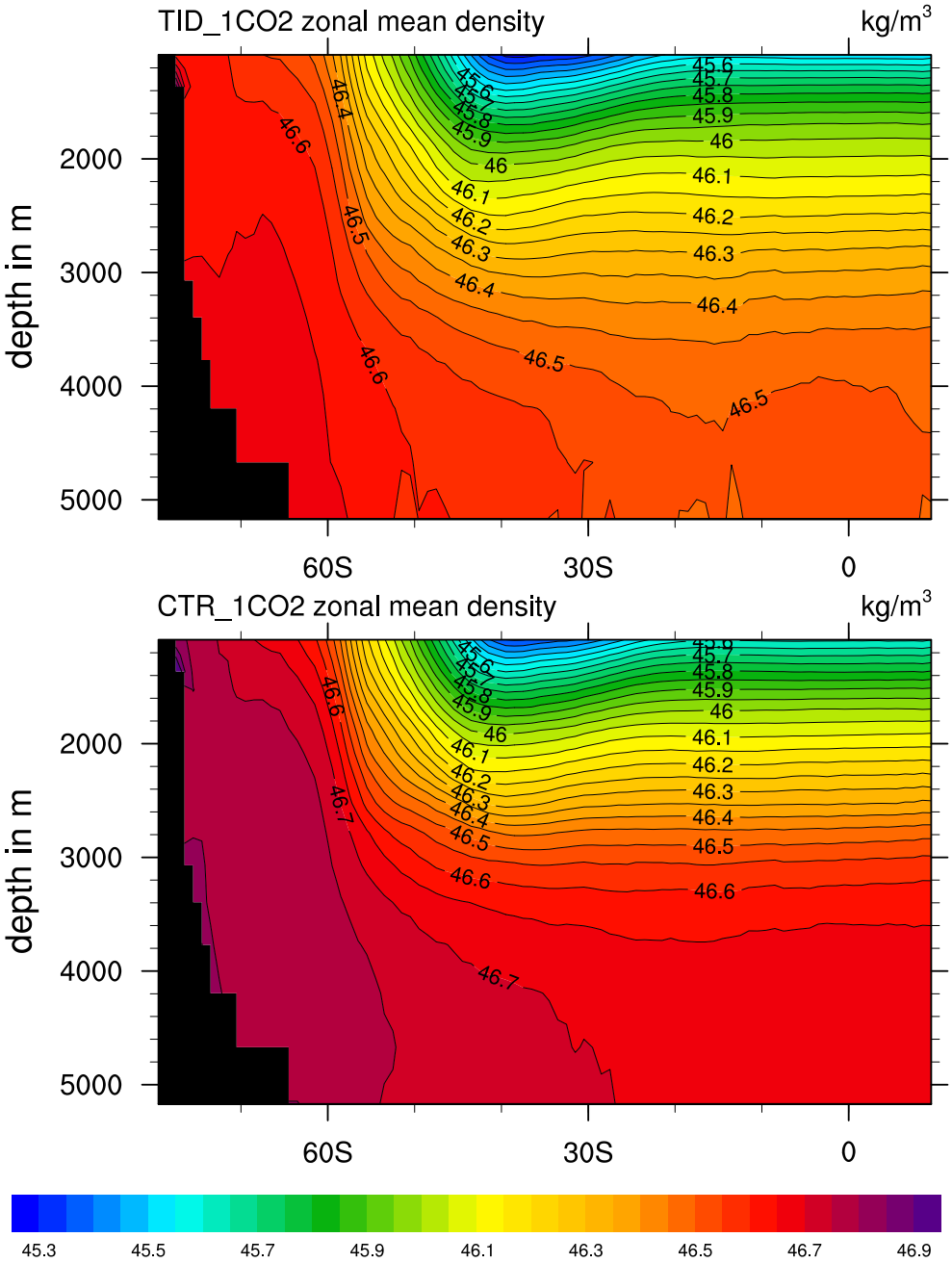

Figure 3.6: Zonal-mean density (potential density σ_4, referenced at 4000 m depth) for the SH, for $\mathrm{TID}_{1\mathrm{CO2}}$ (top) and $\mathrm{CTR}_{1\mathrm{CO2}}$ (bottom). Contour interval is 0.05 kg m^{-3}.

3.3.2 Meridional heat transports

The differences in heat transports between CTR and TID (bottom panel of Fig. 3.7) are consistent with the changes in their meridional mass transports. The mass transports are enhanced in all basins in TID_{1CO2}, transporting therefore more heat in the ocean. The difference between TID_{1CO2} and CTR_{1CO2} in Fig. 3.7 shows that the enhancement of heat transports in TID_{1CO2} is more pronounced in the northern World Ocean (amplitude is larger by 0.1 PW compared to CTR_{1CO2}) rather than in the southern World Ocean (amplitude is larger by 0.07 PW compared to CTR_{1CO2}). The reason is that in the North Hemisphere (NH), there is hardly any difference between the two runs in the NH Pacific, implying that the differences arise from the NH Atlantic only. In the SH, on the other hand, the amplitudes of heat transports in both Southern Pacific and Southern Atlantic increase in TID_{1CO2}. But, the heat transports in the Southern Atlantic are always positive (northward), hence, opposing the negative (southward) Southern Pacific heat transports. The combination of both opposing transports is that the Southern Pacific changes dominate over the Southern Atlantic changes, hence the amplitude of the total heat transport in the SH of TID still increases, but much less compared to the NH.

3.3.3 Temperature and salinity distributions

Temperature

Fig. 3.8 shows the zonal-mean temperature distributions for the World Ocean, as well as the distribution for the Atlantic, Pacific and Southern Ocean. Both TID_{1CO2} and CTR_{1CO2} have stratified temperature fields, with warm upper ocean at low latitudes that gets colder with depth and at higher latitudes.

At the deep ocean, TID_{1CO2} is both more stratified and warmer than CTR_{1CO2} in all basins. The largest warming occurs in North Atlantic around 3500 m depth, where TID_{1CO2} is warmer than CTR_{1CO2} by up to 1.6° C. Larger temperature stratification in TID seems counter-intuitive, since tidal mixing is expected to minimize temperature gradients rather than to enhance them. Warmer deep ocean in TID, on the other hand, can be seen as a direct consequence of tidal mixing: enhanced diffusivity due to tidal mixing leads to more diffusion of heat at large depths.

At the upper ocean there is not much difference between TID and CTR temperatures, with few exceptions at the tropical upper Pacific and subtropical Atlantic, where TID is warmer. Moreover, in regions poleward of 60° N, which is the Arctic Ocean, TID is colder than CTR by up to 0.4° C.

The ocean temperature bias, defined as the departure from its initial climatology (Levitus et al., 1998), in CTR is almost everywhere positive in the global ocean (not shown), meaning that CTR is warmer than observations. TID, which is warmer than

CTR, has therefore even larger positive temperature bias. In the uncoupled model (Chapter 2) the biases were different; in the uncoupled control experiment (equivalent to CTR here) there were too warm water masses in the upper ocean and too cold in the lower ocean. Tidal mixing in the uncoupled simulations modified that bias by having warmer ocean at 1000 m (increasing the bias) as well as in the deep ocean (reducing the bias).

Salinity

Fig. 3.9 shows, in a similar manner as above, the zonal-mean salinity distributions.

At the deep ocean in the global zonal-mean, TID is fresher. In combination with TID being warmer, we can infer that TID, in the deep World Ocean, is less dense (also seen in the zonal-mean density plot in Fig. 3.6). In the NH Atlantic TID is more saline than CTR from surface to bottom everywhere northward of 30° N.

At the upper ocean, TID is more saline than CTR, at tropical-subtropical regions, probably because there is more evaporation than in CTR, as seen also from the warmer ocean temperature at these regions in Fig. 3.8.

The salinity bias in the global ocean of CTR (not shown) is mostly positive (more saline than climatology) with few exceptions in the upper ocean and in the high latitudes, where the bias is negative (fresher than climatology). TID, being fresher than CTR in high latitudes, has larger (negative) bias at these regions. TID is also fresher at mid-latitudes between 1500 and 3000 m, therefore it has smaller (positive) bias there. Overall, the relative differences between TID and CTR in salinity are quite small, hence not affecting significantly the bias.

3.3.4 Sea ice

We now describe changes in sea ice between $\mathrm{TID}_{1\mathrm{CO2}}$ and $\mathrm{CTR}_{1\mathrm{CO2}}$, by discussing summer sea-ice extent and winter sea-ice thickness (Fig. 3.10 and 3.11, respectively).

The simulated sea-ice conditions in the quasi-equilibrium climates are quite different. $\mathrm{TID}_{1\mathrm{CO2}}$ has significantly less sea ice in both polar regions. In more detail, in the NH summer, $\mathrm{TID}_{1\mathrm{CO2}}$ has smaller sea-ice area in the Barents Sea, Baffin Bay at the west coast of Greenland, and along the Arctic coasts. In the SH summer, sea-ice area in $\mathrm{TID}_{1\mathrm{CO2}}$ is smaller everywhere around Antarctica, but mostly in the Weddell and Ross Seas.

In winter, sea ice in $\mathrm{TID}_{1\mathrm{CO2}}$ is thinner almost everywhere in both polar region compared to $\mathrm{CTR}_{1\mathrm{CO2}}$. In the NH winter, $\mathrm{TID}_{1\mathrm{CO2}}$ has smaller thickness by about 0.4 m (-20%) in Labrador Sea, Barents Sea, Bering Sea and at the Arctic coasts. In the SH winter, the thickness is smaller by $0.6 - 0.8$ m ($\sim 25\%$) in the Weddel Sea and by $0.2 - 0.4$ m ($\sim 20\%$) in the rest of the regions surrounding Antarctica.

Smaller sea-ice area and thickness in TID_{1CO2} are possibly associated with the larger meridional heat transports in the World Ocean (Fig. 3.7), which in turn are associated with the stronger meridional mass transports compared to CTR_{1CO2} (Section 3.3.1).

3.3.5 Near-surface air temperature

We describe here the near-surface air temperature (defined as the temperature at 2 m above sea level, abbreviated as SAT) in the quasi-equilibrium climates. In Fig. 3.12 the SAT are plotted for both experiments. It is apparent that TID_{1CO2} is warmer almost everywhere compared to CTR_{1CO2}. The differences are in most of the regions quite small (below 1° C), with some notable exceptions: both polar regions, particularly in Barents Sea and Weddell Sea, Labrador Sea and the North-West Atlantic close to 40° N, are much warmer in TID_{1CO2}. The largest difference occurs in Weddell Sea, where TID_{1CO2} is 5.6° C (+58%) warmer than CTR_{1CO2}. Smaller differences are in Barents Sea (TID_{1CO2} is 2.41° C, or 33%, warmer than in CTR_{1CO2}), and in Labrador Sea and in the North-West Atlantic (TID_{1CO2} is 16% warmer than CTR_{1CO2}).

The temperature differences between TID and CTR in the polar regions are associated with the different sea-ice conditions of the two experiments through the sea-ice albedo feedback mechanism: an initial warming causes sea-ice melting, which in turn enhances the atmospheric warming by reduced albedo, and by larger upward sensible and latent heat fluxes from ocean to the atmosphere (Fig. 3.13). The latter is due to larger open ocean area, that is not being covered by insulating sea ice.

The temperature differences in the mid-latitudes of North Atlantic are related to latent and sensible heat fluxes changes, which in turn are associated with differences in wind stress between the two experiments (not shown). More particular, the wind stress magnitude is larger in TID than in CTR over 30°- 60° N in the Atlantic Ocean.

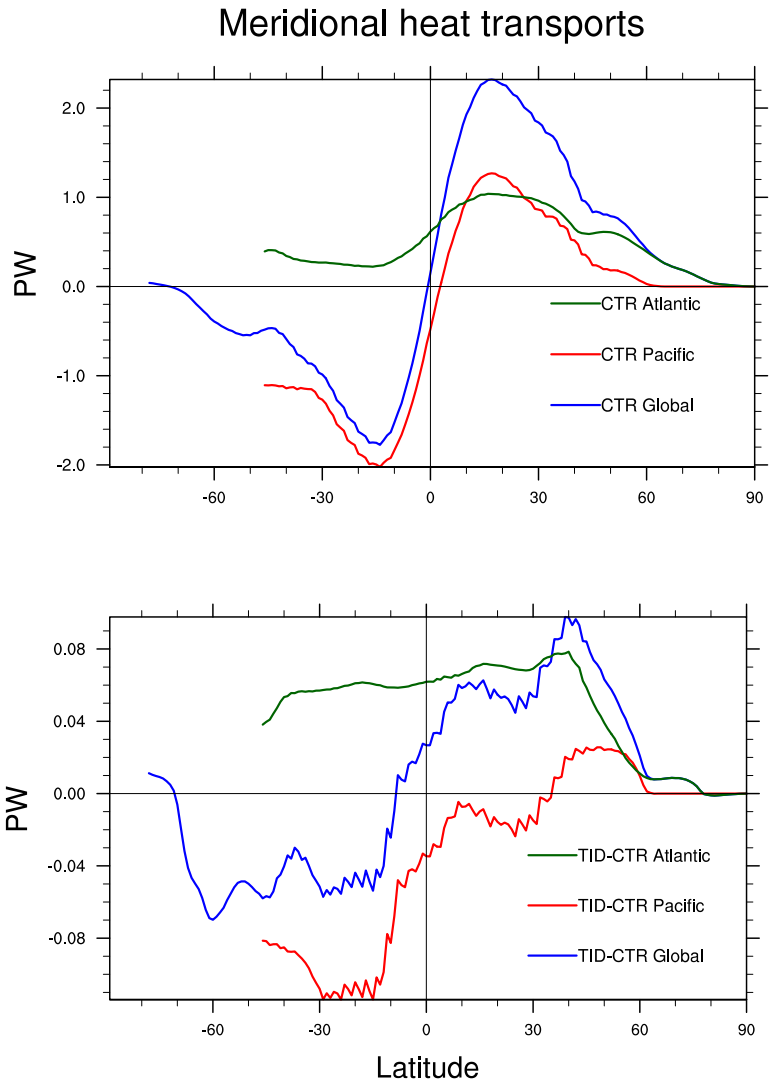

Figure 3.7: Meridional heat transports (PW) for the World Ocean (blue), Atlantic (green) and Pacific (red), for CTR_{1CO2} (top) and for the difference TID_{1CO2}-CTR_{1CO2} (below).

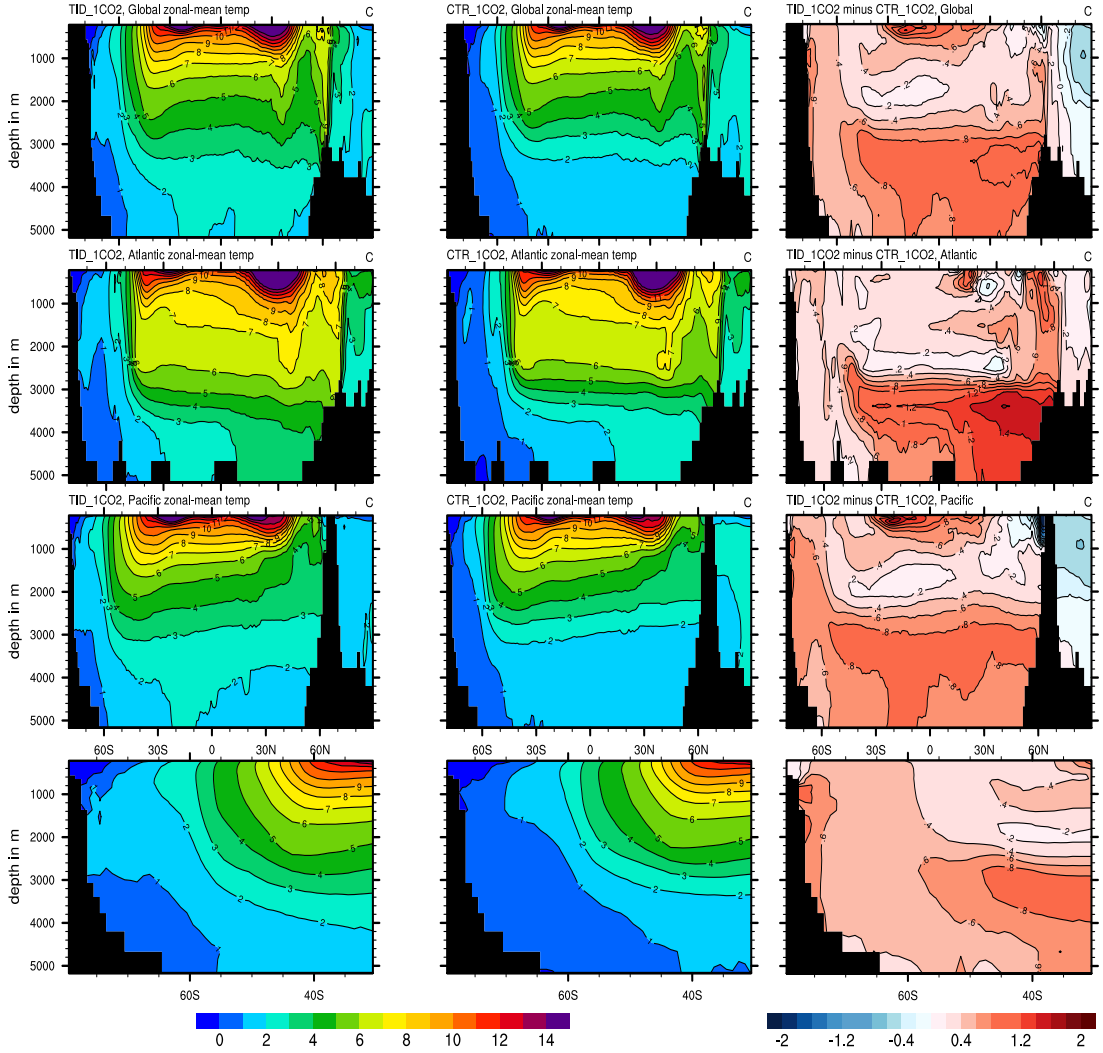

Figure 3.8: Zonal-mean ocean temperature (in °C), for (from top to bottom row): World Ocean, Atlantic, Pacific, and Southern Ocean. Left is $\mathrm{TID}_{1\mathrm{CO2}}$, middle is $\mathrm{CTR}_{1\mathrm{CO2}}$, and right is their difference: $\mathrm{TID}_{1\mathrm{CO2}}$ minus $\mathrm{CTR}_{1\mathrm{CO2}}$.

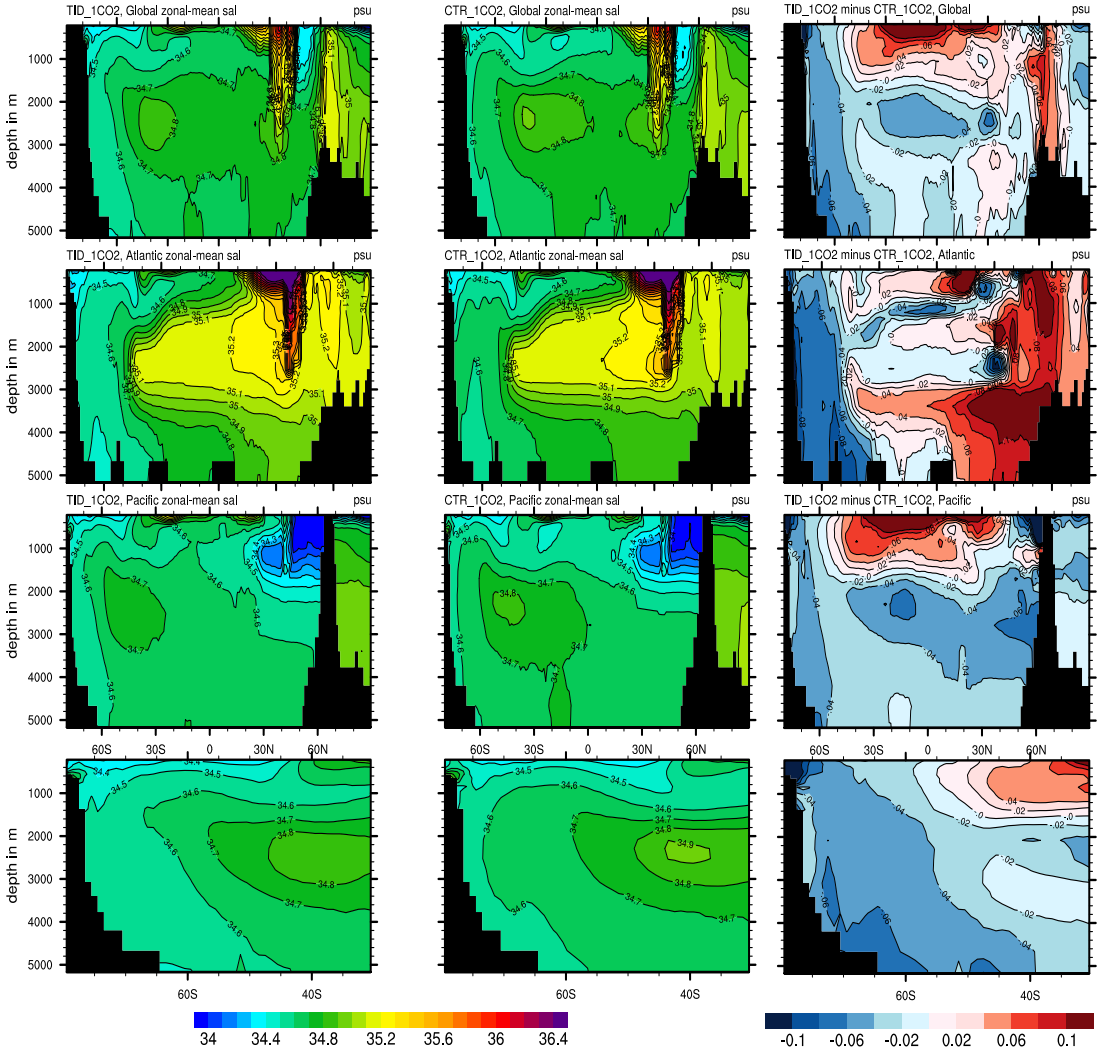

Figure 3.9: Zonal-mean ocean salinity (in psu), for (from top to bottom row): World Ocean, Atlantic, Pacific, and Southern Ocean. Left is $\mathrm{TID}_{1\mathrm{CO2}}$, middle is $\mathrm{CTR}_{1\mathrm{CO2}}$, and right is their difference: $\mathrm{TID}_{1\mathrm{CO2}}$ minus $\mathrm{CTR}_{1\mathrm{CO2}}$.

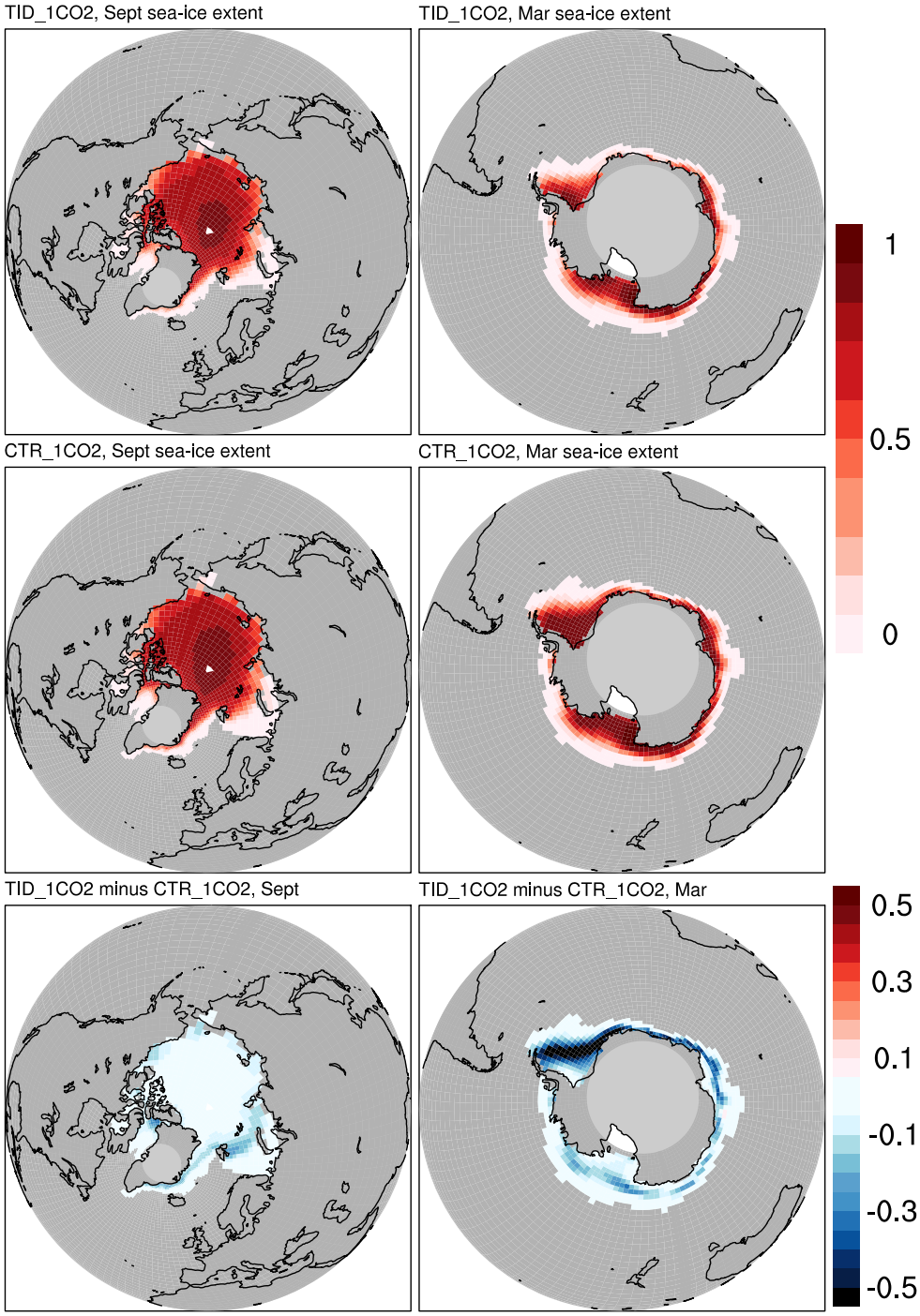

Figure 3.10: Summer sea-ice area (in grid cell fraction) defined as September for NH (shown in left column) and as March for SH (shown in right column) in $\mathrm{TID}_{1\mathrm{CO2}}$ (top), $\mathrm{CTR}_{1\mathrm{CO2}}$ (middle), and the difference $\mathrm{TID}_{1\mathrm{CO2}}$-$\mathrm{CTR}_{1\mathrm{CO2}}$ (bottom).

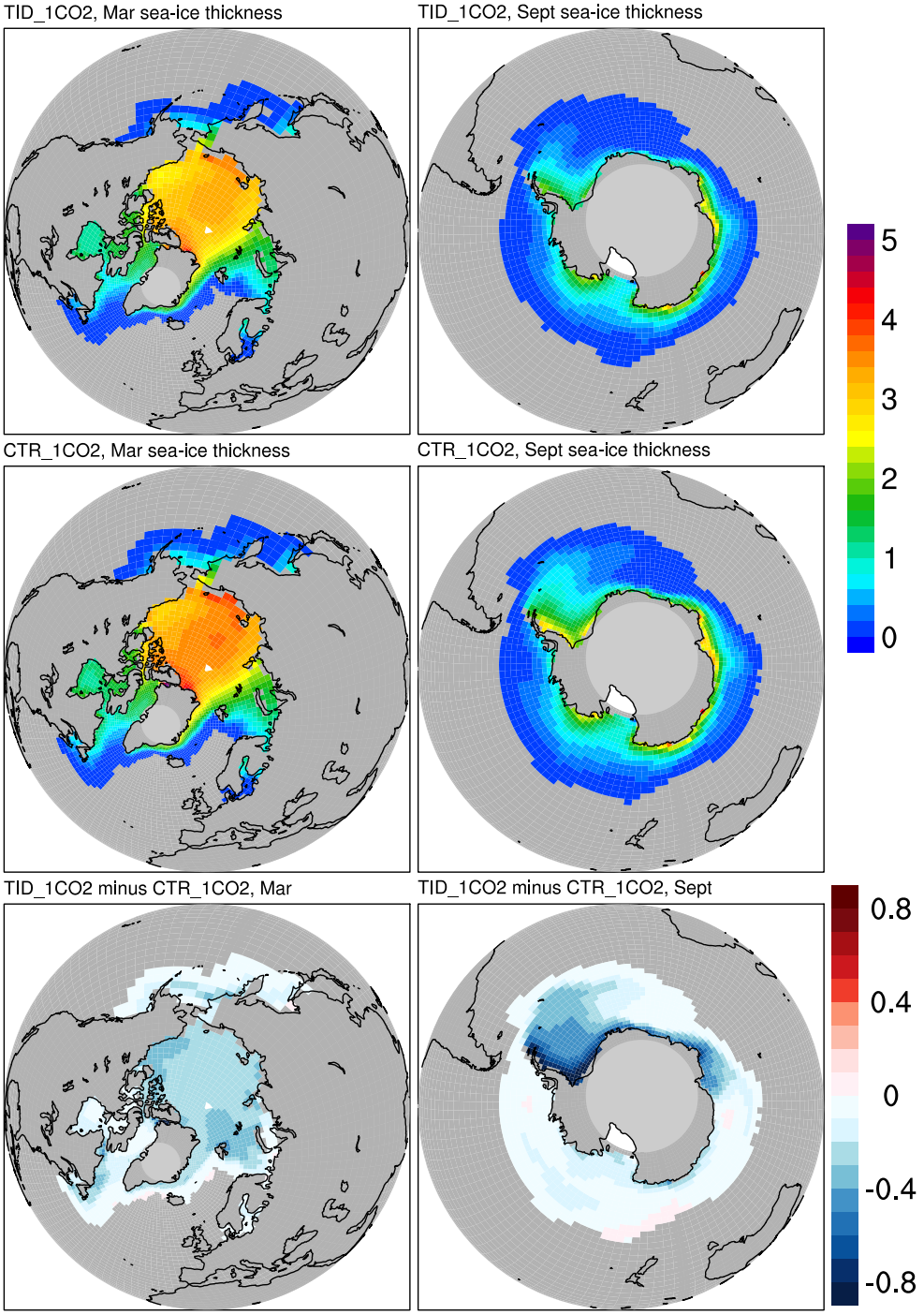

Figure 3.11: Winter sea-ice thickness (in m) defined as March for NH (shown in left column) and as September for SH (shown in right column) in TID_{1CO2} (top), CTR_{1CO2} (middle), and the difference TID_{1CO2}-CTR_{1CO2} (bottom).

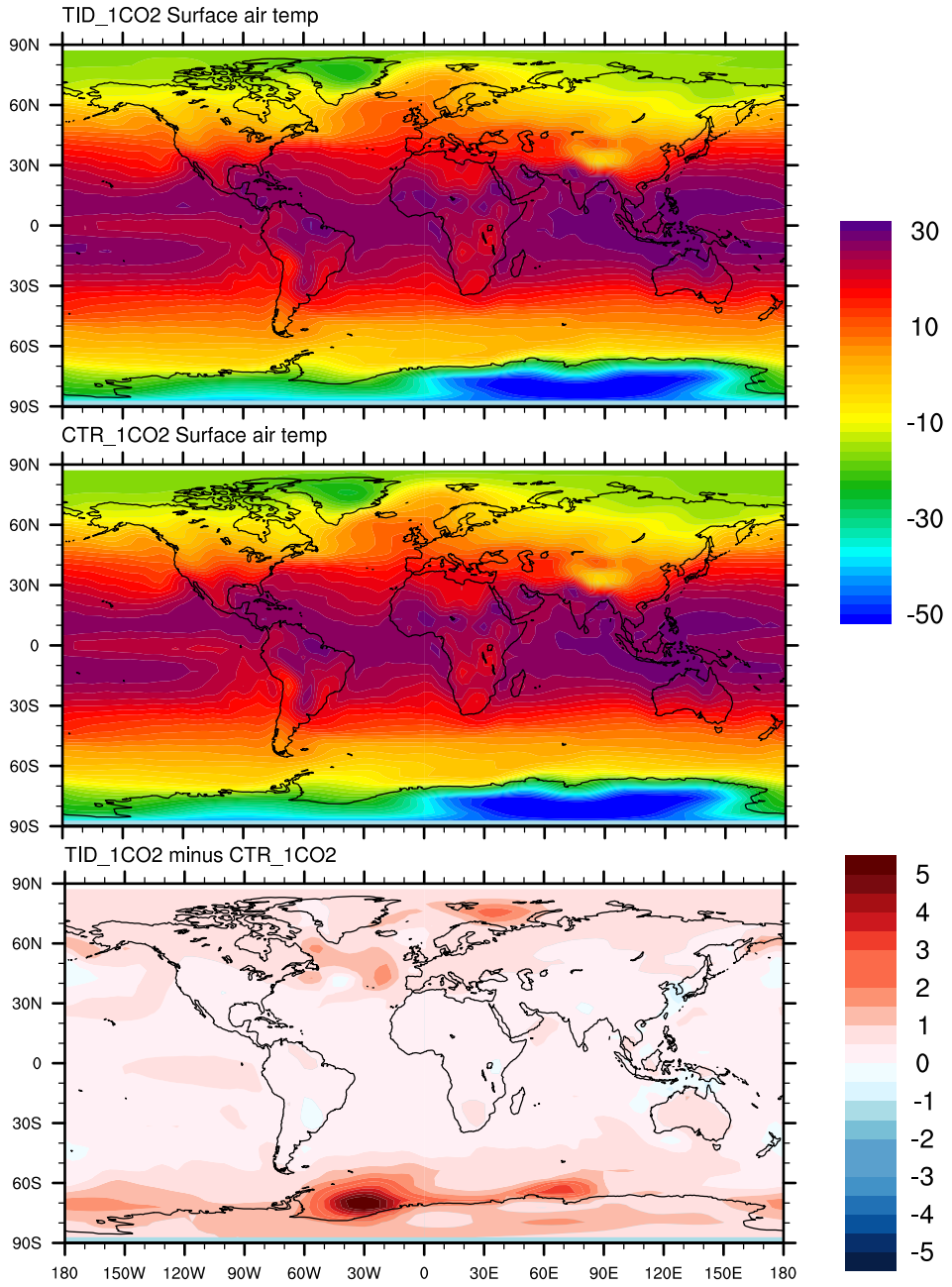

Figure 3.12: Surface air temperature (in °C, defined as the temperature at 2 m above the sea surface) for $\mathrm{TID_{1CO2}}$ (top), $\mathrm{CTR_{1CO2}}$ (middle), and the difference $\mathrm{TID_{1CO2}}$-$\mathrm{CTR_{1CO2}}$ (bottom).

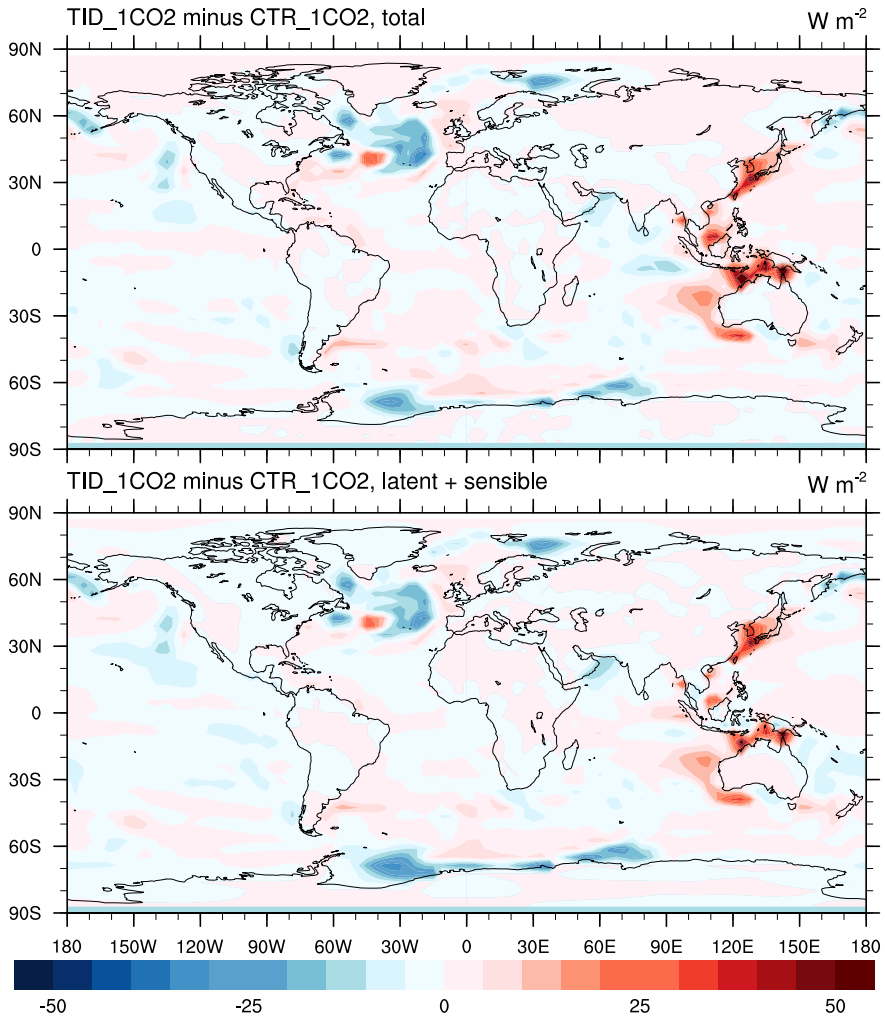

Figure 3.13: Net surface heat fluxes (positive heat fluxes are downward) for the difference $\mathrm{TID}_{1\mathrm{CO2}}$ minus $\mathrm{CTR}_{1\mathrm{CO2}}$ (in $\mathrm{W/m^2}$), for total (top) and latent plus sensible (bottom) heat fluxes. Negative difference means that $\mathrm{TID}_{1\mathrm{CO2}}$ has larger surface fluxes to the atmosphere (or smaller fluxes to the ocean).

3.4 Tidal-mixing induced changes in climate response

We discuss how much the climate response to CO_2 doubling, described by changes in global-mean SAT and sea ice conditions, is modified when tidal mixing is implemented. We discuss changes in the ocean, like the meridional mass and heat transports, as well as the ocean temperature and heat content changes. We also discuss what are the physical mechanisms responsible for the changes in the response. Our approach is, as we already described in Section 3.2, to increase CO_2 by 1% year^{-1} until CO_2 doubling (year 70), and then we keep CO_2 constant for another 430 years. Here we define 'response' as the difference $\text{RES}_{\text{`EXP'}} = \text{`EXP'}_{2\text{CO2}} - \text{`EXP'}_{1\text{CO2}}$, where $\text{`EXP'}_{2\text{CO2}}$ is the time-mean of the last 100 years of the post-transient climate and $\text{`EXP'}_{1\text{CO2}}$ is the time-mean of the last 200 years of the spin-up integrations ('EXP' is either CTR or TID, see also Fig. 3.2). In order to isolate the impact of tidal mixing on the post-transient climate, we also discuss the differences $\text{RES}_{\text{TID}} - \text{RES}_{\text{CTR}}$. All differences are ensemble means of three runs for each experimental set-up, each run starting from slightly different initial conditions, in order to eliminate the natural variability of the climatic states that are far from quasi-equilibrium.

3.4.1 Meridional mass transports

We discuss the response in the mass transports, expressed in the form of the zonally integrated stream function, in the Atlantic, the Info-Pacific and the World Ocean. Positive stream function values imply clockwise and negative counter-clockwise transports. During the transient phase, the overturning circulation decreases rapidly and continues decreasing for a long time during the post-transient phase (not shown). The overturning circulation starts to recover at about year 140 after initialization of CO_2 doubling, but full recovery does not take place until the end of the 500-year long simulation. The response is calculated at the last stage of the post-transient climate, so the circulation is still weaker than in the quasi-equilibrium climate.

Atlantic

The CTR response in the Atlantic circulation is shown in Fig. 3.14. There is an overall decrease in transports in both upper and lower cells (the stream function is positive in the upper and negative in the lower cell in quasi-equilibrium). The response is 4.57 Sv in the upper and 2.25 Sv in the lower cell. Even though the reduction in the lower cell transport seems to be very drastic, the bottom ocean does not become stagnant; the bottom circulation becomes very weak, but there is still some transport (~ 1 Sv).

The weakening of the Atlantic circulation as a response to CO_2 increase is a well known effect and has been reproduced in many modeling studies (e.g. Manabe et al., 1991; Manabe and Stouffer, 1993; Rahmstorf and Ganopolski, 1999), also in the IPCC

framework studies (Fig. 3.1). The weakening of the circulation is caused by weakening of the meridional density gradient due to a reduction in deep water formation. The deep water formation is inhibited because of a weakening of convection, caused by the increase in buoyancy of surface waters in high latitudes, at deep water formation regions, because of increased surface freshwater and heat fluxes to the ocean (Dixon et al., 1999; Mikolajewitcz and Voss, 2000).

In the response of the circulation (Fig. 3.14) even though there is a reduction everywhere, there is one region where there is an enhancement in the circulation of up to 1 Sv: the northern high latitudes (north of 60°). This is a quite common feature among models (Wiebe and Weaver, 1999; Holland and Bitz, 2003; Hu et al., 2004; Bitz et al., 2006). It has been attributed to an intrusion of increased salty North Atlantic water into the Nordic Seas and Arctic Ocean, that makes denser the upper water column, which then leads to increasing convective activity in the region. Therefore, the weakening in convection that slows down the overall Atlantic circulation takes place south of 60° N, whereas poleward of 60° N, the convection, hence the circulation, increase.

The differences in the response due to tidal mixing is shown at the bottom panel of Fig. 3.14. The magnitude of the response in the upper cell increases by 1.2 Sv and in the lower cell by 0.9 Sv. Hence, tidal mixing causes a stronger reduction in the Atlantic circulation in both cells, upper and lower. At the northern high latitudes, TID has a stronger response at the latitudes of the Nordic Seas, and weaker response in the Arctic Ocean. The TID circulation, therefore, increases more than CTR in the Nordic Seas, but increases less than CTR in the Arctic Ocean.

Info-Pacific

The response in the CTR Info-Pacific circulation is mostly positive (Fig. 3.15). In quasi-equilibrium, the Info-pacific stream function is negative in deep and bottom ocean, implying a counter-clockwise transport. Positive response means that Info-pacific stream function is reduced, or even reverses its sign from negative to positive, hence becoming clockwise. What is happening in fact is a combination of both, so the stream function both reduces and changes sign at some depths.

$\mathrm{RES_{TID}}$ is stronger by up to 3 Sv than $\mathrm{RES_{CTR}}$ (bottom panel of Fig. 3.15) below 1500 m, but it is weaker above 1500 m and at the SH. Tidal mixing, therefore, as is also the case in the Atlantic Ocean, causes a stronger reduction in the deep and bottom indo-pacific circulation.

Global

The CTR response in the World Ocean is shown in Fig. 3.16. The signs of the stream function at $1\times CO_2$ (Fig. 3.5) imply that, at $1\times CO_2$, there are two main cells separated at around 3000 m depth, representing water of Atlantic origin circulating clockwise at

the upper cell, and of Antarctic origin circulating counter-clockwise at the lower cell. At $2\times CO_2$, both cells generally are weakened.

The reduction in the overturning in the World Ocean, as it is also the case in Atlantic and Info-Pacific, is stronger in TID. The difference in the responses due to tidal mixing is 1.2 Sv in the upper cell (response of TID is 32% larger than CTR) and 4.5 Sv in the lower cell (response of TID is 53% larger than CTR, bottom panel of Fig. 3.16).

Despite the overall decrease in the global overturning circulation, there is a one region where the overturning circulation actually increases: between $45^\circ - 70^\circ$ S, at the upper cell. This increase is evident in both experiments, but from the difference plot (bottom panel of Fig. 3.16) we can infer that the increase of the Deacon cell is stronger in TID than in CTR. The increase of the Deacon cell is associated with increase of the zonal wind stress over this region, and in TID the wind stress increase is stronger than in CTR (Fig. 3.17).

Therefore, the overall picture is that the tidal mixing significantly alters the response in the global circulation: it increases the reduction in the meridional transports in both upper and lower cells, and particularly in the deep ocean, where tidal mixing is stronger.

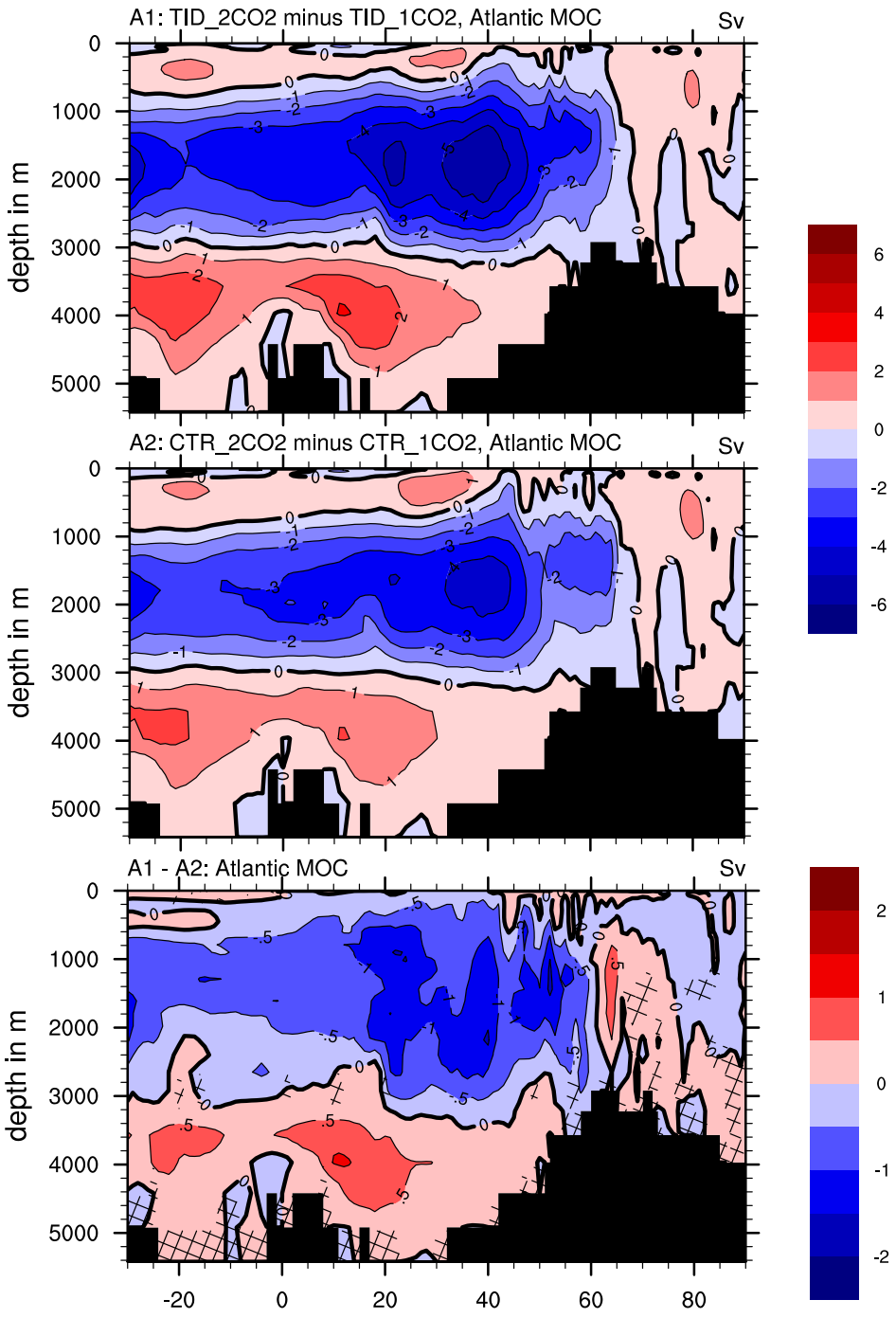

Figure 3.14: Response of meridional overturning stream function in the Atlantic Ocean (in Sv), where response is defined as 'EXP_{2CO2}'−'EXP_{1CO2}', for TID (top), CTR (middle) and the differences between responses of TID and CTR (bottom). (Contour interval for the top and middle plots: 1 Sv. For the bottom plot: 0.5 Sv). A Student's t-test is performed on time series of TID_{RES} and CTR_{RES} during the last 100 years of the post-transient phase, to test the null hypothesis that the means of the responses are equal. Shaded grid points at the bottom plot are points where the null hypothesis is not rejected, at a 95% significance level.

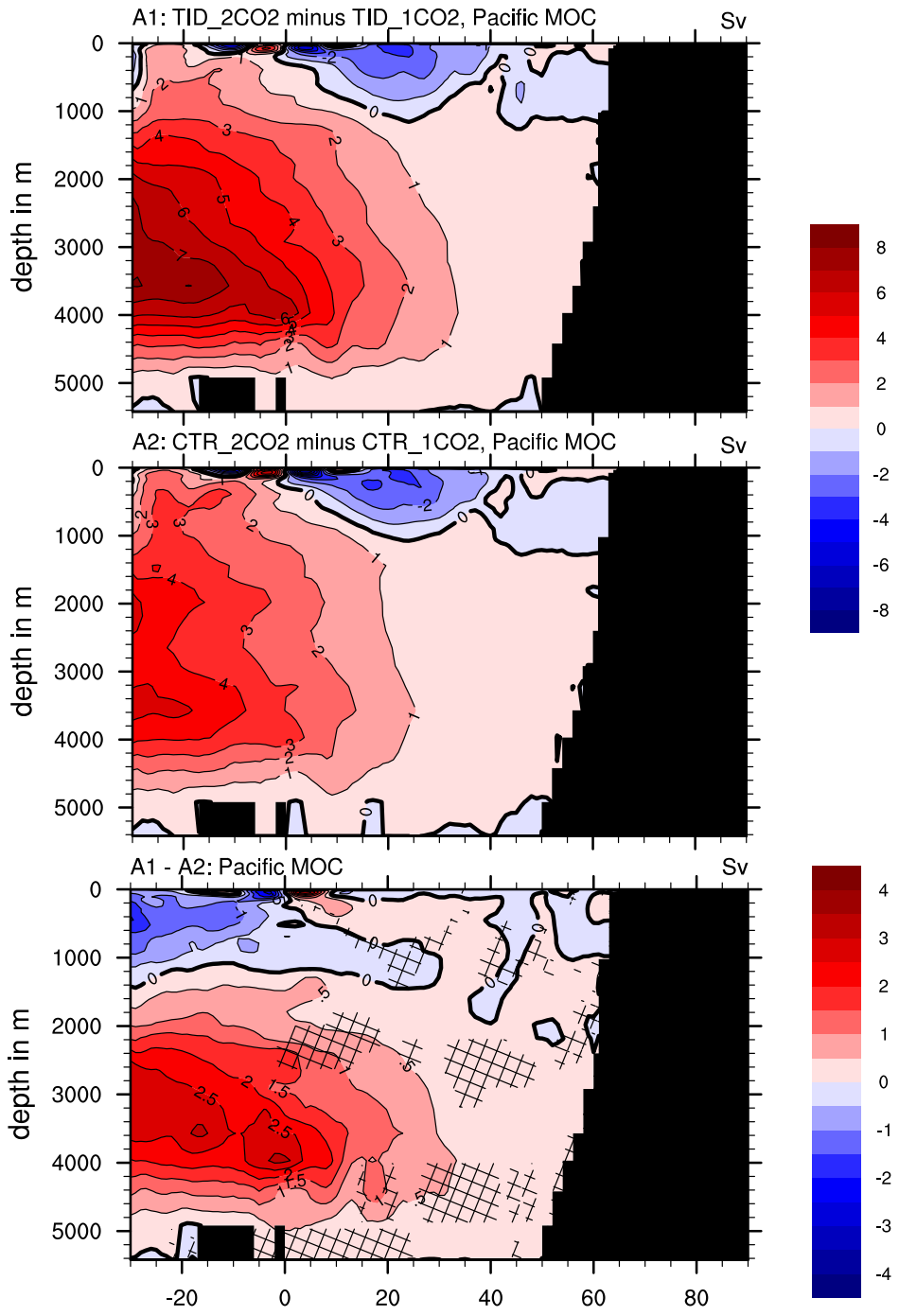

Figure 3.15: Response of meridional overturning stream function in the Indo-Pacific Ocean (in Sv), where response is defined as 'EXP_{2CO2}'−'EXP_{1CO2}', for TID (top), CTR (middle) and the differences between responses of TID and CTR (bottom). (Contour interval for the top and middle plots: 1 Sv. For the bottom plot: 0.5 Sv). A Student's t-test is performed on time series of TID_{RES} and CTR_{RES} during the last 100 years of the post-transient phase, to test the null hypothesis that the means of the responses are equal. Shaded grid points at the bottom plot are points where the null hypothesis is not rejected, at a 95% significance level.

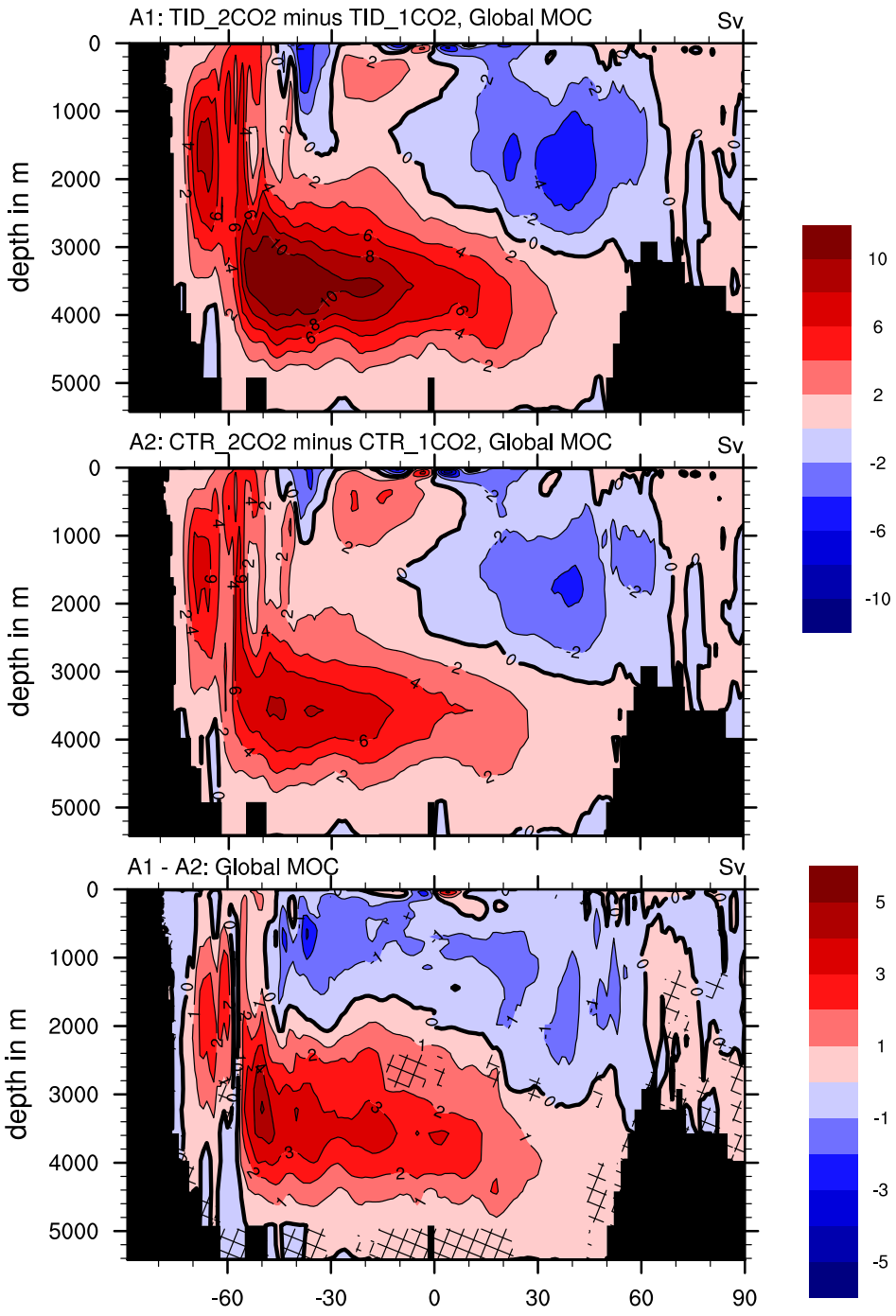

Figure 3.16: Response of meridional overturning stream function in the World Ocean (in Sv), where response is defined as 'EXP_{2CO2}'−'EXP_{1CO2}', for TID (top), CTR (middle) and the differences between responses of TID and CTR (bottom). (Contour interval for the top and middle plots: 2 Sv. For the bottom plot: 1 Sv). A Student's t-test is performed on time series of TID_{RES} and CTR_{RES} during the last 100 years of the post-transient phase, to test the null hypothesis that the means of the responses are equal. Shaded grid points at the bottom plot are points where the null hypothesis is not rejected, at a 95% significance level.

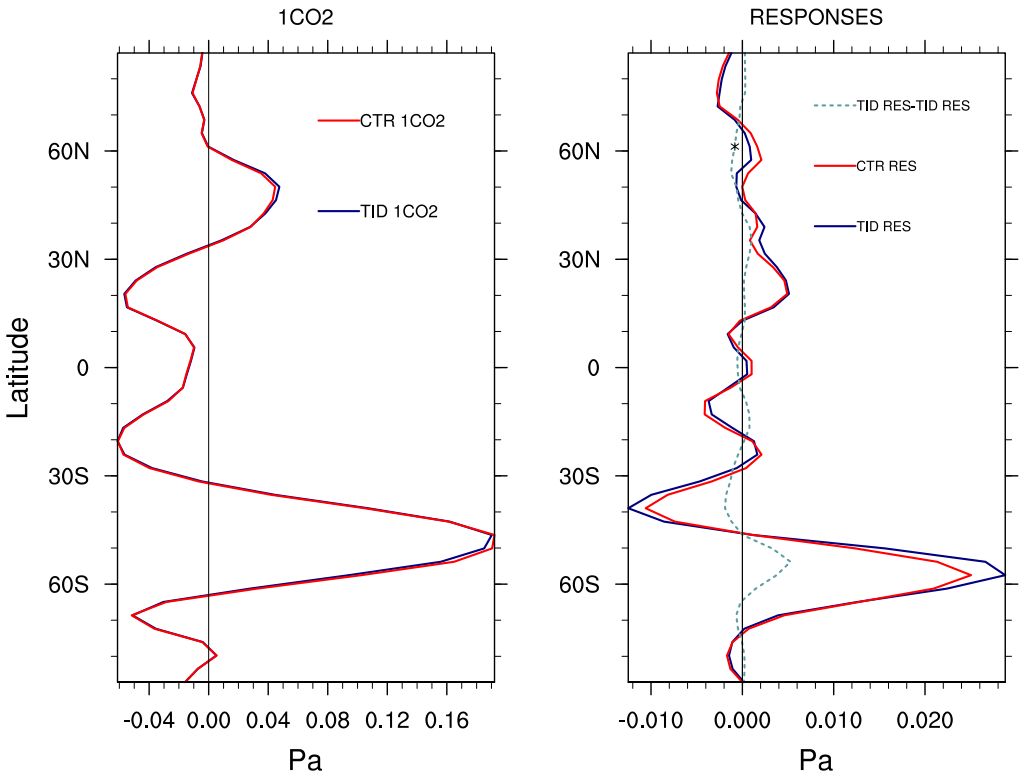

Figure 3.17: Zonal wind stress (in Pa), zonally averaged over the global ocean, for $1\times CO_2$ (left) and for the responses and differences between the responses (right). A Student's t-test is performed on the time series of RES_{TID} and RES_{CTR}, to test whether the difference RES_{TID}-RES_{CTR} is significant. In all but one (starred) point the difference is significant, at a 95% significance level.

3.4.2 Meridional heat transports

Fig. 3.18 shows the response in the meridional heat transports. In general, the heat transports decrease in the $2\times CO_2$ climate in both experiments, as a result of the decreasing ocean mass transports, with few exceptions which we discuss below.

We performed a Student's t-test to examine whether the CTR response in heat transports is significantly different than the TID response. The null hypothesis, that means of the responses are equal, is rejected at a 95% significance level.

Negative (positive) response in the NH global ocean heat transports implies decrease (increase) in the northward heat transports. In the SH it means the opposite. Therefore, the CTR heat transports decrease everywhere, except for the tropics (15° S-10° N) and the northern high latitudes (poleward of 60° N). The latter feature is direct consequence of the increase in the circulation at these latitudes, as already discussed in Section 3.4.1. There is a strong hemispheric asymmetry in CTR response: the maximum NH response is 0.07 PW and maximum SH response is 0.18 PW (0.11 PW difference, and the SH maximum response is 150% larger than the NH one). Therefore, we discuss

hereon separately the responses in heat transports for NH and SH, and also identify what changes occur in the different ocean basin.

The NH global heat transport in CTR reduces at sub-tropical and mid-latitudes, reaching a maximum reduction of 0.07 PW at 30° N. This reduction is mainly due to changes in Atlantic transports (0.05 PW), rather than in Pacific (0.02 PW). The global heat transport increases at tropical and high-latitudes, by 0.05 PW and 0.025 PW, respectively. The increase in the tropical heat transports is entirely due to changes in Pacific, probably being related to wind stress increase in the tropical Pacific (Fig. 3.19). Even though the changes in wind stress seam to be small, they appear to be significant, as shown with a Student's t-test. The tropical Atlantic heat transports are decreasing, hence they are opposite to those in tropical Pacific. The increase in high-latitude global transports, that reach up to 0.25 PW at 65° N, is due to a North Atlantic increase in circulation, as we discussed above.

In the SH of CTR, the heat transport increases by 0.08 PW northward of 15° S, whereas it decreases by up to 0.18 PW poleward of this latitude. Responsible for the SH response are mainly changes in the Pacific Ocean. In the SH tropical Pacific there is, as also in the northern tropical Pacific, an increase in the heat transports, probably related to wind stress changes (Fig. 3.19). The decrease in the pacific heat transports poleward of 15° S is significantly larger (by about 150%) than the decrease in the Atlantic transports, hence creating the large hemispheric asymmetry.

Tidal mixing has opposite effect in the responses in NH and SH: the reduction in heat transports in TID is mostly stronger in the NH compared to CTR, but weaker in the SH. The hemispheric asymmetry, therefore, is largely reduced in TID: difference between NH and SH maximum responses in TID is 0.05 PW (the SH maximum response is 50% larger than the NH one).

In the NH Pacific Ocean, TID response is identical to the one of CTR. This is probably because the NH Pacific is almost stagnant below 1000 m depth at the $1\times CO_2$ climate, and does not really change at the $2\times CO_2$ climate (Fig. 3.15). In the NH Atlantic Ocean, TID has a larger reduction in the heat transport: 0.1 PW, which is 0.03 PW larger than the CTR reduction. A larger reduction in Atlantic heat transport is clearly due to a larger Atlantic MOC reduction in TID (Fig. 3.14).

Concerning the SH reduction in heat transports poleward than 15° S, TID has a mixed impact: the decrease in TID between $15° - 50°$ S is weaker, and between $50° - 70°$ S stronger than in CTR. The latter difference is related to the larger strengthening of the TID Deacon cell of the global stream function in the $2\times CO_2$ climate, that we mentioned in the Section 3.4.1 (Fig. 3.16). The Deacon cell is associated with northward (positive) heat transport, therefore, its larger strengthening in TID implies even stronger northward (positive) heat transport, thus reducing more the amplitude of the southward (negative) heat transport. In the latitude band $15° - 50°$ S, both Atlantic and Pacific basins are contributing to the reduced TID response in the heat transports.

In Atlantic, the heat transport at the SH between $10^\circ - 30^\circ$ S is even increasing in the CTR.

The overall effect of tidal mixing on the heat transports is that it leads to a stronger reduction in heat transports in the NH (about 42% more than in CTR) and between $50^\circ - 70^\circ$ S ($\sim$ 50% more than in CTR), but to a weaker reduction in heat transports in the SH between $15^\circ - 50^\circ$ S ($\sim$ 16% less than in CTR). The stronger reduction in the subpolar SH latitudes in TID results from stronger increase of zonal wind stress over these latitudes in the experiment with tidal mixing.

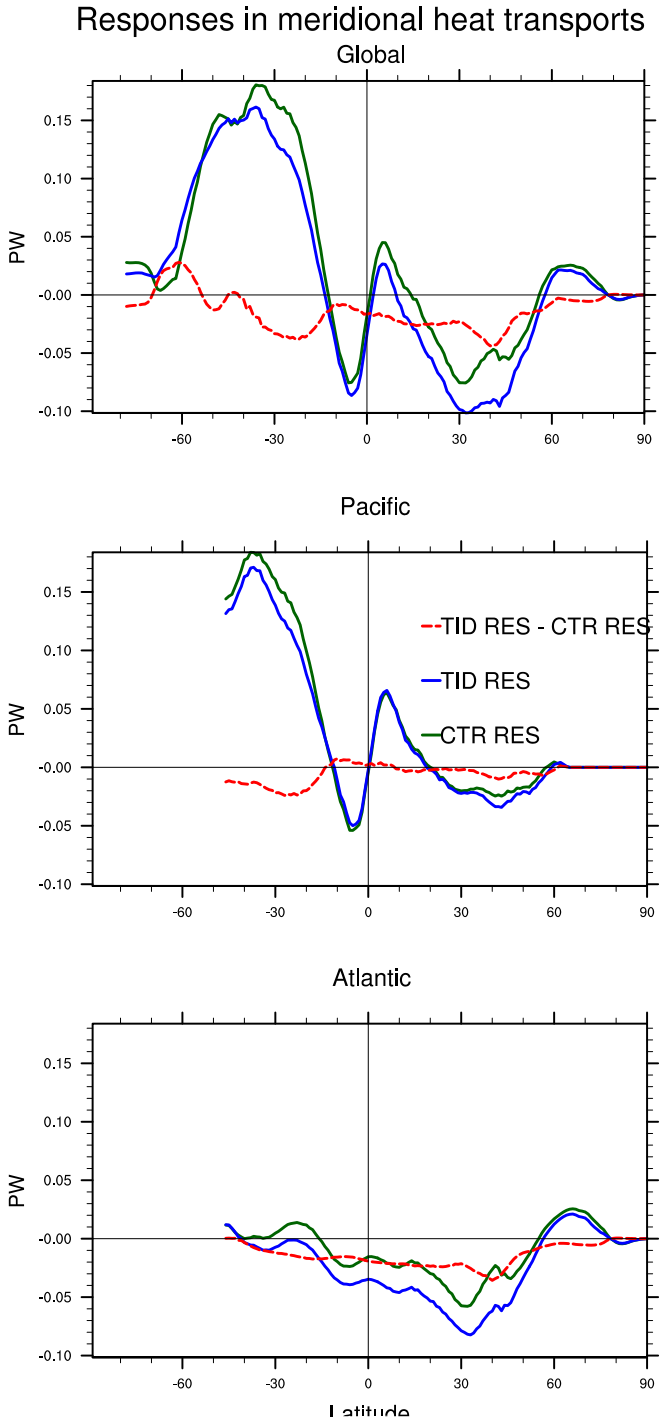

Figure 3.18: Responses in meridional heat transport (in PW) and differences of the responses, for the Global (top), Pacific (middle) and Atlantic (bottom) Ocean.

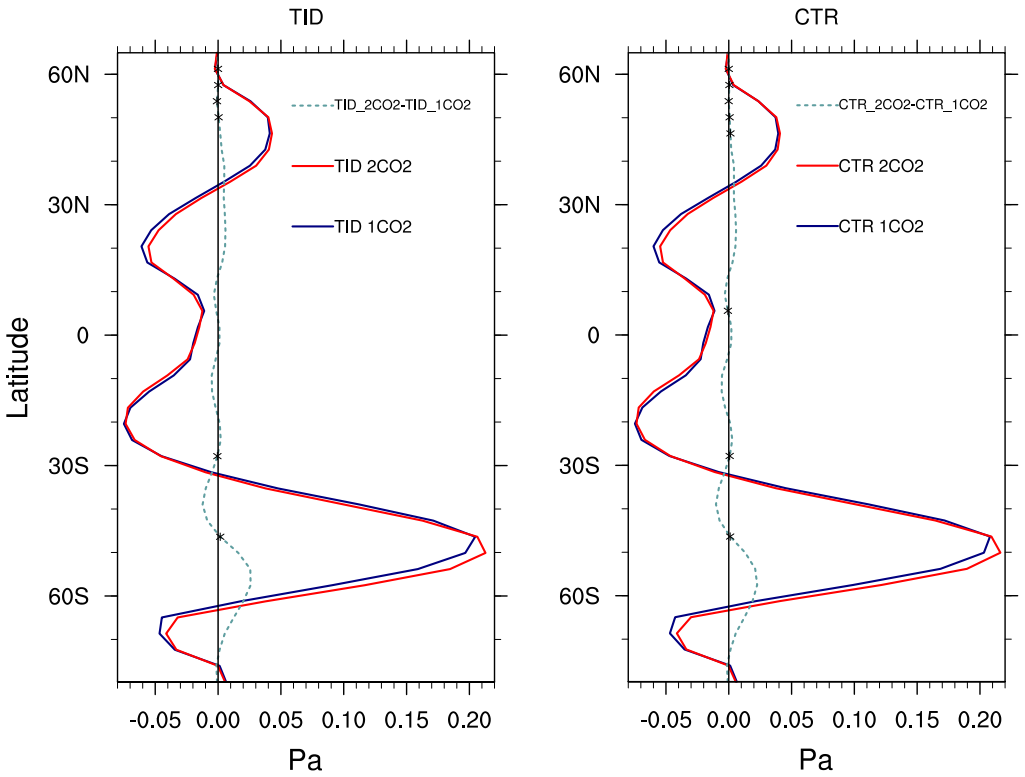

Figure 3.19: Zonal wind stress (in Pa), zonally averaged over Pacific, for TID (left) and CTR (right). A Student's t-test is performed on the time series of EXP_{1CO2} and EXP_{2CO2} (EXP is TID or CTR), to test whether the difference EXP_{2CO2}-EXP_{1CO2} is significant. Starred points in the lines EXP_{2CO2}-EXP_{1CO2} are points where the difference is not significant, at a 95% significance level.

3.4.3 Sea ice

We discuss the changes in the sea ice as a result of CO_2 forcing. As in the previous section with the description of sea ice at $1\times CO_2$, we describe summer sea-ice extent and winter sea-ice thickness.

Fig. 3.20 shows the response in summer sea-ice area in both hemispheres and the differences between the responses. The NH summer sea ice (NH summer is September here), disappears completely in CTR. This is not the case for SH summer sea ice (SH summer is March here), where there is still some sea ice at the Weddell and Ross Seas. Fig. 3.21 shows the response in late-winter sea-ice thickness (we define late-winter as March in NH and September in SH). As in most modeling studies in IPCC framework, CTR experiences a larger late-winter sea ice melt in the NH than in the SH. In the NH sea-ice thickness decreases by more than 2 m, in the SH the decrease is only $0.5-1$ m. The strong asymmetric response between NH and SH is attributed to the largest reduction of heat loss from ocean to the atmosphere (equivalent to net heat uptake) in the Southern Ocean, due to reduced vertical mixing in the ocean (Gregory,

2000).

Tidal mixing leads to both weaker summer sea-ice area loss, and less late-winter sea-ice melting. TID, like CTR, becomes sea-ice free in the summer. If changes in the sea-ice responses are $\mathrm{DIFF_{RES}} = \mathrm{TID_{2CO2}} - \mathrm{TID_{1CO2}} - (\mathrm{CTR_{2CO2}} - \mathrm{CTR_{1CO2}})$, these are equal to $\mathrm{DIFF_{RES}} = \mathrm{TID_{2CO2}} - \mathrm{CTR_{2CO2}} - (\mathrm{TID_{1CO2}} - \mathrm{CTR_{1CO2}})$. When $\mathrm{TID_{2CO2}}$ and $\mathrm{CTR_{2CO2}}$ become sea-ice free, then $\mathrm{TID_{2CO2}} - \mathrm{CTR_{2CO2}} = 0$, hence $\mathrm{DIFF_{RES}} = \mathrm{TID_{1CO2}} - \mathrm{CTR_{1CO2}}$, or that the difference between the two responses (bottom panel of Fig. 3.20) are identical to the differences between their equilibrium NH summer sea-ice area (Fig. 3.10). Which means that all the additional summer sea ice that $\mathrm{CTR_{1CO2}}$ has compared to $\mathrm{TID_{1CO2}}$ is lost at the warming climate. Similar conclusion can be derived also for the late-winter sea ice: the differences in the responses in thickness (bottom panel of Fig. 3.21) are very similar to the differences in equilibrium late-winter sea ice (bottom panel of Fig. 3.11). Therefore, CTR loses all the extra late-winter sea ice it has in equilibrium compared to TID experiment, and at the end of the post-transient phase, CTR and TID sea-ice conditions are almost identical. The reasons for the weaker sea-ice loss in TID are related to its different near-surface temperature responses, as we will see in the coming section.

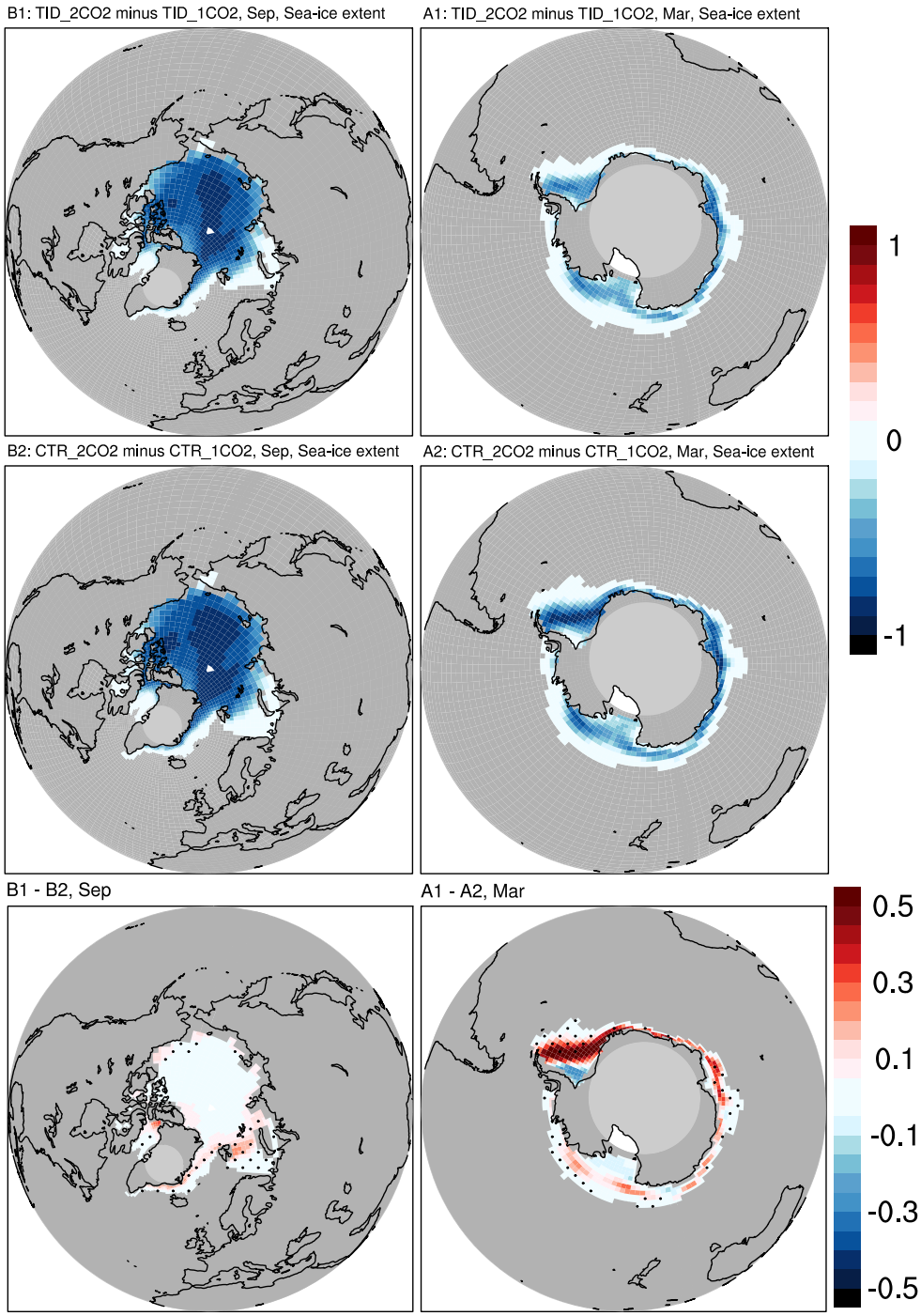

Figure 3.20: Responses in summer sea ice area (in grid cell fraction) defined as September for NH (shown in left column) and as March for SH (shown in right column) for $\mathrm{RES_{TID}}$ (top), $\mathrm{RES_{CTR}}$ (middle), and their difference (bottom). Positive difference at the bottom panel means that $\mathrm{TID_{2CO2}}$ has less sea ice area loss than $\mathrm{CTR_{2CO2}}$. A Student's t-test is performed on time series of $\mathrm{TID_{RES}}$ and $\mathrm{CTR_{RES}}$ during the last 100 years of the post-transient phase, to test the null hypothesis that the means of the responses are equal. The dotted grid points at the bottom plot are points where the null hypothesis is not rejected, at a 95% significance level.

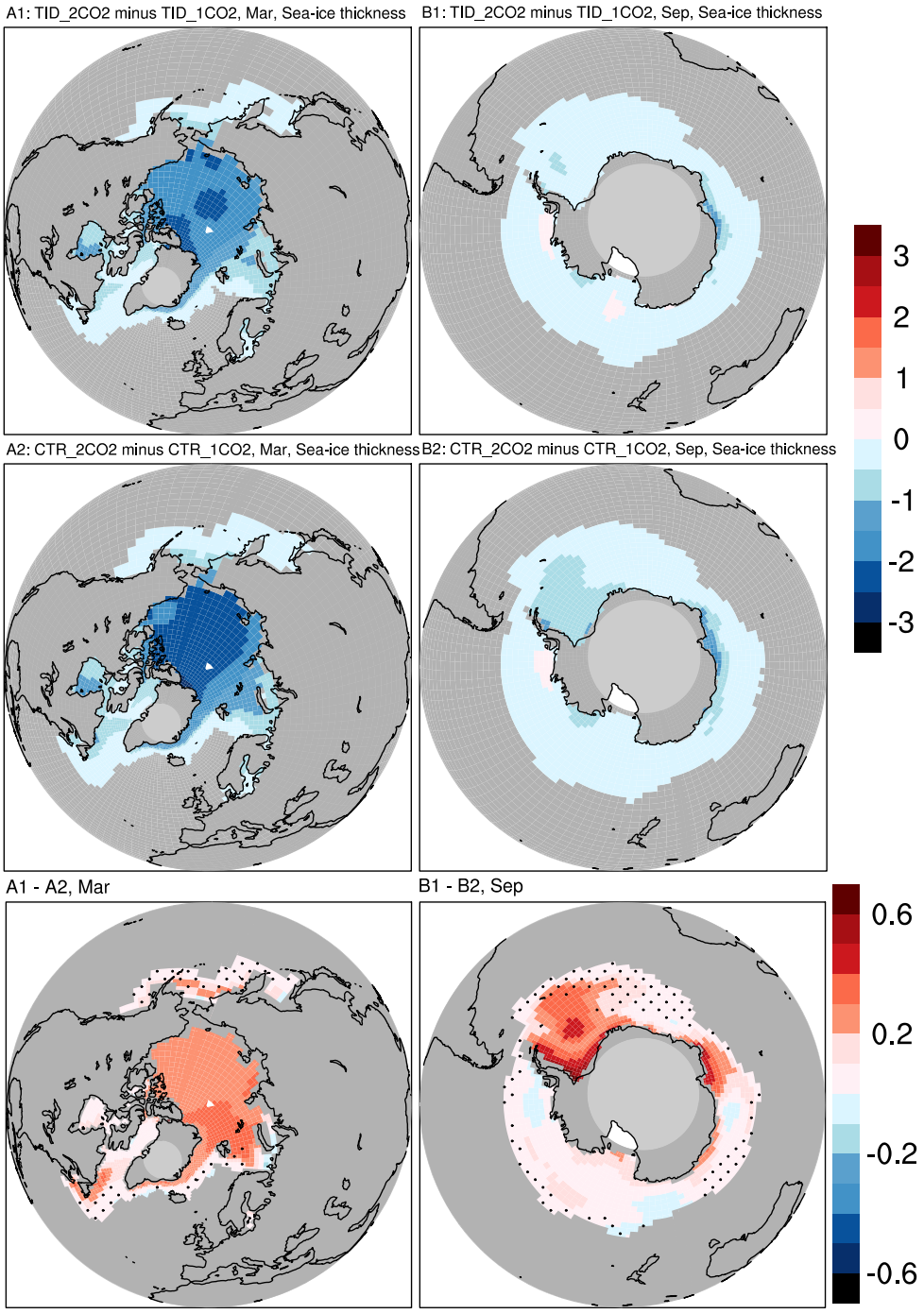

Figure 3.21: Responses in winter sea ice thickness (in m) defined as March for NH (shown in left column) and as September for SH (shown in right column) for $\mathrm{RES_{TID}}$ (top), $\mathrm{RES_{CTR}}$ (middle), and their difference (bottom). Positive difference at the bottom panel means that $\mathrm{TID_{2CO2}}$ has smaller sea ice thickness reduction than $\mathrm{CTR_{2CO2}}$. A Student's t-test is performed on time series of $\mathrm{TID_{RES}}$ and $\mathrm{CTR_{RES}}$ during the last 100 years of the post-transient phase, to test the null hypothesis that the means of the responses are equal. The dotted grid points at the bottom plot are points where the null hypothesis is not rejected, at a 95% significance level.

3.4.4 Near-surface air temperature

Here, we discuss the surface air temperature (SAT, 2 m air temperature) response to $2\times CO_2$ forcing.

The global-mean SAT response in CTR is 3.91 °C. The spatial patterns of the warming are shown in Fig. 3.22. CTR warms more in the polar regions than the middle and low latitudes, a feature commonly referred to as 'polar amplification'. This effect is due to a positive feedback between warming and retreat of sea ice, that lowers the albedo, which amplifies the initial warming, hence the name 'polar amplification'. It is very common among models and it is being reproduced in almost all climate model simulations (Holland and Bitz, 2003).

In TID the SAT response is everywhere smaller, its global-mean being 3.56 °C, which is 8.9% smaller than CTR. The difference plot (bottom panel of Fig. 3.22) reveals the changes between the responses. The differences in responses is similar to the changes between CTR_{1CO2} and TID_{1CO2} in quasi-equilibrium (Fig. 3.12), in both magnitudes and spatial patterns. Therefore, if the differences in the quasi-equilibrium climates are A=$TID_{1CO2}-CTR_{1CO2}$, and the differences in the post-transient climate are B=$TID_{2CO2}-CTR_{2CO2}$, the spatial patterns of A are absent in B, so they do not cancel out in the response difference B−A.

It is interesting that the polar amplification in $TID_{2CO2}-TID_{1CO2}$ is weaker than in $CTR_{2CO2}-CTR_{1CO2}$. At the SAT responses normalized with the global-mean response (Fig. 3.23), we can see in more detail the differences in polar amplification between TID and CTR: in CTR the maximum normalized SAT for the NH is 3.06, and for the SH is 2.31. These numbers mean that in CTR the (maximum) NH polar warming is 3.06 times the CTR global-mean warming, and the (maximum) SH polar warming is 2.31 times the CTR global-mean warming. For TID_{2CO2} the respective numbers are 2.77 K (9% less than in CTR) and 1.93 °C (17% less than in CTR). The polar response in TID, therefore, is clearly weaker. The weaker polar SAT response in TID is associated with its weaker sea-ice loss (Section 3.4.3). According to the polar amplification mechanism, an initial polar warming triggers the sea-ice albedo feedback, which melts the sea ice and hence reduces albedo, which in turn causes even more warming. In TID_{2CO2} the overall temperature response is weaker compared to CTR_{2CO2}, which in turn initiates a weaker sea-ice albedo feedback, that on one hand results in weaker sea ice loss, on the other hand results in weaker polar amplification.

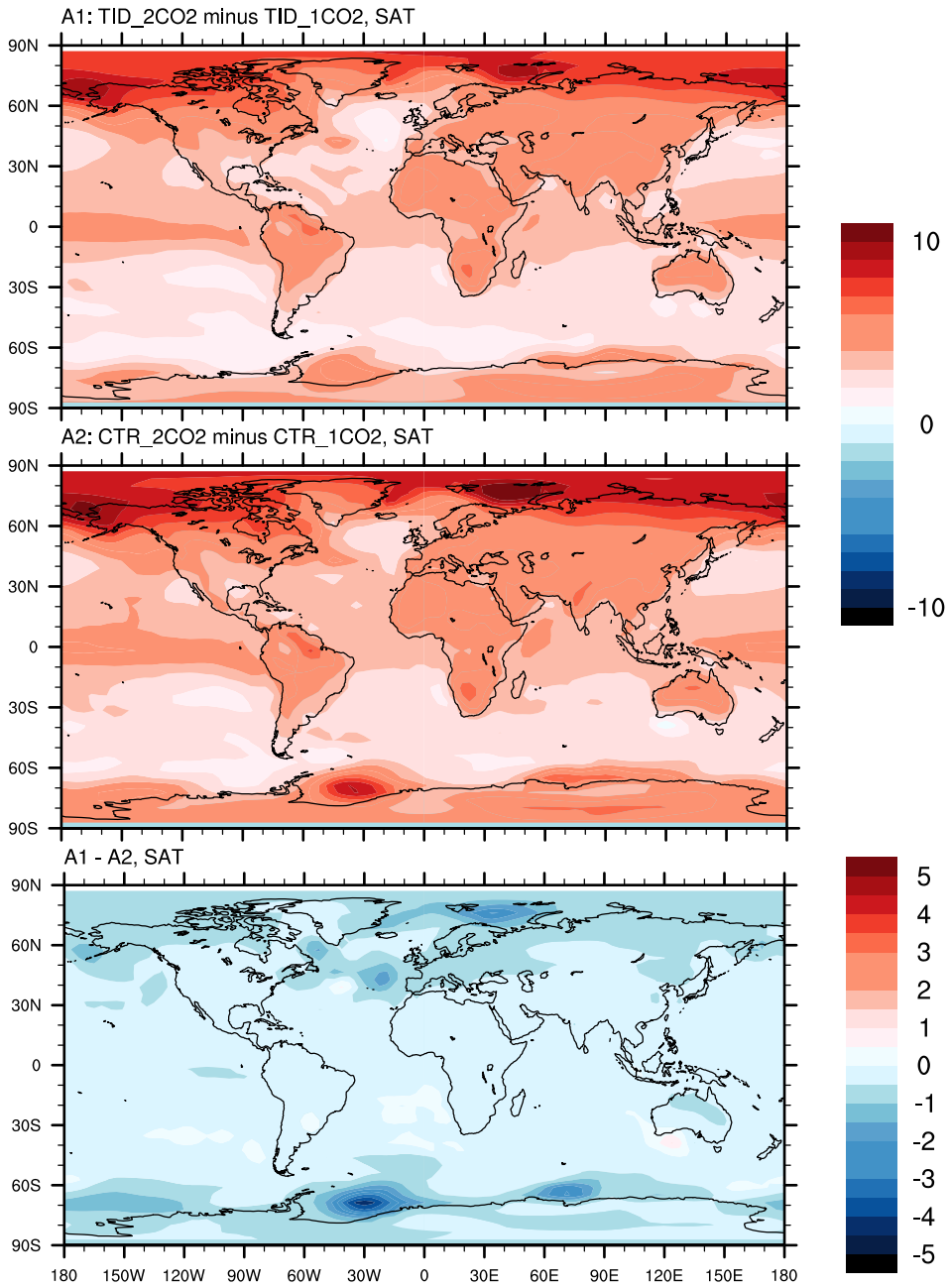

Figure 3.22: Response in surface air temperature (in °C, defined as the temperature at 2 m above the sea surface) for TID_{2CO2} (top), CTR_{2CO2} (middle), and their difference (bottom). The statistical significance of the results is tested with a Student's t-test, with the null hypothesis that the means of the responses in CTR and TID are equal. In almost all points the null hypothesis was rejected at 95% significance level.

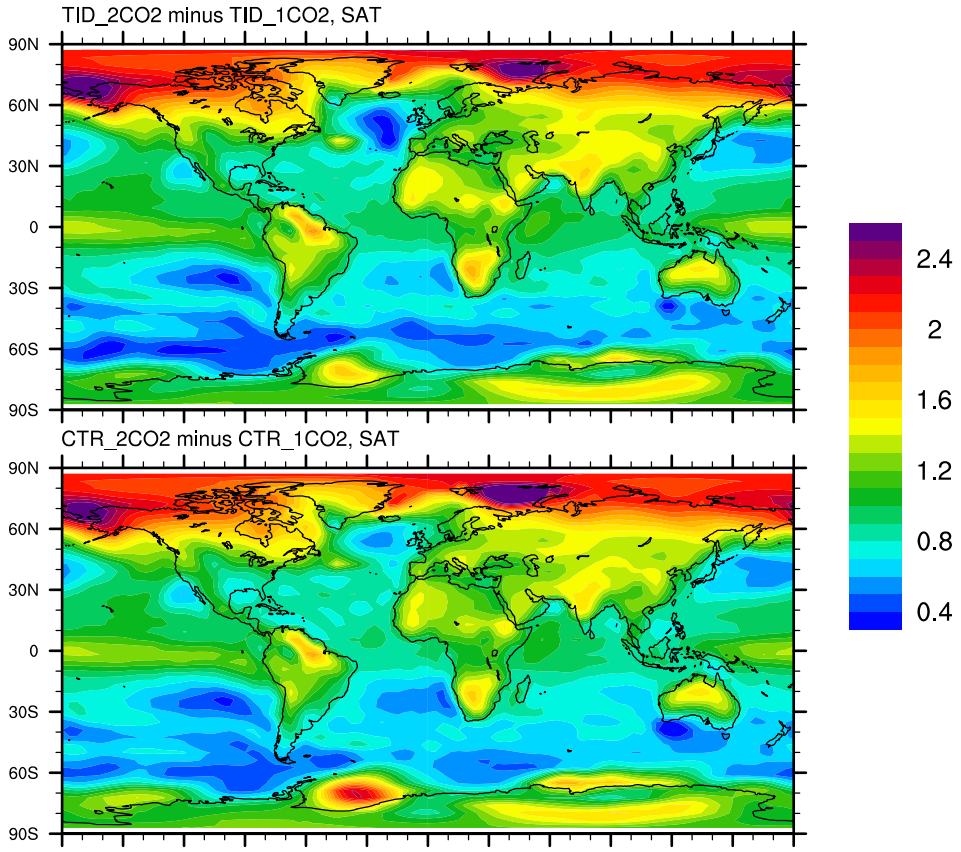

Figure 3.23: Response in surface air temperature, normalized by the global-mean SAT response (unit is ratio) for $\mathrm{TID}_{2\mathrm{CO2}}$ (top) and $\mathrm{CTR}_{2\mathrm{CO2}}$ (bottom).

3.5 Role of ocean heat uptake for the reduction in near-surface warming induced by tidal mixing

We discuss the ocean temperature response to $2\times CO_2$ forcing in order to understand the ocean heat uptake changes. The World Ocean has enormous heat capacity compared to any other earth system component, and by taking up heat during the transient and post-transient phase, the ocean can substantially delay surface climate change (Banks and Gregory, 2006; Manabe et al., 1991; Raper et al., 2002). Bóe et al. (2009) argue that differences in deep ocean heat uptake among coupled models is one of the major uncertainties in transient surface climate change projections. Therefore, modification in deep ocean heat uptake due to tidal mixing, can provide the answer for the weaker TID surface climate response.

3.5.1 Relation between the reduction in near-surface warming and the changes in heat content

Ocean temperature

Fig. 3.24 shows response in the ocean potential temperature and the differences between the responses for the World Ocean. The global oceans of both CTR and TID are getting warmer with time, particularly in the upper 2000 m. Differences between the responses show clearly that TID takes up more heat, hence becoming warmer, in the deep ocean (below 3000 m depth), leaving thus the TID response in the upper 2000 m slightly weaker than in CTR.

We further investigate how the temperature response is distributed among the different ocean basins, namely the Atlantic, Indo-Pacific and Southern Ocean (Fig. 3.25). Two features are striking: first, above 3000 m depth, the Atlantic is the dominant basin in heat uptake. This is in line with observations (Levitus et al., 2000), according to which the upper 700 m of Atlantic warm much faster than the rest of the oceans. The faster warming rate of Atlantic has been attributed to enhanced inter-ocean heat transport from Indian to Atlantic through the Agulhas leakage due to a strengthening of the wind stress curl over the SH Atlantic and Indian Ocean (Lee et al., 2011). This is also the case in our experiments: the zonal wind stress is enhanced in the SH between $50^\circ - 70^\circ$ S, in both TID and CTR, and the increase in TID is stronger than the increase in CTR (Fig. 3.17). The second striking feature is that, below 3000 m depth, the Southern Ocean is the dominant basin in deep ocean warming. According to Gregory (2000), the Southern Ocean is a dominant region for ocean heat uptake because there is a large reduction in heat loss from the ocean to the atmosphere (equivalent to net heat uptake) at the southern high latitudes, due to a reduction in isopycnal diffusion, resulting from reduction in high-latitude convection.

Fig. 3.25 also shows the TID response and the difference between the responses in

ocean temperature (top and bottom panel). The response in TID ocean temperature is in all basins stronger (more warming) in the deep ocean and weaker (less warming) in the upper ocean than that in CTR. The stronger TID deep ocean warming is more pronounced in the Atlantic and Southern Ocean. Therefore, it is quite clear that the deep ocean heat uptake increases with tidal mixing. This increase is responsible for the TID weaker surface temperature response.

Ocean heat content

We can translate the temperature responses ΔT of the above plots into heat content changes ΔQ, according to

$$\Delta Q = \int_{-H}^{z} \iint c\Delta T(x, y, z)\, \mathrm{d}x\, \mathrm{d}y\, \mathrm{d}z, \tag{3.2}$$

where $c = 4.1 \times 10^6\,\mathrm{J\ m^{-3}\,K^{-1}}$ is the volumetric heat capacity, and $\iint \mathrm{d}x\, \mathrm{d}y$ indicates the area integral at a given depth. Equation 3.2 estimates the heat content change integrated between the depth levels z and $-H$ and along longitude x and latitude y. In Fig. 3.26 the heat content changes for the World Ocean are shown. The heat content responses are distributed more evenly with depth compared to the temperature responses, because of the large volume of the deep ocean. As we expected, the deep ocean heat uptake in TID is more dominant than in CTR: in TID, the additional heat is distributed between 1000 and 4500 m, whereas in CTR heat is distributed only up to 3000 m depth. The difference between the two experiments lies mainly below 2000 m depth. The last 50-year time-mean heat content change, integrated from surface to bottom is 7.99×10^{24} J for CTR and 9.05×10^{24} J for TID. The total heat content change in TID is 13% larger than in CTR, and this can explain why TID has smaller surface temperature response in the post-transient phase than CTR. Most of the heat uptake in TID takes place in the deep ocean: it stores about 40% more heat below 2000 m depth than CTR (Table 3.2).

Fig. 3.27 shows the distribution of heat content change among the three major ocean basins. In CTR heat content changes, even though the Atlantic has the largest and the Indo-Pacific the smallest temperature response, the heat content responses are reversed: Indo-Pacific stores most of the heat (about 50% of the total heat), while the other two basins store significantly less ($\sim 25\%$ of the total heat for each basin) (see Table 3.2). This is not surprising, since, according to Equation 3.2, the heat content change is integrated along the dimensions of a basin, and Indo-Pacific is the largest ocean basin of all.

In TID the total heat content change is stronger by $12 - 16\%$ than CTR in all basins. In the deep ocean (below 2 km depth), TID stores $34 - 54\%$ more heat than CTR

(Table 3.2). The largest difference between TID and CTR heat content change is in the Atlantic Ocean.

Even though the heat content change in CTR and TID is largest in the Pacific, due to its dimensions, the Atlantic and Southern Ocean have the largest heat content change per unit area, as the horizontal map of vertical integration in heat content change reveals (Fig. 3.28). This figure also shows that the basins where TID stores more heat per surface unit compared to CTR, are the Atlantic and Southern Ocean. Russell (2006) also found increased heat storage in Atlantic and Southern Ocean in global warming simulations, which was caused by poleward intensification of westerly winds, which in turn resulted in larger outcrop area of dense water around Antarctica. In our experiments, even though there is a larger intensification of the SH westerly winds in TID compared to CTR (Fig. 3.17), we did not find significant differences in the outcropping areas of dense water between TID and CTR. In Section 3.6 we investigate in detail the processes that are responsible for the deep ocean ocean heat uptake.

ΔQ (in 10^{24} J)	GLOBAL	ATLANTIC	INDOPACIFIC	SOUTHERN
TID Total	9.05 (+13%)	2.14 (+16%)	4.37 (+13%)	2.27 (+12%)
CTR Total	7.99	1.83	3.87	2.01
TID (below 2 km)	3.59 (+41%)	0.88 (+54%)	1.60 (+40%)	1.07 (+34%)
CTR (below 2 km)	2.53	0.57	1.14	0.80

Table 3.2: Heat content changes (in 10^{24} J, time-mean of the last 50 years of the post-transient climate), from surface to bottom, and from 2000 m to bottom, using Eq. 3.2, for the World Ocean, and for the Atlantic, Indo-Pacific and Southern Oceans. The numbers in the parenthesis give the percentage difference compared to CTR.

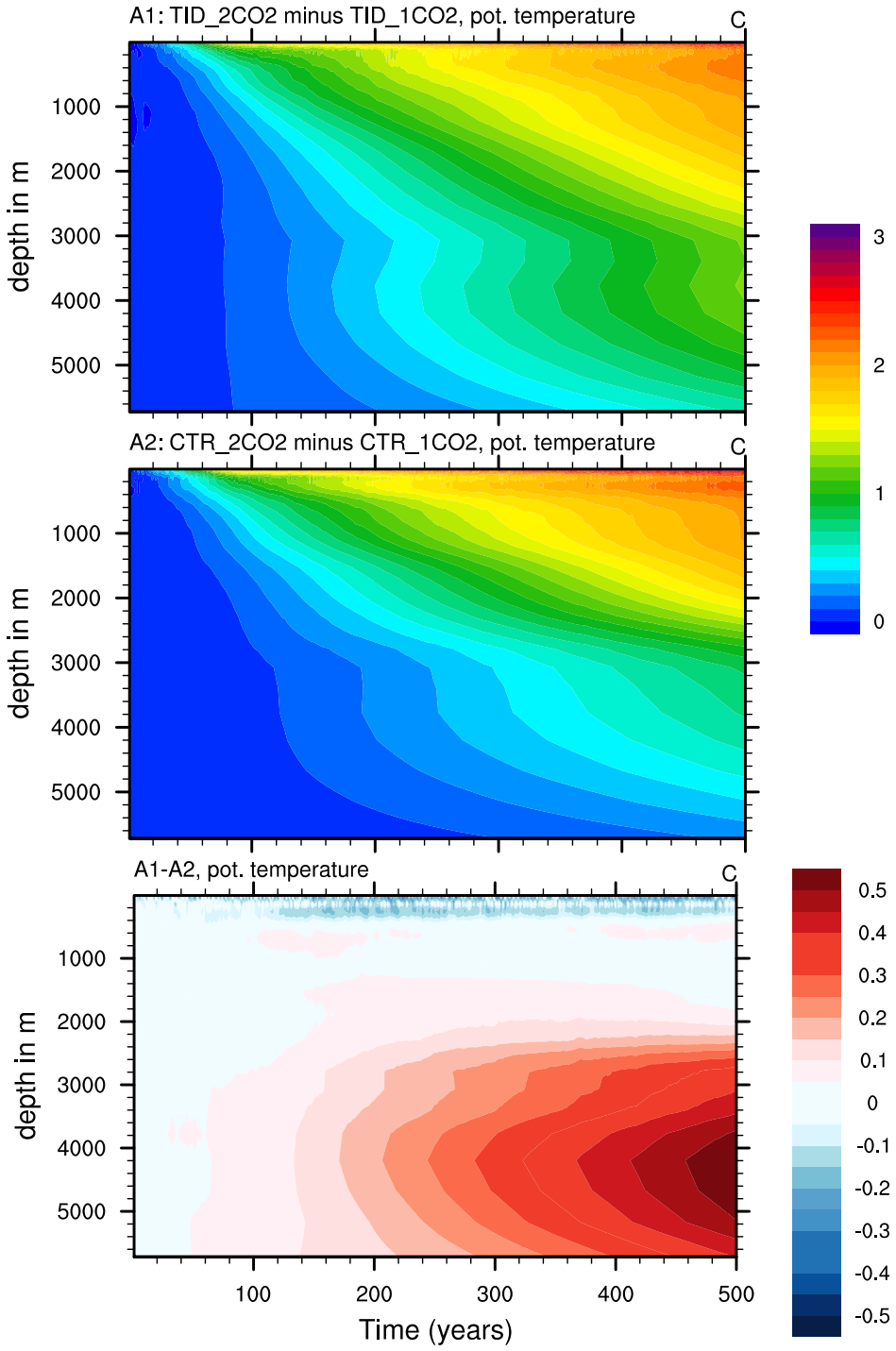

Figure 3.24: Hovmoeller type diagram for the response in global-mean ocean temperature (in °C) for TID (top), CTR (middle) and their difference (bottom).

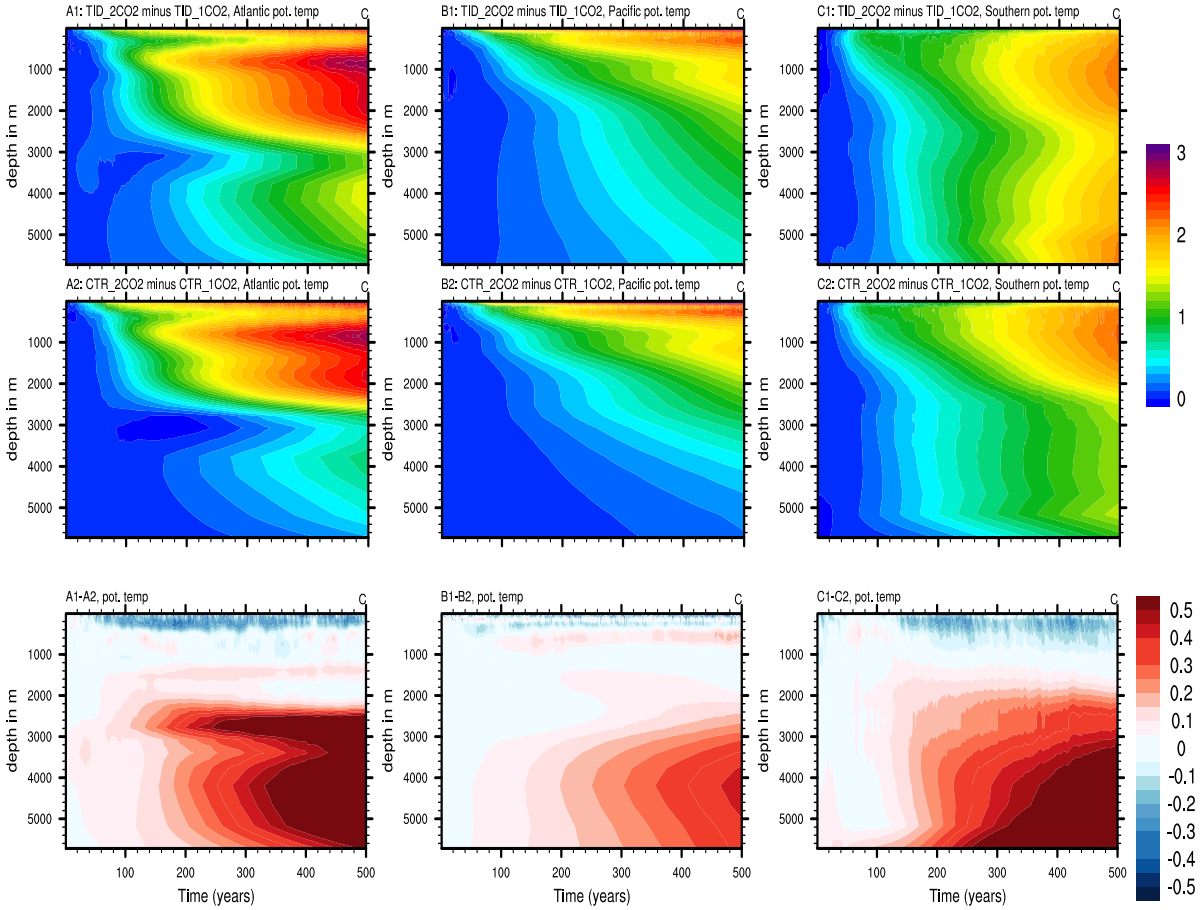

Figure 3.25: Hovmoeller type diagram for the response in ocean temperature (in °C) for TID (top), CTR (middle) and their difference (bottom), for the Atlantic (left), Indo-Pacific (middle) and Southern Ocean (right).

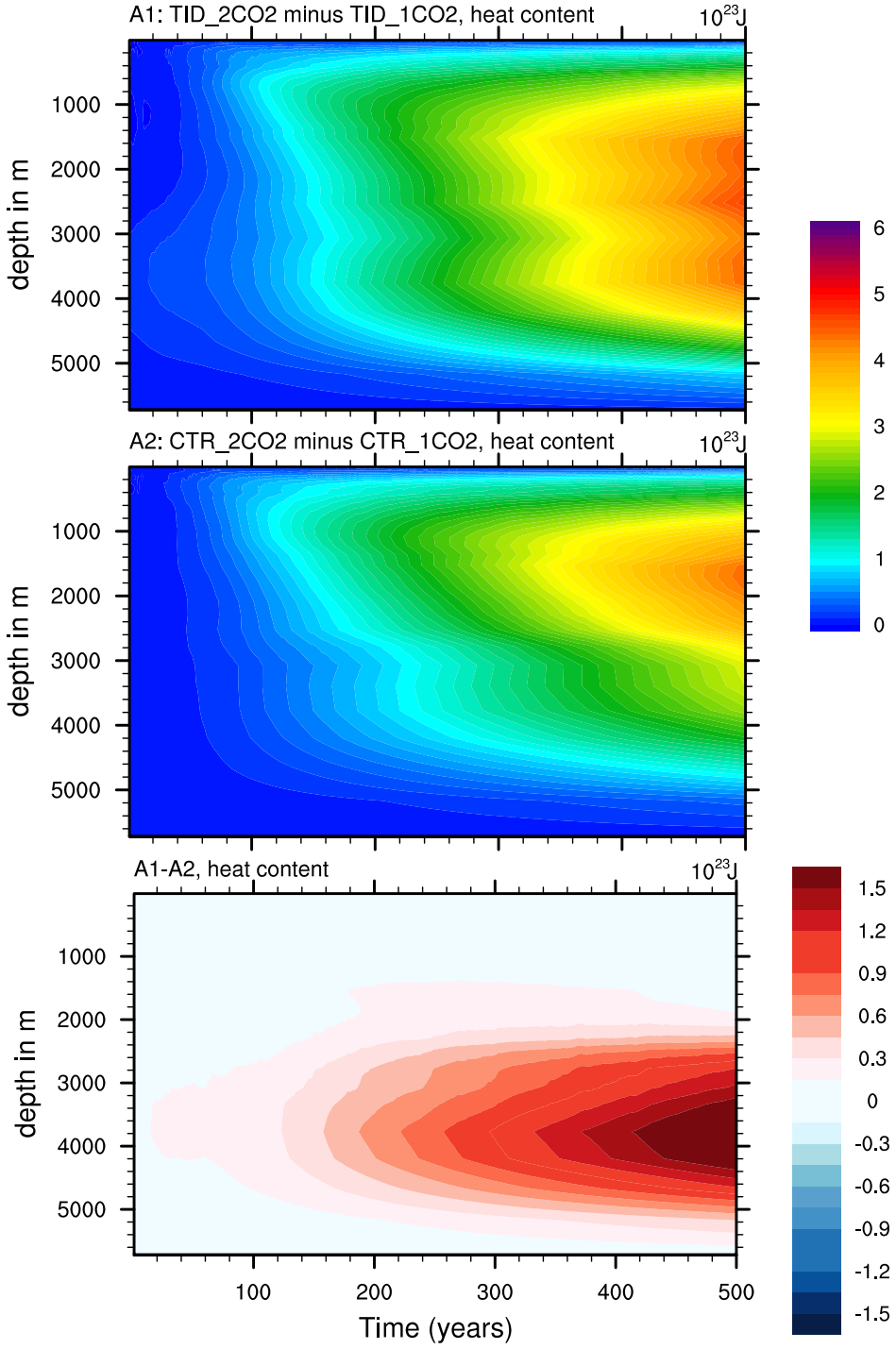

Figure 3.26: Hovmoeller type diagram for the response in ocean heat content change (in 10^{23} J) for TID (top), CTR (middle) and their difference (bottom).

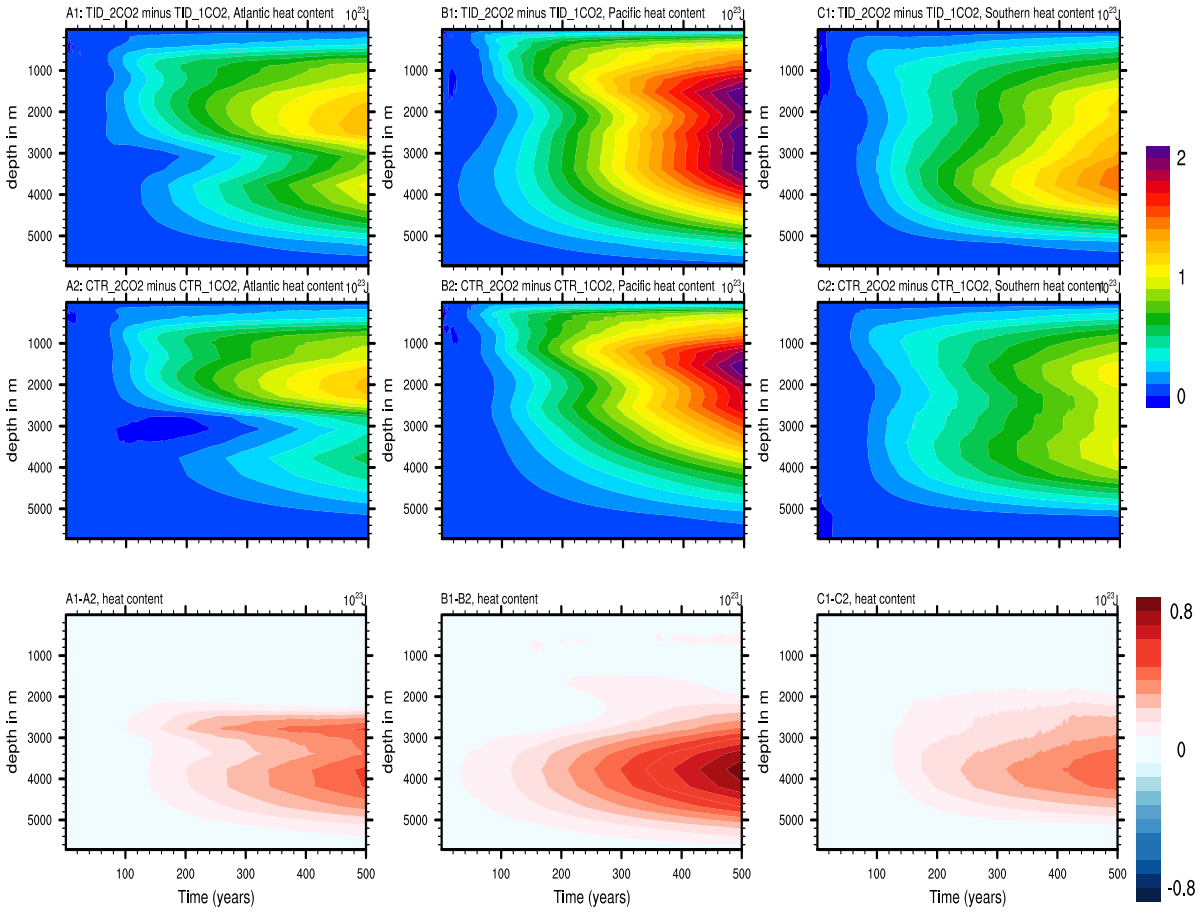

Figure 3.27: As in Fig. 3.25 but for the response in ocean heat content (unit is 10^{23} J).

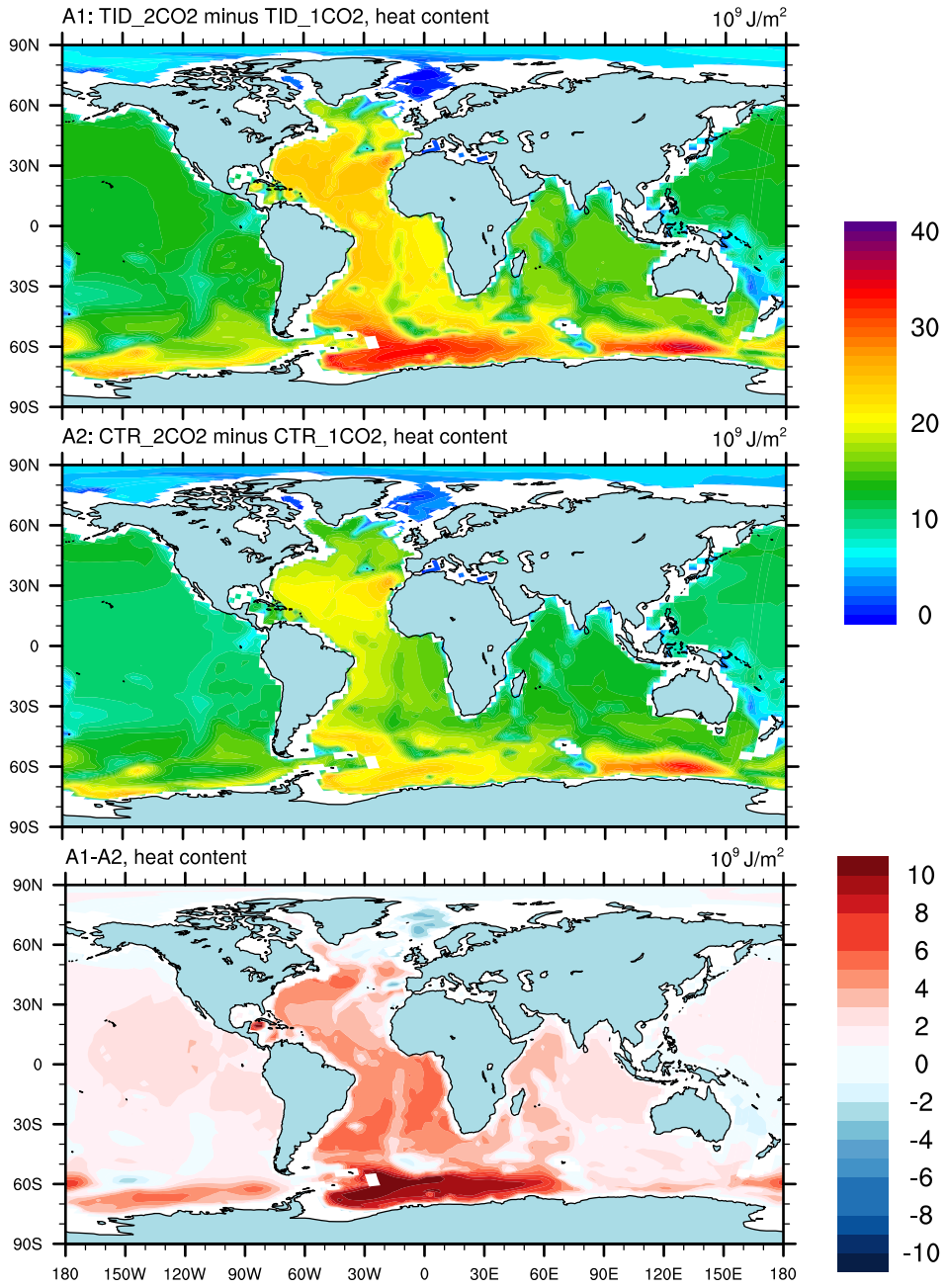

Figure 3.28: Vertically integrated (between 1000 and 4000 m depth) ocean heat content change, calculated from $\int_{-H}^{z} c\Delta T(x,y,z)\mathrm{d}z$, (unit is 10^9 J m^{-2}) for $\mathrm{TID}_{2\mathrm{CO}2}$ (top), $\mathrm{CTR}_{2\mathrm{CO}2}$ (middle), and their difference (bottom).

3.5.2 The role of surface heat fluxes changes

Russell (2006) used a kitchen metaphor to compare the ocean heat uptake and the atmospheric warming: in a kitchen with a warming oven, the wider the oven door opens, the warmer the kitchen will become, and the slower the oven will warm up. If the kitchen is the World Ocean and the oven is the atmosphere, the more the ocean heat uptake is (wider oven door opening), the slower the warming rate of the atmosphere will be (slower warming up of the oven). The metric for how wide open is the kitchen door in our experiments, is the heat fluxes at the sea surface.

The time series of the global-mean heat fluxes at the sea-surface are in Fig. 3.29 (positive is downward). The last 200-year time-mean before the beginning of the CO_2 doubling the fluxes are close to zero ($\sim 0.16\,\mathrm{W/m^2}$) implying that the simulations are very close to equilibrium. When the forcing begins there is a rapid increase of fluxes into the ocean, up to almost $2.5\,\mathrm{W/m^2}$, and then the fluxes start decreasing again. At the last 100 years, the surface fluxes are $1.15\,\mathrm{W/m^2}$ in CTR and $1.30\,\mathrm{W/m^2}$ (+13%) in TID.

If the kitchen-oven analogy works, integrating the fluxes over the 500-years time period and over the entire ocean surface area would roughly equal the additional heat stored in the ocean during that time period:

$$Q_{\mathrm{OCEAN}} = \int\int\int \mathrm{Fluxes}\,\mathrm{d}x\,\mathrm{d}y\,\mathrm{d}t.$$

The difference between the values acquired for TID and CTR when applying the formula above is $1.01 \times 10^{24}\,\mathrm{J}$. This value is roughly equal to the difference in total ocean heat uptake between TID and CTR at the end of the 500-year period ($1.06 \times 10^{24}\,\mathrm{J}$, Table 3.2). Therefore, tidal mixing opens wider the door to the deep ocean, which leads to more heat removal from the warming atmosphere, thus slowing down the atmospheric heating rate.

3.6 Quantifying processes responsible for changes in deep ocean ocean heat uptake

In the previous section we argued that the weaker response in the experiment with tidal mixing is caused by stronger deep ocean heat uptake. The total ocean heat uptake in the World Ocean in TID is 13% larger than CTR. TID also stores more efficiently heat in the deep ocean, leaving the TID upper ocean response weaker than in CTR. We also showed that TID stores more efficiently heat in Atlantic and Southern Ocean. The mechanism of how the difference in heat uptake occurs, remains to this point unaddressed. To investigate this mechanism, we look into the vertical heat transports, or the ways heat is transported in the vertical direction in the interior of the ocean.

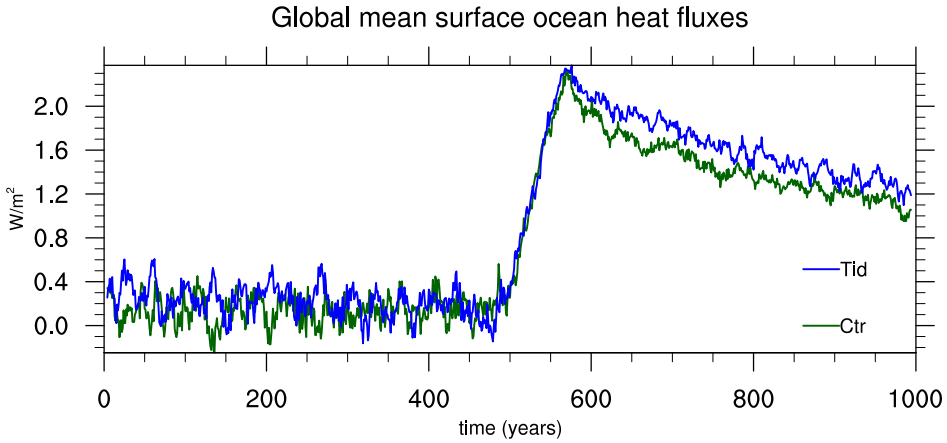

Figure 3.29: Time series of global mean surface ocean heat fluxes (in W/m^2, 10-year running mean). Positive means that fluxes go into the ocean.

Differences in the ocean heat uptake between TID and CTR lie into the different ways heat is transported in the ocean during the transient climate change. According to intuition the larger diffusion in TID could be responsible for the stronger, through diffusion, transport of heat into the deep ocean. However, we show that the relation between tidal mixing and deep ocean heat uptake is an indirect and counter-intuitive one.

Numerous past studies examine in detail the vertical heat fluxes in global warming experiments. Wiebe and Weaver (1999) found that the Gent-McWilliams scheme reduces the efficiency of ocean heat uptake in the transient climate change. In the study of Gregory (2000) the dominant region for the heat uptake is the Southern Ocean (SO), and it is the reduction in the SO isopycnal diffusion, resulting from reduced convection, that leads to reduction in ocean heat loss on the SO (net heat gain). Huang et al. (2003b) found that the ocean heat content in the transient climate increases with diapycnal diffusion of temperature. Huang et al. (2003a) examined the sensitivity of the deep ocean heat uptake to sub-grid scale parameterizations. The main conclusion is that the penetration of heat occurs mainly in high latitudes and that the deep ocean heat uptake increases due to reduced convection and Gent-McWilliams mixing (reduced cooling) in the NH and reduced Gent-McWilliams mixing (reduced cooling) in the SH. Huang et al. (2003c) found out that the total ocean heat uptake is insensitive to the diffusivity value used in Gent-McWilliams-Redi isopycnal diffusion scheme. There are regional changes occurring, but they cancel out in the global mean fluxes. Dalan et al. (2004) examined the sensitivity of transient climate to diapycnal diffusivity in a coupled atmosphere-ocean intermediate complexity model. Experiments were performed with a spatially constant diapycnal diffusivity that ranges from low to high values. The main finding in tis study was that the ocean heat uptake increases with increasing diapycnal

diffusivity. The increased ocean heat uptake was related not to diffusivity directly, but to reduction of Gent-McWilliams and isopycnal diffusion fluxes. The magnitude of decrease of the latter fluxes were found to be proportional to their control values, which in turn are associated with diffusivity through the thickness of the thermocline. Saenko (2006) examined the sensitivity of transient climate to the same tidal mixing scheme as in our study, in a idealized geometry ocean model coupled with an energy-moisture balance atmospheric model. The deep ocean heat uptake was found to be larger in the case of the relatively large, horizontally homogeneous diffusivity.

Our study of the ocean heat transports is complementary to the studies described above. Its uniqueness lies on the fact that we use a far more realistic setting than the studies above, almost all of which are using idealized settings, or lower hierarchy models.

Four processes transport heat in the model: advection, diffusion, convection, and advection due to mesoscale eddies. Advection is part of the model solution, the other three processes are sub-grid scale, hence are parameterized. Convection is parameterized using a convective adjustment scheme (Marsland et al., 2003); vertical diffusion is parameterized following the PP scheme (Pacanowski and Philander, 1981); isopycnal diffusion for tracers is parameterized following Griffies et al. (1998); isopycnal advection due to sub-grid scale eddies follows the scheme of Gent and McWilliams (1990) (we refer to is as GM scheme). Therefore, the balance is

$$\frac{\partial T}{\partial t} = \text{Advection} + \text{Diffusion} + \text{GM eddy advection} + \text{Convection}, \tag{3.3}$$

where the first term on the left hand side is the temperature tendency, that is balanced by advection, diffusion, GM eddy advection, and convection.

To calculate the heat transports, we put additional diagnostics in the model that diagnose in each time-step the temperature change due to each one of the four different processes of Eq. 3.3. A verification that our diagnostics are correct is proved by the fact that the sum of the time integrals of all the diagnostics over a time period is equal to the total temperature difference ΔT in this period. These diagnostics are in $\mathrm{K\,s^{-1}}$. To convert them into $\mathrm{W\,m^{-2}}$ (units of fluxes) we multiply them with the volumetric heat capacity c ($c = 4.1 \times 10^6\,\mathrm{J\ m^{-3}\,K^{-1}}$) and we integrate them over depth. For convenience, we diagnose the total (vertical plus horizontal) fluxes due to diffusion, rather than having separately the isopycnal and diapycnal component. The reason is that in the model it is calculated in the z-coordinate rather than in isopycnal surfaces at each time step, therefore it would not be straightforward to convert the vertical/horizontal in each time step to isopycnal/diapycnal. Therefore, in the coming analysis, we compare total diffusion with total advection, as well as convection and GM advection.

We have the diagnostics (hence the heat transports) for years $0-100$ of the transient

climates. We discuss the heat transports in the first 10-year period of the transient climate (named 'TRANS1', look also Fig. 3.2), and the difference between the transports of the last 10-years of the transient climate ('TRANS2') and the transports of TRANS1. We examine the transports in the World Ocean and in the different basins: Atlantic, Indo-Pacific, and Southern Ocean.

3.6.1 Vertical heat transports at the first 10 years of the transient climate

The global-mean vertical heat fluxes are shown on Fig. 3.30. If a process has positive (negative) fluxes at a certain level, it means that this process leads to increase (decrease) of the temperature, and therefore of the heat content, at that particular level. The sum of all processes at each level should be zero at equilibrium, because the temperature tendency of Eq. 3.3 becomes zero, and all the processes then balance each other. Since TRANS1 is not far from quasi-equilibrium and the anomaly fluxes at sea surface due to increased CO_2 have not yet spread in the deep ocean, the total vertical fluxes should be close to zero during TRANS1. This is true for both TID and CTR (total fluxes are smaller than $0.05\,\mathrm{W/m^2}$ in TID and $0.02\,\mathrm{W/m^2}$ in CTR), even though there is a small drift in TID below 3000 m. However, this drift should not pose a problem in the coming analysis, because in the differences between TRANS2 and TRANS1, assuming that the drift remains the same through out the transient climate, it cancels out.

In CTR, above 3000 m depth, advection and diffusion fluxes are positive, therefore increasing the heat content of the World Ocean at these depths, and they are balanced by convection and GM advection fluxes, that are instead decreasing the heat content of the ocean. To understand the positive diffusion fluxes is intuitively straightforward: heat is diffused from the sea surface downwards. Positive advection fluxes means that heat converges through advective motion at these depths, and since the water masses are warmer closer to the sea surface, positive advection fluxes imply that there is more warmer sinking than cooler rising water, on the global-mean. Negative convection fluxes is due to that convection occurs due to ocean cooling at the sea surface at high latitudes: cooling of the upper ocean implies that heat is removed from the ocean to the atmosphere. Negative GM advection fluxes mean that the isopycnal diffusion due to mesoscale eddies is removing heat from the ocean. Below 3000 m depth, convection and GM fluxes are not significant, and the main balance is between positive diffusion and negative advection fluxes.

In TID, the general picture is the same qualitatively as in CTR. However, there is an important difference: TID diffusion fluxes are larger than in CTR, especially below 3000 m depth. This is direct result of the tidal mixing scheme that leads to stronger diffusivities at large depths. And since at these depth the balance is between advection and diffusion, the TID advection fluxes are also enhanced.

In Fig. 3.30 the vertical heat fluxes for each basin are also shown. The balances for

each basin are not different in a qualitative manner if we compare TID and CTR; what constitutes the major difference between the two experiments is the magnitude of the fluxes in TID: its advection and diffusion fluxes are significantly enhanced compared to CTR in all basins, especially below 2000 m depth. This is a direct consequence of the tidal mixing, which leads to stronger advection, related to the stronger circulation in quasi-equilibrium in experiment TID (Section 3.3.1).

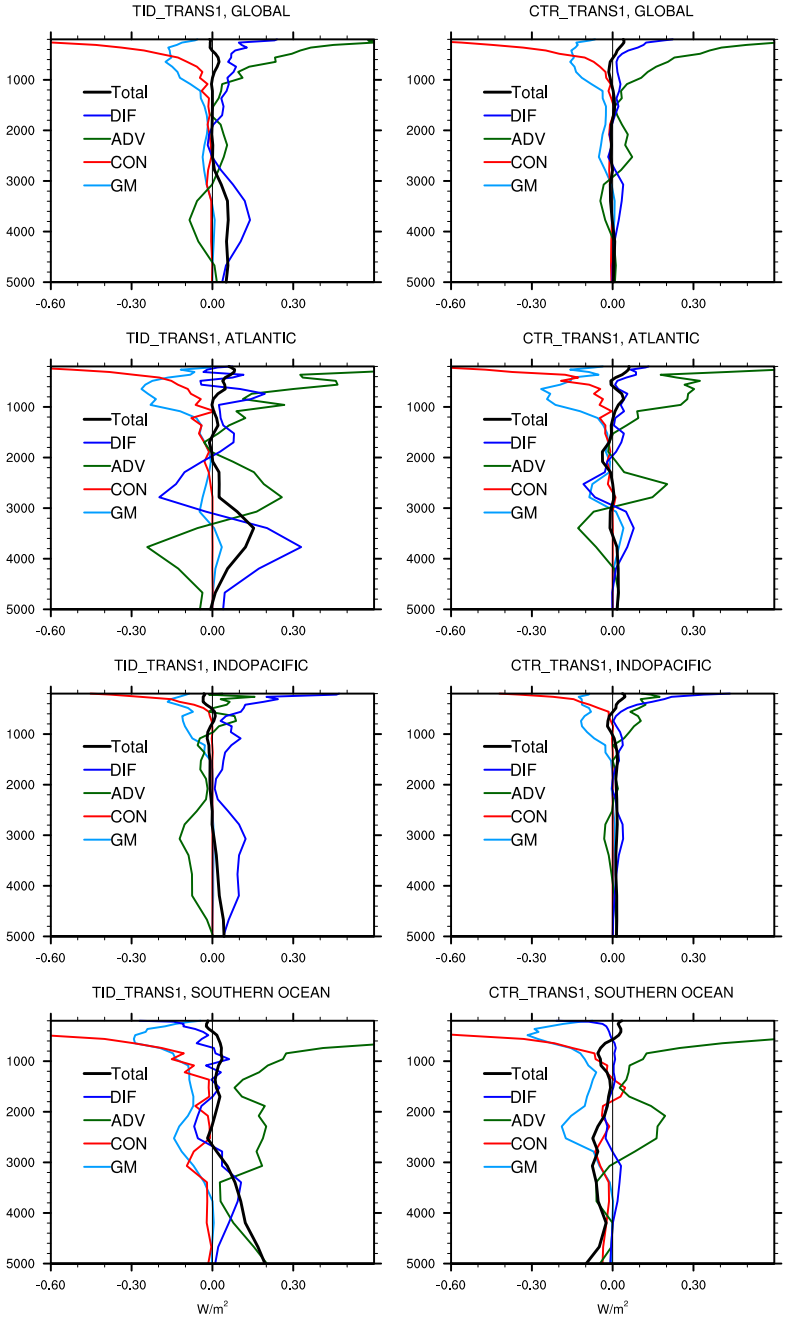

Figure 3.30: Vertical heat fluxes in the ocean (in W/m^2) during TRANS1 time period, for TID (left) and CTR (right), averaged in World Ocean (top), in Atlantic (second row), in Indo-Pacific (third row), and in Southern Ocean (bottom row). Total fluxes, as well as fluxes due to advection, diffusion, convection and GM advection are shown.

3.6.2 Differences in vertical heat transports between the last and first 10 years of the transient climate

In Fig. 3.31 the differences in heat transports between TRANS2 and TRANS1 are shown for CTR and TID, for the World Ocean, as well as the three major ocean basins. Positive differences in either one of the four processes of Eq. 3.3 imply that in TRANS2 that particular process is modified in such a way that it increases the heat content of the ocean, hence resulting in ocean heat uptake. The sum of the differences of all processes, therefore, corresponds to the total heat uptake during the transient period.

In CTR, the total fluxes increase from surface to bottom, by up to $0.15\,\mathrm{W/m^2}$ at 600 m depth, and by up to $0.04\,\mathrm{W/m^2}$ at depths between $3000 - 5000$ m. Surprisingly, the process that is responsible for the increase in the total fluxes, from $600 - 5000$ m depth, is advection, rather than diffusion or GM eddy advection, as we might have anticipated from previous studies described above. Above 600 m, changes in convection are responsible for the warming in the upper layers. Convection, as we discussed for the TRANS1 period, is cooling the upper ocean. In the transient climate convection is reduced, due to warming and freshening of the high latitudes. Reduction in convection leads to weaker ocean heat loss, or net ocean heat gain.

Looking at each ocean basin separately (second to fourth row of Fig. 3.31) we can investigate the relative role of each basin in the global-mean heat uptake in CTR. In Atlantic there is significant increase in total ocean heat fluxes (up to $0.02\,\mathrm{W/m^2}$) until 3000 m, but no increase below that depth. In Indo-Pacific the increase in total fluxes is relatively unimportant below 1500 m, but the total fluxes increase in a narrow depth layer from $400 - 1200$ m depth, by up to $0.015\,\mathrm{W/m^2}$ peaking at 800 m depth. In the Southern Ocean there is a very large increase in total fluxes, more than 0.2 $\mathrm{W/m^2}$, from $1000 - 5000$ m depth. The general picture, hence, for CTR is that Atlantic is important for ocean heat uptake above 3000 m depth, the Southern Ocean is important in depths $1000 - 5000$ m, whereas the Indo-Pacific is relatively unimportant, except for a narrow depth layer from $400 - 1200$ m. The above results are consistent with what we discussed in Section 3.5: the largest heat content change per unit area in CTR occurs in Atlantic and Southern Ocean (Fig. 3.28). The increase in total fluxes occurs due to either changes in convection (in the upper layers until 600 or 800 m depth), or due to changes in advection (from 800 m to bottom).

The major difference between TID and CTR in the total fluxes of the Wold Ocean (upper row of Fig. 3.31) is that the increase in total fluxes is distributed much more evenly with depth (at the value of about $0.1\,\mathrm{W/m^2}$), instead of peaking at 800 m depth as in CTR. The surface warming therefore spreads from the upper to the lower ocean more efficiently in TID. Again, as in CTR, changes in advection are responsible for the increase in the TID fluxes below 800 m, and changes in convection above 800 m. The fluxes at different ocean basins reveal that, first, as in CTR, the largest heat uptake in

TID takes place in Atlantic and Southern Ocean, and second, the large increase of TID compared to CTR is stronger in these two basins rather than in the Indo-Pacific Ocean, consistent with Fig. 3.28. In the deep ocean, even though there is some contribution to the increase of total fluxes from Atlantic and Indo-Pacific, it is the Southern Ocean that dominates in deep ocean heat uptake in experiment TID.

It is surprising that changes in TID total fluxes are mainly due to changes in advection, rather that diffusion, as we might have expected. Therefore, there is no direct relationship between tidal mixing and larger deep ocean heat uptake. Instead, there is an indirect relation, through the impact of tidal mixing on advection.

The description of the zonal distribution of the heat fluxes is missing from the basin-mean fluxes shown in Fig. 3.31. Fig. 3.32 shows the differences between TRANS2 and TRANS1 total heat fluxes, as well as fluxes due to advection and convection, that are zonally averaged for the global ocean. In CTR, there is an increase in the total heat fluxes, hence there is heat uptake, in high latitudes, close to the sea surface and up to 2000 m depth in the NH, and between $1500 - 5000$ m depth in the SH. Other modeling studies (Gregory, 2000; Bitz et al., 2006) also predict that the NH high-latitude warming is close to the sea surface and that the SH high-latitude warming is deep, below 1 km depth. The high-latitude warming in the upper km of the ocean is caused by reduction in convection at these latitudes. In the upper ocean, changes in advection fluxes oppose the warming cause by reduced convection. In the lower ocean, especially in the SH, changes in advection are responsible for the heat uptake.

The difference in fluxes in TID differ from CTR in two striking features: first, the increase in the upper ocean heat fluxes in both NH and SH high latitudes is much weaker in TID than in CTR. Second, the increase in the lower ocean heat fluxes, particularly in the deep Southern Ocean, is stronger in TID than in CTR. The upper ocean NH high-latitude warming is weaker in TID, even though its reduction in NH convection is strong and spreads deeper than in CTR. However, changes in advection at the same latitudes cancel out the warming due to convection. The net result in the zonal-mean World Ocean is that the upper NH ocean warming is weak or absent in TID. The same applies for the SH warming due to reduced convection, at 70° S and at $400 - 1400$ m depth; advection at the same latitude and depth cancel out the warming effect due to convection. The Southern Ocean deep warming in TID is both stronger and covers larger area than in CTR; advection changes are also here responsible for this warming. Overall, the larger heat uptake in TID is due to the large scale advection. Reduction in convection seems to be stronger in TID than in CTR. Advection, however, seems to cancel out the convection-induced warming in the upper ocean of TID.

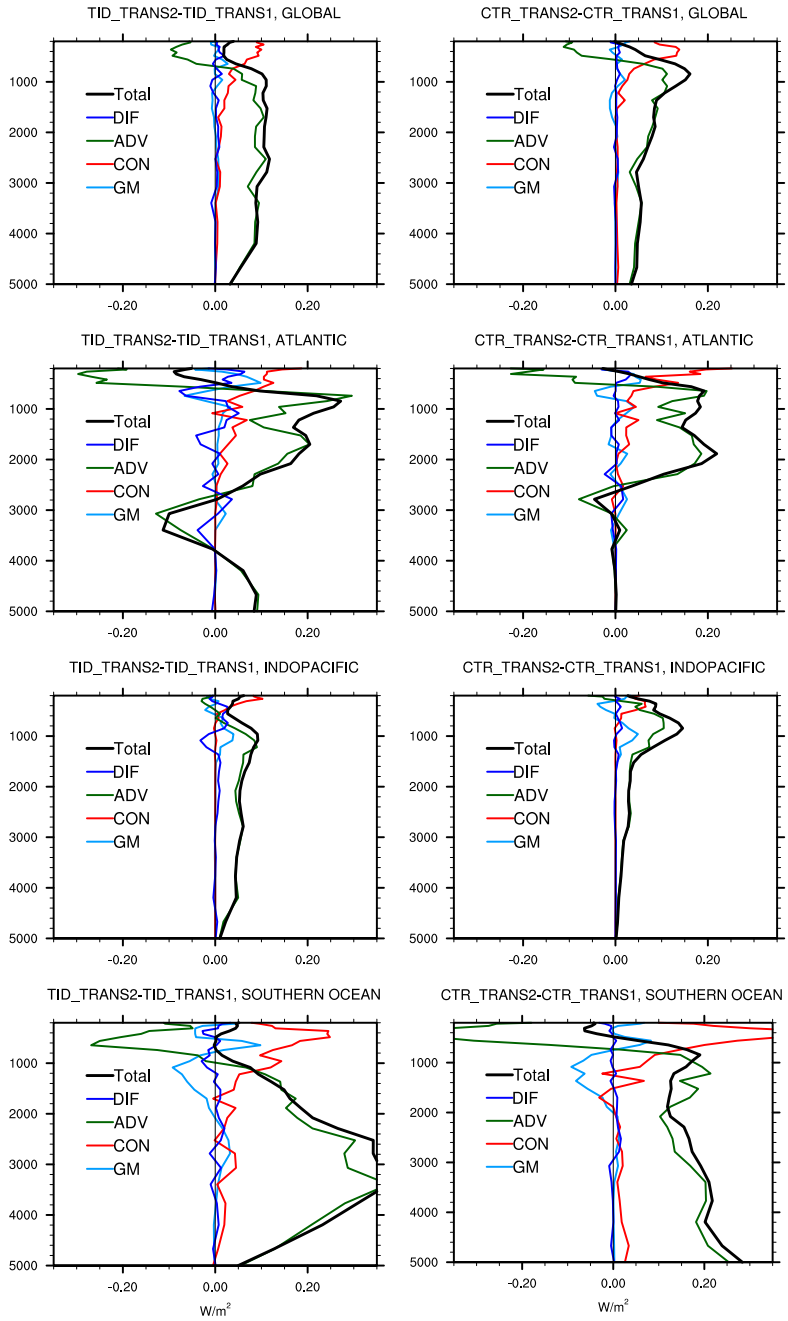

Figure 3.31: Differences in vertical heat fluxes (in W/m^2) between TRANS2 and TRANS1, for TID (left) and CTR (right), averaged in World Ocean (top), in Atlantic (second row), in Indo-Pacific (third row), and in Southern Ocean (bottom row). Total fluxes, as well as fluxes due to advection, diffusion, convection and GM advection are shown.

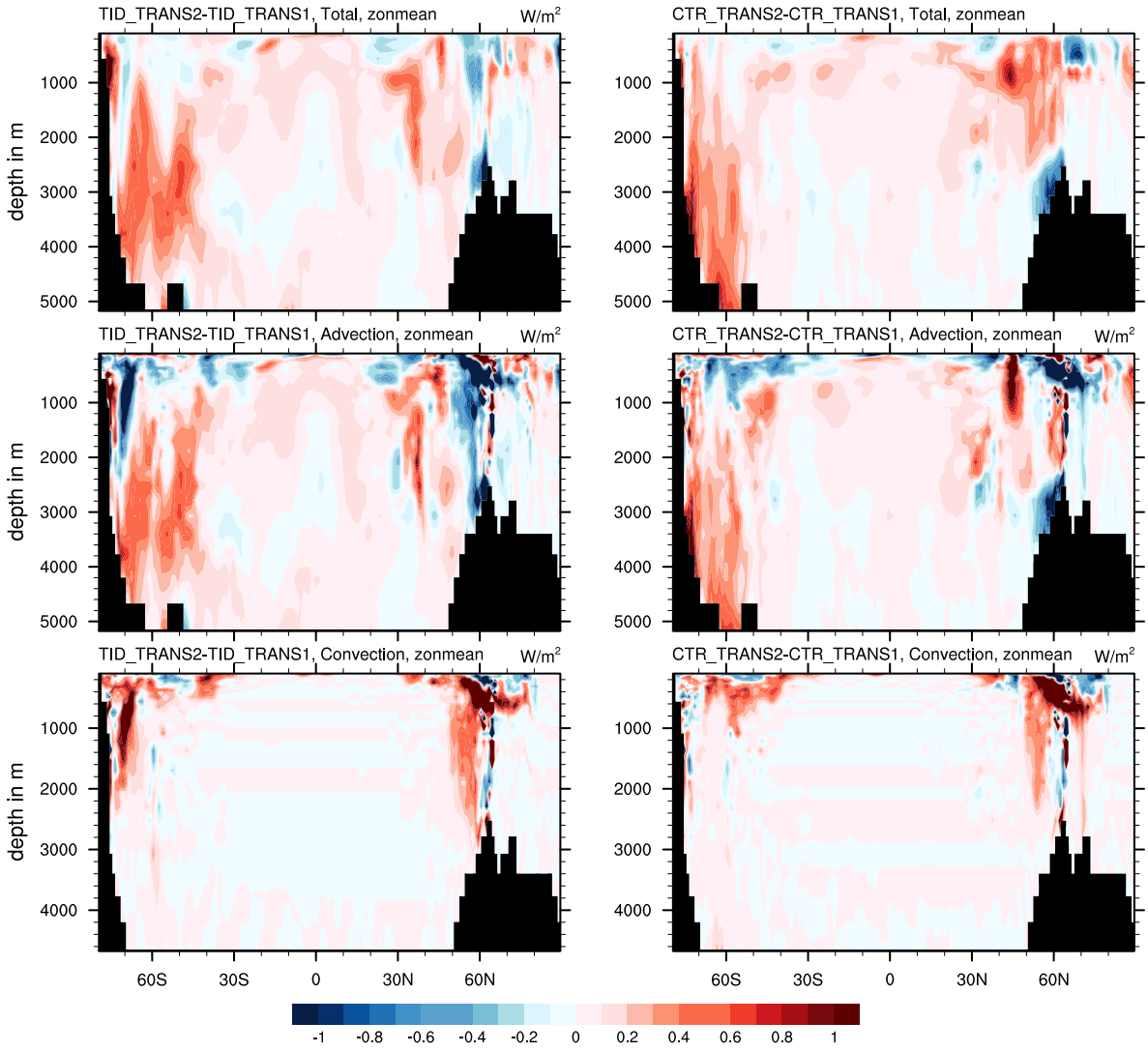

Figure 3.32: Differences in zonal-mean heat fluxes (in W/m^2, zonal averaging is in the World Ocean) between TRANS2 and TRANS1, for TID (left) and CTR (right), for total fluxes (top), fluxes due to advection (middle) and due to convection (bottom).

3.7 Summary and discussion

We investigate the sensitivity of the transient climate change for a global warming scenario to a tidal mixing scheme (Laurent et al., 2002). The new scheme parameterizes diapycnal diffusivity depending on the location of energy dissipation over rough topography, whereas the standard configuration uses horizontally constant diapycnal diffusivity. We perform experiments with two setups of the state-of-the-art coupled AOGCM ECHAM5/MPIOM, one setup with the tidal mixing scheme (TID) and the second setup with the standard configuration (CTR). We integrate TID and CTR with pre-industrial CO_2 concentration until quasi-equilibrium is reached (TID_{1CO2} and CTR_{1CO2}).

Differences between TID_{1CO2} and CTR_{1CO2} occur in mass/heat transports, temperature/salinity distributions, sea ice conditions, and near-surface air temperature fields. The circulation, hence the mass transports, in the model ocean in TID_{1CO2} is significantly stronger than in CTR_{1CO2}, particularly for the lower cell (below 3000 m depth), where TID_{1CO2} circulation is up to 80% stronger than CTR_{1CO2}. The strengthening of the circulation in TID_{1CO2} is occurring in both Atlantic and Indo-Pacific. The stronger Indo-Pacific circulation at the deep ocean in TID_{1CO2} is in better agreement with observational estimates (Talley et al., 2003). Stronger deep circulation in TID_{1CO2} occurs because its meridional density gradient is larger than CTR_{1CO2}, despite that the deep ocean in TID_{1CO2} is warmer and fresher, hence overall less dense than CTR_{1CO2}. Similar results for the strengthening of the circulation due to tidal mixing were found in the uncoupled MPIOM experiments of Chapter 2 (Exarchou et al., 2011). Heat transports in TID_{1CO2} are stronger than CTR_{1CO2}, consistent with the stronger mass transports of TID_{1CO2}. Larger heat transports in TID_{1CO2} are associated to its smaller sea-ice area and thickness in both northern and southern hemisphere. The sea ice conditions in TID_{1CO2}, in turn, lead to larger temperatures in the polar regions compared to CTR_{1CO2}. Less sea ice in TID_{1CO2} implies larger ocean areas without insulation to the cold polar atmosphere, hence the upward latent and sensible heat fluxes from the ocean to the atmosphere increase, leading to a warmer atmosphere in the polar regions of TID_{1CO2}.

After the quasi-equilibrium integration, we preform ensemble integrations with CO_2 increasing 1% per year, until CO_2 doubling (year 70) and keep the CO_2 concentration constant to $2\times CO_2$ for another 430 years. We investigate the response, defined as the difference between the last 100 years of the CO_2 perturbation experiments (TID_{2CO2} and CTR_{2CO2}) and the last 200 years of the quasi equilibrium climates (TID_{1CO2} and CTR_{1CO2}). We focus on the difference in the response caused by tidal mixing.

The response in the CTR MOC is that its circulation becomes mostly weaker in all ocean basins. Weakening of the circulation is a result of high-latitude warming and freshening, and is common among coupled models (Gregory et al., 2005; Solomon

et al., 2007). Tidal mixing modifies the response: its circulation weakens even more than in CTR, particularly in the deep ocean, where tidal mixing is stronger. Ocean heat transports in CTR, with few exceptions, decrease, due to the decrease in the ocean mass transports. Tidal mixing has a mixed impact on these responses: the reduction in heat transports in TID is mostly stronger in the NH, whereas in the SH the reduction is weaker between $15^\circ - 50^\circ$ S, but stronger between $50^\circ - 70^\circ$ S. The latter results from stronger increase of zonal wind stress over these latitudes in the experiment with tidal mixing. The responses in the sea-ice conditions of CTR to the increasing CO_2 include complete summer sea-ice loss and winter sea-ice melting. Tidal mixing leads to weaker summer sea-ice loss and less winter sea-ice melting. The reasons for the weaker response in the sea-ice conditions in TID are in its weaker near-surface temperature response. Its global-mean SAT response is 9% smaller than in CTR. Moreover, polar amplification in TID is weaker than in CTR: the normalized maximum polar warming in TID is 10% and 17% smaller than in CTR in NH and SH, respectively.

The weaker warming in TID in the transient climate change is caused by a stronger ocean heat uptake. The total ocean heat uptake is 13% larger in TID than in CTR. The deep ocean heat uptake in TID is 40% larger than in CTR. The largest ocean heat uptake per surface unit in TID is taking place in Atlantic and Southern Ocean. The larger total ocean heat uptake in TID is seen in its ocean-surface heat fluxes: they are 13% stronger than in TID. Therefore, more heat removal from the atmosphere to the ocean in TID results to its weaker atmospheric heating rate.

The analysis of the ocean vertical heat transports reveals that TID has stronger heat uptake than CTR due to larger changes in advective fluxes, rather than diffusive fluxes. The larger changes in advective fluxes in TID than in CTR are associated with the larger overall reduction in the overturning circulation in TID. An exact mechanism of how changes in advection result in larger heat uptake, is not investigated here, and it could be a subject of a future study. Therefore, the large-scale advection is more strongly modified when tidal mixing is included, which results in net heat uptake by the ocean. The relationship between tidal mixing and large deep ocean heat uptake is an indirect and counter-intuitive one.

3.8 Conclusions

We use the state-of-the-art coupled AOGCM ECHAM5/MPIOM to investigate the effect of tidally driven mixing on the transient climate response to CO_2 increase. Our main results are:

1. The expected response to a CO_2 doubling, that is a reduction of MOC and the northward heat transports, and a surface warming characterized by polar amplification and sea ice melting, is altered by the tidal mixing. More specifically, tidal mixing enhances the MOC-reduction by 30% in the upper cell and by 50% in the lower cell of the World Ocean. The simulation with tidal mixing has stronger reduction in the northward heat transport by 40% in the NH, by 50% in the SH between $50^\circ - 70^\circ$ S, and weaker reduction by 16% in the SH between $15^\circ - 50^\circ$ S. Tidal mixing reduces the surface warming, by about 9%, and polar amplification, quantified by the normalized maximum polar warming, by 9% in the NH and by 17% in the SH. Tidal mixing also leads to both weaker summer sea-ice area loss, and less late-winter sea-ice melting.

2. The reduction of the surface warming in the experiment with tidal mixing results from stronger ocean heat uptake. The total heat content storage in the global ocean increases by 13% due to tidal mixing.

3. The changes in the ocean heat uptake are caused by advection, i.e. caused by the different response in the circulation indirectly induced by the tidal mixing, rather than directly by the additional diffusion provided by the tidal mixing.

Chapter 4

Conclusions and Outlook

4.1 Conclusions

We summarize the conclusions of the present study by answering the questions posed in Chapter 1.

We implemented in the ocean general circulation model MPIOM the tidal mixing scheme of Laurent et al. (2002), which parameterizes diapycnal diffusivity depending on the location of tidal energy dissipation over rough topography. The tidal mixing scheme requires a bottom roughness map that can be chosen depending on the scales of topographic features one wants to focus on. Different scales of topographic features would imply a different structure of tidal mixing, hence different structure of diapycnal diffusion. Previous studies based on observations and on theoretical arguments suggest that small scale topographical features with length scales $1-10$ km should be considered on the formulation of the bottom roughness map. However, previous modeling studies that implemented the tidal mixing scheme of Laurent et al. (2002) did not take such arguments into account. In our study we attempted to cover this gap. In Chapter 2, we discussed experiments using the ocean general circulation model MPIOM, and addressed the following research questions:

(1) What is the impact of different scales of bottom roughness on the general circulation?

Simulations that include the tidal mixing scheme with different scales of bottom roughness have different equilibrium solutions for the circulation. The strength of the bottom circulations increases with decreasing roughness length, whereas the AMOC behaves in a more complex manner: it increases everywhere in the experiment with large-scale roughness, increases only at depths between 1000-3000 m in experiment with medium-scale roughness, and decreases at depths between 2000-3000 m in experiment with small-scale roughness. Thus, when implementing the tidal mixing scheme, one should take the sensitivity of the results on the formulation of bottom roughness into account.

(2) Do tidally-induced changes in convection drive the strong bottom water transports in the simulations with tidal mixing?

No. Tidal mixing in convection regions is not responsible for the large enhancement of the bottom water transport in the simulations with tidal mixing. Local changes in water masses properties affect the bottom circulation, without necessarily having convection played a dominant role.

(3) Does tidal mixing improve the MPIOM solution?

Yes. The bottom water transports in the Pacific Ocean are enhanced when tidal mixing is taken into account, which is significantly closer to observations. All tidal simulations reduce the bias of the model at big depths, and increase it at intermediate depths. Among the tidal simulations, the one based on small-scale roughness produces the smallest biases in the deep ocean. This result is indirectly supportive of the theoretical and observational studies that tidal mixing occurs mainly on topographic features with spatial scales smaller than 10 km.

In Chapter 3, we addressed the question of the effect of tidally driven mixing on the transient climate response to CO_2 increase, by performing global warming simulations using the coupled atmosphere-ocean general circulation model ECHAM5/MPIOM. There is no other study that addressed the impact of tidal mixing on the transient climate change using such a setting as realistic as in the present study. We investigated the following questions:

(4) What is the effect of tidally driven mixing on the transient climate response to CO_2 increase?

The expected response to a CO_2 doubling, that is a reduction of MOC and the northward heat transports, and a surface warming characterized by polar amplification and sea ice melting, is altered by the tidal mixing. More specifically, tidal mixing enhances the MOC-reduction by 30% in the upper cell and by 50% in the lower cell of the global ocean. The simulation with tidal mixing has stronger reduction in the northward heat transport by 40% in the NH, by 50% in the SH between $50^\circ - 70^\circ$ S, and weaker reduction by 16% in the SH between $15^\circ - 50^\circ$ S. Tidal mixing reduces the surface warming, by about 9%, and polar amplification, quantified by the normalized maximum polar warming, by 9% in the NH and by 17% in the SH. Tidal mixing also leads to both weaker summer sea-ice area loss, and less late-winter sea-ice melting.

(5) What are the processes responsible for the modified transient climate response?

The reduction of the surface warming in the experiment with tidal mixing results from stronger ocean heat uptake. The total heat storage in the global ocean increases by 13% due to tidal mixing, 40% of which is stored in the deep ocean. The changes in the ocean heat uptake are caused by advection, i.e. caused by the different response in the circulation indirectly induced by the tidal mixing, rather than directly by the additional diffusion provided by the tidal mixing.

4.2 Outlook

Possible extension of the current study could involve a further investigation of an exact mechanism of how changes in advection result in larger heat uptake in the experiment with tidal mixing (Chapter 3).

In Chapter 3 we discussed the transient climate response to CO_2 increase. Even though the transient response in globally averaged near-surface temperature is reduced by tidal mixing, the equilibrium response (what is known as climate sensitivity) could be equal between the tidal and the control experiment. The climate sensitivity is determined by the radiative forcing and the climate feedback parameter. Using the method described in Gregory et al. (2004), in a possible extension of our study, one could estimate the radiative forcing and climate sensitivity of the control and tidal simulation.

In a more general direction, as we discussed in Chapter 1, there are two major sources of energy that are considered necessary for the ocean circulation: winds and tides. The tidal mixing scheme we considered in this study parameterizes the effect of the tides in increasing the ocean diffusivity. An extension of this study could also include the effect of the winds in mixing the ocean. As described in Munk and Wunsch (1998), there are two ways that the wind can mix the ocean. The direct way, that is associated with the outcropping of dense waters in the Southern Ocean, and the indirect way, associated with the interaction of wind-driven large-scale motion with topography and the dissipation of wind-generated internal waves in the ocean interior. Such arguments could, for example, be investigated with high resolution numerical simulations that can resolve meso-scale eddies and partially gravity waves in the ocean, like the simulations developed in the STORM project[1].

[1] https://verc.enes.org/community/projects/national-projects/german-projects/storm

Bibliography

Banks, H. T. and J. M. Gregory, 2006: Mechanisms of ocean heat uptake in a coupled climate model and the implications for tracer based predictions of ocean heat uptake. *Geophysical research Letters*, **33**.

Bitz, C. M., P. R. Gent, R. A. Woodgate, H. M. M., and R. Lindsay, 2006: The influence of sea ice on ocean heat uptake in response to increasing CO2. *Journal of Climate*, **19**, 2437–2450.

Bóe, J., A. Hall, and X. Qu, 2009: Deep ocean heat uptake as a major source of spread in transient climate change simulations. *Geophysical Research Letters*, **36**.

Bryan, F., 1987: Parameter sensitivity of primitive equation of ocean general circulation models. *Journal of Physical Oceanography*, **17**.

Dalan, F., P. H. Stone, and A. P. Sokolov, 2004: Sensitivity of the ocean's climate to diapycnal diffusivity in an EMIC. part II: Global warming scenario. *Journal of Climate*, **18**.

Dixon, K., T. L. Delworth, M. Spelman, and J. Stouffer, 1999: The influence of transient surface fluxes on north atlantic overturning in a coupled gcm climate change experiment. *Geophysical Research Letters*, **26**, 2749–2752.

Egbert, G. D., 1997: Tidal data inversion: interpolation and inference. *Progress in Oceanography*, **40**, 53–80.

Egbert, G. D. and R. D. Ray, 2003: Semi-diurnal tidal dissipation from TOPEX/Poseidon altimetry. *Geophysical Research Letters*, **30**.

Exarchou, E., J.-S. Von Storch, and J. Jungclaus, 2011: Impact of tidal mixing with different scales of bottom roughness on the general circulation in the ocean model MPIOM. *Ocean Modelling*, submitted.

Ferrari, R. and C. Wunsch, 2010: The distribution of eddy kinetic and potential energies in the global ocean. *Tellus*, **62A**, 92–108.

Furue, R. and E. Masahiro, 2005: Effects of the pacific diapycnal mixing and wind stress on the global and pacific meridional overturning circulation. *Journal of Physical Oceanography*, **35**.

Gent, P. R. and J. C. McWilliams, 1990: Isopycnal mixing in Ocean Circulation Models. *Journal of Physical Oceanography*, **20**, 150–155.

Gregory, J. M., 2000: Vertical heat transports in the ocean and their effect on time-dependent climate change. *Climate Dynamics*, **16**, 501–515.

Gregory, J. M. and J. F. B. Mitchell, 1997: The climate response to CO2 of the hadley center coupled AOGCM with and without flux adjustment. *Geophysical Research Letters*, **24**.

Gregory, J. M., et al., 2004: A new method for diagnosing radiative forcing and climate sensitivity. *Geophysical Research Letters*, **31**.

Gregory, J. M., et al., 2005: A model intercomparison of changes in the Atlantic thermohaline circulation in response to increasing atmospheric CO2 concentration. *Geophysical Research Letters*, **32**.

Griffies, S. M., R. C. Pacanowski, V. D. Larichev, J. K. Dukowicz, R. D. Smith, and et al., 1998: Isoneutral diffusion in a z-coordinate ocean model. *Journal of Physical Oceanography*, **28**, 805–830.

Hagemann, S. and L. Dumenil, 1998: A parameterization of the lateral waterflow for the global scale. *Climate dynamics*, **14**, 17–31.

Hagemann, S. and L. Gates, 2003: Improving a subgrid runoff parameterization scheme for climate models by the use of high resolution data derived from satellite observations. *Climate Dynamics*, **21**, 349–359.

Hasumi, H. and N. Suginohara, 1999: Effects of locally enhanced vertical diffusivity over rough bathymetry on the world ocean circulation. *Journal of Geophysical Research*, **104**, 2367–2374.

Hibler, W., 1979: Dynamic thermodynamic sea-ice model. *Journal of Physical Oceanography*, **9**, 815–846.

Holland, M. M. and C. M. Bitz, 2003: Polar amplification of climate change in coupled models. *Climate Dynamics*, **21**, 221–232.

Hu, A., G. A. Meehl, W. M. Washington, and A. Dai, 2004: Response of the Atlantic Thermohaline Circulation to increased CO2 in a coupled model. *Journal of Climate*, **17**, 4267–4279.

Huang, B., P. H. Stone, and C. Hill, 2003a: Sensitivities of deep-ocean heat uptake and heat content to surface fluxes and subgrid-scale parameters in an ocean general circulation model with idealized geometry. *Journal of Geophysical Research*, **108**.

Huang, B., P. H. Stone, A. Sokolov, and I. Kamemkovich, 2003b: The deep-ocean heat uptake in transient climate change. *Journal of Climate*, **16**, 1352–1362.

Huang, B., P. H. Stone, A. Sokolov, and I. Kamemkovich, 2003c: Ocean heat uptake in transient climate change: mechanism and uncertainty due to subgrid-scale mixing. *Journal of Climate*, **16**, 3344–3356.

Huang, R. X. and X. Jin, 2007: Deep circulation in the South Atlantic induced by bottom-intensified mixing over the Midocean Ridge. *Journal of Physical Oceanography*, **32**, 1150–1164.

Ito, T. and J. Marshall, 2008: Control of lower-limb overturning circulation in the southern ocean by diapycnal mixing and eddu transfer. *Journal of Physical Oceanography*, **38**.

Jacobs, S. S., A. Amos, and P. M. Bruchhausen, 1970: Ross Sea oceanography and Antarctic Bottom Water formation. *Deep Research*, **17**, 935–962.

Jayne, S. and L. C. S. Laurent, 2001: Parameterizing tidal dissipation over rough topography. *Geophysical Research Letters*, **28**, 811–814.

Jayne, S. R., 2009: The impact of abyssal mixing parameterizations in an Ocean General Circulation Model. *Journal of Physical Oceanography*, **39**, 1756–1775.

Jeffreys, H. W., 1925: On fluid motions produced by differnces of temperature and humidity. *Q. J. R. Meteor. Soc.*, **51**, 347–356.

Jungclaus, J. H., et al., 2006: Ocean circulation and tropical variability in the coupled model ECHAM5/MPI-OM. *Journal of Climate*, **19**, 3952–3972.

Kamenkovich, I. V. and P. J. Goodman, 2000: The dependecne of AABW transport in the Atlantic on vertical diffusivity. *Geophysical Research Letters*, **27**, 3739–3742.

Kuhlbrodt, T., 2008: On sandström's inferences from his tanks experiments - a hundred years later. *Tellus*, **60**, 819–836.

Kuhlbrodt, T., A. Griesel, M. Montoya, M. Hofmann, and S. Rahmstorf, 2007: On the driving processes of the Atlantic Meridional Circulation. *Review of Geophysics*, **45**.

Laurent, L. C. S., H. L. Simmons, and S. R. Jayne, 2002: Estimating tidally driven mixing in the deep ocean. *Geophysical Research Letters*, **29**.

Ledwell, J. R., E. T. Montgomery, K. L. Polzin, L. C. S. Laurent, R. W. Schmitt, and J. M. Toole, 2000: Evidence for enhanced mixing over rough topography in the abyssal ocean. *Nature*, **403**.

Lee, S.-K., W. Park, E. v. Sebille, M. O. Baringer, W. Chunzai, D. B. Enfield, S. G. Yeager, and B. P. Kirtman, 2011: What caused the significant increase in Atlantic Ocean heat content since the mid-20th century? *Geophysical Research Letters*, **38**.

Levitus, S., J. I. Antonov, T. P. Boyer, and C. Stephens, 2000: Warming of the World Ocean. *Science*, **287**, 2225–2229.

Levitus, S., et al., 1998: World ocean database 1998. *Introduction. NOAA Atlas NESDIS 18*, Ocean Climate Laboratory, National Oceanographic Data Center, U.S. Goverment Printing Office, Washington, DC, Vol. 1.

Manabe, S. and R. J. Stouffer, 1993: Century-scale effects of increased atmospheric CO2 on the Ocean-Atmosphere system. *Letter to Nature*, **364**, 215–218.

Manabe, S., R. J. Stouffer, M. J. Spelman, and K. Bryan, 1991: Transient responses of a coupled Ocean-Atmosphere model to gradual changes of atmospheric CO_2. part 1: Annual mean response. *Journal of Climate*, **4**, 785–818.

Marotzke, J., 1997: Boundary mixing and the dynamics of the three-dimensional thermohaline circulations. *Journal of Physical Oceanography*, **27**, 1713–1728.

Marsland, S. J., H. Haak, J. H. Jungclaus, M. Latif, and F. Röske, 2003: The Max Planck Institute global ocean/sea ice model with orthogonal curvilinear coordinates. *Ocean Modelling*, **5**, 91–127.

Mikolajewitcz, U. and R. Voss, 2000: The role of the individual air-sea flux components in co2-induced changes of the ocean's circulation and climate. *Climate Dynamics*, **16**, 627–642.

Montenegro, A., M. Eby, A. J. Weaver, and R. Jayne, Steven, 2007: Response of a climate model to tidal mixing parameterization under present day and last glacial maximum conditions. *Ocean Modelling*, **19**, 125–137.

Muller, C. J. and O. Bühler, 2009: Saturation of the internal tides and induced mixing in the abyssal ocean. *Journal of Physical Oceanography*, **39**, 2077–2096.

Munk, W. and C. Wunsch, 1998: Abyssal recipies II: energetics of tidal and wind mixing. *Deep Research I*, **45**, 1977–2010.

Naveira Garabato, A. C., K. L. Polzin, B. A. King, K. J. Heywood, and M. Visbeck, 2004: Widespread intense turbulent mixing in the Southern Ocean. *Science*, **303**, 210–213.

Nikurarashin, M. and G. Vallis, 2011: A theory of deep stratification and overturning circulation in the ocean. *Journal of Physical Oceanography*, **41**.

Nikurashin, M. and R. Ferrari, 2010a: Radiation and dissipation of internal waves generated by geostrophic flows impinging on small-scale topography: Application to the Southern Ocean. *Journal of Physical Oceanography*, **40**, 2025–2042.

Nikurashin, M. and R. Ferrari, 2010b: Radiation and dissipation of internal waves generated by geostrophic flows impinging on small-scale topography: Theory. *Journal of Physical Oceanography*, **40**, 1055–1074.

Nikurashin, M. and S. Legg, 2011: A mechanism for local dissipation of internal tides generated at rough topography. *Journal of Physical Oceanography*, **41**, 378–395.

Pacanowski, R. C. and S. G. H. Philander, 1981: Parameterization of vertical mixing in numerical models of tropical oceans. *Journal of Physical Oceanography*, **11**, 1443–1451.

Park, Y.-G., 1999: Stability of Thermohaline Circulation in a two-box model. *Journal of Physical Oceanography*, **14**, 3101–3110.

Polzin, K., 2004: Idealized solution for the energy balance of the finescale internal wave field. *Journal of Physical Oceanography*, **34**, 231–246.

Polzin, K. and E. Firing, 1997: Estimates of diapycnal mixing using LADCP and CTD data from I8S. *International WOCE Newsletter,*, **29**, 39–42.

Polzin, K., J. M. Toole, J. R. Ledwell, and Schmitt, 1997: Spatial variability of turbulent mixing in the abyssal ocean. *Science*, **276**, 93–96.

Rahmstorf, S. and A. Ganopolski, 1999: Long-term warming scenarios computed with an efficient coupled climate model. *Climatic Change*, **43**, 353–367.

Raper, S. C. B., J. M. Gregory, and R. J. Stouffer, 2002: The role of climate sensitivity and ocean heat uptake on AOGCM transient temperature response. *Journal of Climate*, **15**, 124–130.

Roeckner, E., et al., 2003: The Atmospheric General Circulation Model ECHAM5, Part I. Tech. rep., Max Planck Institute for Meteorology, Bundesstrasse 53, D - 20146, Hamburg.

Röske, F., 2006: A global heat and freshwater forcing dataset for ocean models. *Ocean Modelling*, **11**, 235–297.

Russell, J. L., 2006: The southern hemisphere westerlies in a warming world: propping open the door to the deep ocean. *Journal of Climate*, **19**.

Saenko, O. and W. Merryfield, 2004: On the effect of the topographically enhanced mixing on the Global Ocean Circulation. *Journal of Physical Oceanography*, **35**, 826–834.

Saenko, O. A., 2006: The effect of localized mixing on the ocean circulation and time-dependent climate change. *Journal of Physical Oceanography*, **36**, 140–160.

Sandström, J. W., 1908: Dynamische versuche mit Meerwasser. *Annalen der Hydrographie und Maritimen Meteorologie*, **36**, 6–23.

Schmitz, W. J., 1995: On the interbasin-scale thermohaline Circulation. *Reviews of Geophysics*, **33**, 151–173.

Scott, J. R. and J. Marotzke, 2002: The location of diapycnal mixing and the Meridional Overturning Circulation. *Journal of Physical Oceanography*, **32**, 3578–3595.

Semtner, A. J., 1976: Model for thermodynamic growth of sea-ice in numerical investigations of climate. *Journal of Physical Oceanography*, **6**, 379–389.

Simmons, H. L., S. R. Jayne, L. C. S. Laurent, and A. J. Weaver, 2004: Tidally driven mixing in a numerical model of the ocean general circulation. *Ocean Modelling*, **6**, 245–263.

Solomon, S., D. Qin, M. Manning, Z. Chen, M. Marquis, K. B. Averyt, M. Tignor, and H. L. Miller, 2007: *Contribution of Working Group I to the Fourth Assessment Report of the Intergovernmental Panel on Climate Change*. Cambridge University Press.

Talley, L. D., J. L. Reid, and P. E. Robbins, 2003: Data-based meridional overturning streamfunctions for the global ocean. *Journal of Climate*, **16**, 3213–3226.

Thorpe, R. B., J. M. Gregory, T. C. Johns, R. A. Wood, and J. F. B. Mitchell, 2001: Mechanisms determining the Atlantic Thermohaline Circulation resposne to greenhouse gas forcing in a non-flux adjusted coupled climate model. *Journal of Climate*, **14**, 3102–3116.

Toole, J. M., K. L. Polzin, and W. Schmitt, 1994: Estimates of diapycnal mixing in the Abyssal Ocean. *Science*, **264**, 1120–1123.

Tsujino, H., H. Hasumi, and N. Suginohara, 2000: Deep pacific circulation controlled by vertical diffusivity at the lower thermocline depths. *Journal of Physical Oceanography*, **30**.

Valcke, S., D. D. Caubel, and L. Terray, 2003: Oasis ocean atmosphere sea ice soil user's guide. Tech. rep., CERFACS.

Wiebe, E. C. and A. J. Weaver, 1999: On the sensitivity of global warming experiments to the parametrization of sub-grid scale ocean mixing. *Climate Dynamic*, **15**, 875–893.

Wunsch, C., 1998: The work done by the wind on the oceanic general circulation. *Journal of Physical Oceanography*, **28**, 2332–2340.

Wunsch, C. and R. Ferrari, 2004: Vertical mixing, energy, and the general circulation of the oceans. *Annual Review of fluid mechanics*, **36**, 281–314.

Zahel, W., J. Gavinho, and U. Seiler, 2000: Balances de energia y momento angular de un modelo global de mareas con asimilacion de datos. *GEOS*, **20**, 400–161.

Zhang, J., R. W. Schmitt, and R. X. Huang, 1999: The relative influence of diapycnal mxixing and hydrologic forcing on the stability of the thermohaline circulation. *Journal of Physical Oceanography*, **29**, 1096–1108.

Acknowledgements

I would like to thank my advisor Dr. Jin-Song Von Storch for her guidance, support and encouragement, without which I wouldn't have succeeded in completing my PhD. I would like to thank my co-advisor Dr. Johann Jungclaus, for his invaluable scientific opinion that came on some critical situations. Also, I wish to thank Dr. Prof. Detlef Quadfasel for chairing my panel, and helping me put an order to my time schedule. Thanks goes to Dr. Helmut Haak for giving me all the support I needed with setting up the model.

I also want to thank Dr. Ismael Nunez-Riboni, Dr. Daniela Matei and Dr. Katja Lohmann for reading my manuscripts. I want to thank specially Daniela for our interesting discussions during coffee breaks in the 2nd floor kitchen.

IMPRS would have been a completely different experience without Antje and Connie, their contribution to my phd life is inmeasurable.

Special thanks goes to all the people whom I shared office with during the last years in MPI: Nina, Chao, Laura, Alex, Antonija. My office life would have been incredibly boring without our chats. Also, special thanks goes to Laura for proof-reading my thesis and for providing pieces of advice.

Also, thank you to all IMPRS students for making it fun, especially: Fanny, Rosi, Werner, Peter, Steffen and many others who I forget.

My gratitude goes to my friends, Stergios, Olga, Thomas, Olga, Fani, Armelle, Nasia, Francesco, especially for tolerating my endless mood-swings during the last months before my submission.

Also, thanks goes to Swantje, Giovanni and Thomas, for the fun we had on our trips, but also for the fun we had here in Hamburg.

Finally, I want to dedicate my thesis to my family, knowing that it is hard for my parents to have their daughter 'in exile' for so long; and especially to Suvarchal, for being my compass, guiding me every single time I felt lost.

This work is partly funded by the DFG through the research project Sonderforschungsbereich 512.



ISSN 1614-1199